Etudes in situ par GISAXS de la croissance de nanoparticules

Gilles Renaud

Université de Grenoble

Diplôme d'Habilitation à Diriger des Recherches

Presenté par

Gilles RENAUD

Etudes *in situ* par GISAXS de la croissance de nanoparticules

soutenance le 21 mars 2011

Jury :

Rapporteurs :	Michèle Sauvage	- Synchotron SOLEIL
	Claude Henry	- CNRS-CINAM
	Pr. Vaclav Holý	- Université de Prague, République Tchèque
Examinateurs :	Pr. Thomas Michely	- Université de Köln, Allemagne
	Harald Reichert	- Synchrotron Européen, ESRF
	Roberto Felici	- Synchrotron Européen, ESRF

Grenoble's University

Habilitation to Supervise Research

Presented by

Gilles RENAUD

In situ GISAXS studies of growing nanoparticles

March 21st, 2011

Committee:

Referees :	Michèle Sauvage	- Synchotron SOLEIL
	Claude Henry	- CNRS-CINAM
	Pr. Vaclav Holý	- Prague's University, Czech Republic
Other members	Pr. Thomas Michely	- Köln's University, Germany
	Harald Reichert	- European Synchrotron Radiation Facility, ESRF
	Roberto Felici	- European Synchrotron Radiation Facility, ESRF

Contents

I. Foreword 1

II. Introduction to Grazing Incidence Small Angle X-Ray Scattering - GISAXS 2

III. An introduction to grazing incidence x-ray scattering 4
A. The basis of grazing incidence X-ray techniques on nanostructures 4
1. The scattering geometry 4
2. Reciprocal space of nanostructures on a surface 6
3. Advantages and drawbacks of X-ray techniques 7
4. *In situ* GISAXS and GIXS, in UHV, during growth 7
B. Experimental considerations 8
1. Background minimization 8
2. *In situ* GISAXS setups: Simultaneous analysis of morphology and structure by GISAXS and GIXS on the BM32 beamline 8
3. Detectors 10

IV. What is contained in GISAXS data: an introduction to the theory 11
A. Introduction 11
B. The scattering cross sections 11
1. Definition of the scattering cross section 11
2. The Born Approximation of first order (BA) 11
3. The Distorted Wave Born Approximation (DWBA) 11
4. The Fourier transform of particle shape 14
5. Scattering from faceted particles 14
6. Form factors of simple geometrical shapes 15
7. Miscellaneous remarks 16
8. Link between coherence length and coherent and incoherent scattering cross sections 16
C. Accounting for the particle-particle correlations : concentrated assembly of nanoparticles 18
1. Introduction 18
2. General formalism of the partial interference functions : coherent versus incoherent scattering 18
3. Decoupling Approximation 19
4. Local Monodisperse Approximation 20
5. The interference function 20
6. Two other approximations: Size-Spacing Correlation Approximation and Scaling Approximation 23
D. The graded interface model and the nanoparticle form factor 25
E. Deducing nanostructure size and shape from a rapid data analysis 26
1. The small polydispersity case 26
2. The large polydispersity case: nanostructure size distribution 26
3. The large polydispersity case: asymptotic behavior of the form factor 27
F. Summary on GISAXS data analysis 28

V. *In situ* GISAXS measurements in ultra-high vacuum, during growth 28
A. 3D-island growth: the metal/oxide interfaces case 28
1. Motivations 28
2. Investigated systems 29
3. Examples of extensive data analysis of GISAXS patterns from metal/oxide systems 30
4. General trends during growth and coalescence of islands 32
5. Evolution of morphological parameters with thickness: nucleation, growth and coalescence 35
6. Equilibrium shape, Wulff-Kaischew construction and adhesion energy 37
B. Surface nanofacetting: the case of Pt on W(111) 38
1. Nucleation and growth of 3-fold symmetry nanopyramids 39
2. Validity of the DWBA: GISAXS as function of the incident angle 40
3. The growth of Co on a faceted Pt/W{211} surface 41
C. Self-organized growth of nanostructures 41
1. The ordered growth of Co on Au(111) 42
2. The ordered growth of Co on a kinked vicinal surface of Au(111) 47

3. Self-organized growth of Co on a misfit dislocation network Ag/MgO(001)[1] 54
4. Self-organized growth of Ni clusters on a cobalt-oxide thin film induced by a buried misfit dislocation network 57

VI. Conclusion on *in situ* GISAXS 58

VII. Project of in situ x-ray studies of the growth of IV-IV semiconductors by physical and chemical beam epitaxy 59
A. Introduction 59
B. An introduction to nanowires, the vapor-liquid-solid growth and UHV chemical vapor deposition 60
1. Introduction 60
2. A few words on the interest of semiconductor nanowires 60
3. Types of NW: axial, radial and substrate/NW heterostructures 60
4. Methods to grow NWs: the Vapor-Liquid-Solid growth process 61
5. Controlling position, arrangement and size of catalytic metal islands for organized nanowire growth. 61
6. Ultra-High-Vacuum Chemical Vapor Deposition - UHV-CVD or Chemical Beam Epitaxy - CBE 62
C. *In situ* growth of semi-conductor nanostructures, from MBE and islands toward CBE and nanowires 63
1. Introduction 63
2. Methods: the complementarity between GIXS, SXRD, XRR and GISAXS 64
3. A glance on some recent *in situ* studies of SC performed using the BM32/SUV apparatus at the ESRF 64
4. A first step toward NW growth: the AuSi eutectic 69
D. Project of *in situ* X-ray studies of IV-IV semiconductor nanowire growth by Chemical Beam Epitaxy 71
E. Conclusions 72

References 73

I. FOREWORD

I started research using synchrotron radiation (at LURE-Orsay and SRS-Daresbury) during my PhD-Thesis, between 1985 and 1988, mostly using X-Ray Absorption Fine Structure (XAS-EXAFS) and Diffuse Scattering, to investigate the structural properties of alloys, in parallel with laboratory physical metallurgy studies[2]. I next spent one and a half year as a postdoc at Bell-Labs, where I learnt the bases of Grazing Incidence X-Rays Scattering/Diffraction (GIXS/GIXD), both at NSLS (Brokhaven)[3,4] and PEP (Stanford)[5]. I was employed at the CEA in 1990 to develop synchrotron radiations studies of surfaces and thin films. Between 1990 and 1992, I first built a beamline (in collaboration) and a surface diffractometer[6] at LURE, on the supraconducting wiggler, in which I performed first surface diffraction (SRXD) experiments. At that time, I choose to investigate the atomic structure of metal-oxide surfaces by SXRD[7,8], as well as the *in situ* growth of metal on oxide by GIXS and GIXD[9], performing also the first *in situ* Grazing Incidence Small Angle X-Ray Scattering (GISAXS) measurements with a punctual detector. Then I have been quickly involved in the development of the French Interface CRF/BM32 beamline at the ESRF, where I co-developed (with Robert Baudoing-Savois) a new surface diffractometer[10], associated with a large UHV chamber equipped with Molecular Beam Epitaxy (MBE). This instrument went in operation in 1996. I continued the study of oxide surfaces[11] and metal-oxide interfaces[12–15], there and on different ESRF beamlines, combining SXRD, GIXS, GIXD and 0D-GISAXS. This was a fast developing and very gratifying period, which was partly summarized in 1998 in a review paper[13]. In 1999, I developed a complete instrument on the ID32 ESRF beamline to perform GISAXS using a 2-dimensional detector, in UHV, *in situ* during growth, without any window before the sample, the UHV chamber being directly hooked to the sychrotron ring[16,17]. This yielded GISAXS measurements of exceptional quality which opened a new area of diverse studies, during which I progressively shifted from metal on oxide growth to the organized growth of metal dots on different patterned substrates[1,16,18–23]. Around 2001, I developed *in situ* GISAXS, combined with SXRD/GIXS/GIXD, on the MBE X-ray chamber of the BM32 beamline. Between 2000 and 2005, both instruments have been intensively exploited to investigate growing metal on oxides and (nanostructured) metal surfaces, together with first studies of germanium growth on nanostructured Si surfaces. I had the chance to collaborate with Remi Lazzari, a postdoc, Frederic Leroy, a PhD-student, and Christine Revenant, forming a team who developed the quantitative analysis of our GISAXS data, trying to go beyond simple analyses, and to understand in detail the diffuse scattering in GISAXS[16,18,19,21,24]. In parallel, thanks to the venue in our laboratory of specialists of anomalous scattering (Vincent Favre-Nicolin, Hubert Renevier, Johann Coraux), we developed the technique of Multiple Anomalous GISAXS (MAD-GISAXS)[22]. During all these years, we performed GISAXS measurements during growth, probing the morphology, in parallel with scattering measurements (SXRD, GIXS, GIXD), sometimes

anomalous, to probe the structure and composition of growing islands. Because covering all these results would be too wide a field , I have chosen in the first part of this manuscript to concentrate on the GISAXS part of our studies, corresponding to about 6 years of work, between 1999 and 2005. This work also led to the writing of an invited review[25]. Since then, my research has evolved toward *in situ* studies with all these x-ray techniques, of the growth of semiconductor islands (Ge on Si) and semiconductor surface structure[26], with a very recent extension of our MBE system to perform Chemical beam Epitaxy (CBE or UHV-CVD, Chemical Beam Epitaxy) in parallel with MBE. One of the objective of this combined MBE/CVD system is to allow for *in situ* structural investigations of growing semiconductor nanowires, which we already started by studying the fusion/solidification processes of AuSi eutectic catalysers[27]. This last work is the object of a very brief perspective chapter at the end of this manuscript. During all my research work, I have tried to develop and use synchrotron radiation scattering techniques to get the most accurate structural or morphological information during growth, with the goal of going beyond technical studies, to try to understand the basic mechanisms of the processes involved, such as the 3D growth of metal on oxide, or the intermixing between the Si substrate and the Ge deposit. I hope that this permanent concern is also revealed in this manuscript.

II. INTRODUCTION TO GRAZING INCIDENCE SMALL ANGLE X-RAY SCATTERING - GISAXS

Nanomaterials are widely seen as having a huge potential to bring benefits to many areas of research and application, and are attracting rapidly increasing investments in many parts of the world. Their properties differ significantly from those at a larger scale for two main reasons. First, quantum effects dominate the behavior of matter at the nanoscale affecting the structural, optical, electrical and magnetic properties of materials. Second, nanomaterials have a larger surface area when compared to the same mass of macroscopic material, which can make them much more chemically reactive, and affect their strength or electrical properties. Recent industrial developments are clearly targeted toward introducing nanostructures into everyday life[28]. For instance the ongoing trend of miniaturization in electronics is reaching the nanometer scale, where the performances such as tunneling, band structure or photon emission are determined by confinement effects (size, morphology, strain, atomic structure and composition). The past years have thus been marked by the elaboration and study of materials on nanometric scale, such as 2D layers or multilayers, and more recently 1D nanowires, or 0D nanoparticles, such as quantum dots, nanowires, nanotubes or buried aggregates. The properties of interest can be tuned by confining phenomena in objects where at least one dimension is smaller than a typical bulk length scale (screening length, exciton radius, magnetic domain size etc...). For instance, (i) reactivity and selectivity of catalysts made of supported metallic nanoparticles are driven by the nature of the exposed surfaces and by the particle electronic structure, which in turn depend on the particle size, shape and internal structure[29,30]; (ii) magnetic storage properties can be modulated and increased provided that controlled single domain magnetic nanoparticles can be elaborated[31,32]; (iii) in the field of semi-conductors, the novel transport or opto-electronics properties in coherently strained semiconductor nanoparticles, the so-called "quantum dots" (QDs)[33,34], are tuned by playing on the particle size, strain and composition[28].

These few examples are illustrative of the need for characterizing and controlling the growth and the structural properties of nanoobjects, *i.e.* their morphology, their structure and strain, and their composition. In addition, a better understanding of the growth mechanisms of nanoparticles is a prerequisite for their application on a large extent. This point is especially relevant in semiconductor devices. Their properties are highly dependent on the size, shape, strain, composition (interdiffusion), interface structure, roughness, defects and spatial organization on the substrate. Any change of these structural parameters over the assembly of particles gives rise to a broadening of the distribution of properties. It is therefore essential to characterise these quantities precisely as a function of the growth parameters such as substrate quality, temperature and deposition rate. This points to the importance of controlling the growth of a large collection of nanoparticles by monitoring *in situ* and in real time the relevant parameters. From a more fundamental point of view, the growth mechanisms themselves must be investigated, in order to deduce the kinetic coefficients and energy barriers involved in the growth process[35].

In this context, the morphological and structural properties of nanomaterials are usually addressed by a wealth of techniques such as laboratory X-ray diffraction (XRD), Transmission Electron Microscopy (TEM), High resolution Scanning Electron Microscopy (SEM), Scanning Tunneling Microscopy (STM) or Atomic Force Microscopy (AFM), and synchrotron radiation based X-ray techniques. All these techniques have advantages and drawbacks and are thus complementary to each others. If, for particles on top of a surface, Near Field Microscopy (NFM) techniques most often provide the required morphological information, they also have some limitations, such as limited statistics, convolution with the tip shape, difficulty to use on bulk insulating substrates and to use *in situ* during growth because of shadowing effects and temperature drift. Therefore long acquisition times and interruption of the growth

process are needed. For particles embedded in a matrix, below a surface, the NFM techniques are useless, and most other techniques are destructive.

Complementary information can be obtained in reciprocal space using X-ray scattering. For a long time, the small interaction of hard X-rays with matter hampered its straightforward use for surface or interface studies. However, since pioneering works in the 80th[36,37], the combined use of high brilliance synchrotron radiation and grazing incidence geometry allowed to reach surface sensitivity with a reasonable signal to noise ratio. Compared to microscopies, Grazing Incidence X-Ray Scattering or Diffraction (GIXS or GIXD)[13,38–41] and its small angle subset, Grazing Incidence Small-Angle X-Ray Scattering (GISAXS)[42] has several advantages :

(i) the technique is fully non destructive provided that the sample bears hard X-ray exposure;

(ii) the measurement is averaged over all the sample surface, giving statistical information over several square millimeters at variance to microscopies;

(iii) by varying the probed depth with the incident angle, X-rays offer the ability to probe from surface to buried interfaces as well as the bulk of the sample;

(iv) the technique can be applied in various types of environments from ultra-high vacuum to gas atmospheres, even during chemical reactions, *in situ* and in quasi real-time when kinetic phenomena are involved like during growth or a catalytic reaction; the measurements themselves usually require no special sample environment or preparation;

(v) the Grazing Incidence Small Angle Scattering (GISAXS) technique, which provides morphological information from the nanometer to micrometer length scales can be combined, on the same samples, with the grazing incidence wide angle X-ray scattering or diffraction (GIXS) technique which is sensitive to the atomic arrangement and strain state;

(vi) the chemical contrast of a given element can be enhanced by performing anomalous scattering close to a specific absorption edge, thus yielding compositional information.

As most techniques, X-ray scattering also has some drawbacks:

(i) the use of synchrotron radiation is nearly mandatory because the collected signal scales with the amount of material, which can be rather small (of the order of the monolayer).

(ii) the interesting information *e.g.* the morphology is obtained in reciprocal space, and thus has to be "translated" in the real world. As only scattered intensities can be measured, the phase information is lost, which means that some model assumptions are most often mandatory to fit the data. This problem can be overcome if the coherence of the synchrotron radiation is employed. The technique of coherent X-ray diffraction imaging is on the rise and allows for a model-free reconstruction of small crystals and nanostructures, mainly in diffraction configuration.

(iii) it is difficult to characterize a single nanoobject because of the beam size, divergence, and limitations of X-ray optics (although this field, called coherent X-ray diffraction, is going to develop). The statistical average over the coherent domains can be seen as an advantage since the beam samples the growing particles in the same way as for the macroscopic properties of interest, and gives an image of the "mean island".

Since the first experiments[42–44], the Grazing Incidence Small Angle X-Ray Scattering (GISAXS) technique has emerged in the last decade as a powerful tool to analyze the morphology and distribution of either islands on a substrate or buried particles, in parallel to the wide angle X-ray scattering techniques under grazing incidence, which provide unique average information on their atomic structure, strain and composition. The ability of GISAXS to characterize granular multilayered systems[45], implanted systems[46], as well as semiconductor quantum dots obtained by molecular beam epitaxy (MBE) or liquid phase epitaxy (LPE) is now well established[47–50]. Quite recently, new technical developments[16,17,25] allowed to apply this technique to topics which are relevant for surface science, by performing it *in situ* , during particle growth. By combining ultra-high vacuum environment and 2D-detection at small angles and by paying a special attention to the signal to noise ratio and measurement dynamics far away in reciprocal space, quantitative studies of various aspects of thin film growth, from sub-monolayer to percolation, or of surface nanostructuring became possible. High quality data and careful data analysis using the Distorted Wave Born Approximation with suitable programs[24,51] allow to get in one experiment statically averaged information relevant to the growth process which, otherwise, would have implied lengthly *ex situ* measurements. For instance, it has been demonstrated that the technique is relevant to cope with issues such as the particle equilibrium shape for

Pd/MgO(001)[13,16,18,29] or the self-organized growth of Co clusters on the herringbone reconstruction of the Au(111) surface[16,22,52,53]. Using the capability of X-rays to handle gas atmosphere, the technique starts now to be used to bridge the pressure gap for the study of catalytic nanoparticles at relevant pressure conditions[54,55]. In parallel to the measurements, the technique has benefited from theoretical developments to handle scattering at grazing incidence[56–58].

The objective of the present manuscript is to give a brief account of the the GISAXS technique, its theoretical background and analysis, and its application in situ, in UHV, during the growth of nanoparticles by physical evaporation, through a wealth of example of studies performed by the team of the author.

This manuscript is organized as follows. Sect. III is devoted to a basic presentation of the reciprocal space of nanostructures and its exploration with the Grazing Incidence X-Ray Scattering techniques at wide and small angles. Sect. III B presents a few experimental considerations, especially to perform GISAXS measurements *in situ*, in ultra-high vacuum (UHV), during the elaboration of nanostructures. Sect. IV introduces the basic features of the GISAXS interpretation for nanoparticles, with a simplified presentation of the different problems in the description and analysis of GISAXS data. Examples of extensive GISAXS pattern analysis given in Sect. V A 3 illustrate the concepts developed in the two previous sections. Sect. V focuses on *in situ* GISAXS experiments during growth from the group of the authors. Works on metal/oxide interfaces, Ge/Si system, self-organized growth on Au reconstructions or patterned surfaces by buried dislocation networks and nanofacetting of W surface are presented. Finally, the review ends up with an outlook of the present and future capabilities and developments of the technique.

III. AN INTRODUCTION TO GRAZING INCIDENCE X-RAY SCATTERING

A. The basis of grazing incidence X-ray techniques on nanostructures

1. *The scattering geometry*

X-ray scattering allows probing nanostructures by exploring the so-called reciprocal space, or the Fourier space. The principle of X-ray scattering from nanostructures is identical to traditional X-ray diffraction, except that, (i) synchrotron X-ray radiation is usually needed because the investigated volume of matter is small; and (ii) the incident X-ray wave vector $\mathbf{k}_i$ is kept at a grazing angle with respect to the sample surface to minimize the unwanted background scattering (both elastic and inelastic) emanating from the bulk, and to enhance the near-surface scattering. Figure 1

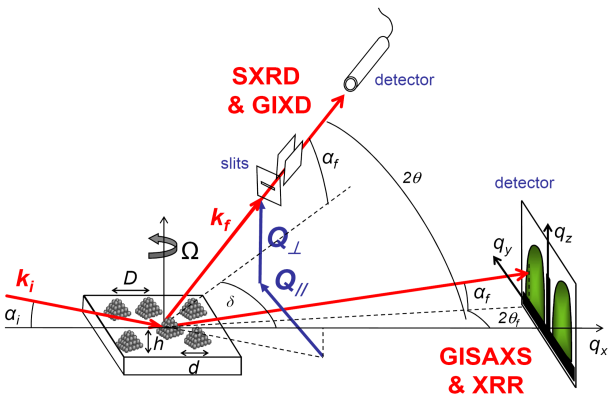

FIG. 1: Grazing incidence X-ray scattering geometry, at small (GISAXS and XRR), and large angles (GIWAXS or GIXD or GID and SXRD). For GISAXS, a 2D detector is used, with a beam stop hiding the direct and specular beam, as well as the specular rod. The intensity is recorded as a function of the two angles, $2\theta_f$ and α_f, describing the in-plane and out-of plane angles between the incident and scattered wavectors, respectively. These angles are related to the wavevector transfer coordinates, q_x, q_y and q_z according to Eq. 3.1. The sample can be rotated by an angle ω around its surface normal. SXRD and GIXD correspond to large values of the scattering angle 2θ between $\mathbf{k_i}$ and $\mathbf{k_f}$, and hence large values of the in-plane, δ, and out-off-plane, α_f, scattering angles. The direction of the exit wavevector $\mathbf{k_f}$ is defined by slits parallel and perpendicular to the surface, behind which lies the detector, which can be punctual or linear, or even two-dimensional.

shows a schematic drawing of such measurements in grazing incident scattering geometry, for which the incident angle α_i is generally small and kept constant, most of the time close to the crtitical angle for total external reflection α_c.

The scattered beam, of wave vector $\mathbf{k}_f$, makes the scattering angle 2θ with respect to the incident wave vector. The wavevector transfer is defined as $\mathbf{q} = \mathbf{k}_f - \mathbf{k}_i$, and is often decomposed into two components, $\mathbf{q}_{\parallel} = (q_x, q_y)$ and $q_\perp = q_z$, respectively parallel and perpendicular to the surface. The absolute value of $\mathbf{q}_\perp$ is a function of α_i and α_f: $|\mathbf{q}_\perp| = q_z = k_0[\sin(\alpha_f)+\sin(\alpha_i)]$, where $k_0 = |k_f| = |k_i| = 2\pi/\lambda$ is the elastically conserved wave vector modulus. λ is the X-ray wavelength. In GISAXS as well as in GIXS, the angular coordinates are related to the wavevector transfer coordinates according to:

$$\begin{aligned} q_x &= k_0[\cos(2\theta_f)\cos(\alpha_f) - \cos(\alpha_i)] \\ q_y &= k_0[\sin(2\theta_f)\cos(\alpha_f)] \\ q_z &= k_0[\sin(\alpha_f) + \sin(\alpha_i)] \\ k_0 &= 2\pi/\lambda. \end{aligned} \tag{3.1}$$

GISAXS and X-Ray Reflecticity (XRR)[40,41,59] are special cases of GIXS, for which all angles considered are small, *i.e.* less than a few degrees (Fig. 1). The wavevector transfer is also small, typically between 0 and 1 nm^{-1}, and hence large dimensions are probed in real space. XRR is used in the specular geometry to probe the density profile perpendicular to the surface and in the off-specular geometry to probe large lateral electron density correlations (along q_x). GISAXS is used to probe the morphology parallel to the surface (along q_y) and perpendicular to it (along q_z), at intermediate length scales (typically between a few nm and a few hundreds of nm). At these small angles, the curvature of the Ewald's sphere can be, most of the time, neglected ($q_x \simeq 0$) and the reciprocal space scales with the angular coordinates $q_y \simeq k_0 \sin(2\theta_f) \simeq k_0 2\theta_f$ and $q_z \simeq k_0\alpha_f$, respectively parallel and perpendicular to the surface. The intensity is measured very close to the origin of the reciprocal space, and hence $q_{y,z}$ span a small range, of a few nm^{-1}. If nanometer-size in-homogeneities of the electron density such as islands, roughness or electronic contrast variation are present on the surface, they scatter the incident, reflected and transmitted beams in a way that depends on their morphology and topography. The sample can be rotated around its surface normal by an angle ω, defining the orientation of the incident X-ray beam with respect to the in-plane crystallographic directions, which is necessary to investigate anisotropic islands. A T-shape beam-stop absorbs the direct and reflected beam before they hit the detector. Note that the origin of the out-of plane exit angle α_f is exactly between the direct and specularly reflected beams. Because these two beams are often hidden by a beamstop, determining the origin may not be trivial. Because of refraction and reflection effects[56,57] the maximum of the off-specular diffuse scattering intensity, also called Yoneda peak, is located at α_c. In order to properly define the origin of reciprocal space, it might be wise to record an image of the direct and specularly reflected beams, without beamstop but for a strongly attenuated incident beam as several orders of magnitude in intensity separate the diffuse scattering from the transmitted and reflected beams.

In the last 20 years, GISAXS has emerged as a powerful tool to analyze the morphology and distribution of either islands on a substrate or buried nanoparticles. The first GISAXS experiments were performed in 1989 with a rotating anode by J. Levine *et al.* on Au deposits on glass[42,43,60]. Naudon *et al.* developed also GISAXS at LURE (Laboratoire pour l'Utilisation du Rayonnement Electromagnétique, France) in order to study clustering near surfaces[44,61–65]. The first *in situ* experiments concerned the growth of metallic islands[66]. GISAXS allowed also studying the surface roughness[67,68], the lateral correlations, sizes and shapes of semiconductor dots[48,69–72], discontinuous multilayers[45], self-organized dot superlattices[71,73] or wires[74]. Recent developments consisted in GISAXS measurements performed in UHV, *in situ*, during MBE, and with no scattering element between the undulator synchrotron X-ray source and the detector, thus yielding a very high sensitivity and background-free data[16].

Wide angle scattering allows probing the order at the atomic scale, with two corresponding techniques: Grazing Incidence (Wide Angle) X-Ray Scattering (GIXS or GIWAXS), also often referred to GIXD or GIXRD or GID for Grazing Incidence X-ray Diffraction, which is the typical technique to probe the crystallographic lattice of nanostructures, and Surface X-Ray Diffraction (SXRD), which is basically the same, but applied to atomic structure determination (*i.e.* atomic positions) at surfaces and interfaces. When α_i and α_f are very small, $q \simeq q_{\parallel}$, the scattering plane is nearly parallel to the surface, and diffracting lattice planes are perpendicular to it. The scattering geometry being defined by the incident beam and detector directions, one has only to rotate the sample around its surface normal to bring these lattice planes into diffraction condition. In that way, the long-range periodicity parallel to the surface is probed. It is often useful to measure the scattered intensity as a function of $q_\perp$, which is achieved by increasing α_f while keeping grazing incidence.

Because the incident angle is small, it is necessary to consider the effects of refraction at the surface[56,57,75]. The refractive index, n, of matter for X-rays being slightly less than unity ($n = 1 - \delta - i\beta$ with $\delta, \beta > 0$), the transmitted beam bends toward the surface as a result of refraction. δ and β are related to the atomic scattering form factor (*i.e.* the Fourier transform of the electronic cloud) $f(\mathbf{q}) = f^0(\mathbf{q}) + f' + if''$ ($\mathbf{q}$ is the scattering wave vector) and to the

atomic density ρ_a[59]:

$$\delta = \frac{r_e \rho_a (f^0(0) + f')\lambda^2}{2\pi}; \quad \beta = \frac{r_e \rho_a f''\lambda^2}{2\pi}. \tag{3.2}$$

The anomalous dispersion correction $f' + if''$ applied on $f^0(\mathbf{q})$ is due to absorption edges and depends on the photon energy E; $f^0(0)$ (=Z) is the number of electrons per atom. When α_i is smaller than a critical value α_c, the beam is totally reflected, and only an evanescent wave, which decays over tens of angstroms, is present below the surface. When α_i is larger than α_c, the transmitted wave propagates into the bulk. Identical refractive effects occur as a function of the exit angle α_f. A full data set of refraction indexes δ, β, dispersion corrections f', f'' and absorption coefficients can be found on the web[76]. The amplitude Fresnel reflection (r) and transmission (t) coefficient are then easily obtained. Three different regimes can be distinguished as function of $\alpha_{i,f}$:(i) when $\alpha_{i,f} \ll \alpha_c$, $r \simeq -1$, the reflected wave is in phase opposition with the incident one. Since the transmission angle α_t is almost imaginary, the transmitted wave is evanescent and propagates only parallel to the surface on a penetration depth given by $\Lambda_c = 1/2k_0\alpha_c$. This is the phenomenon of total external reflection of X-rays. (ii) When $\alpha_i = \alpha_c$, $r \simeq 1$, the incident and the reflected waves are nearly in phase while the amplitude of the transmitted wave is close to twice that of the incident wave, $t \simeq 2$. A steep decrease of reflected intensity is observed at $\alpha_i \geq \alpha_c$. (iii) For $\alpha_i \gg \alpha_c$: the asymptotic behaviors of the Fresnel coefficients are $r \simeq \alpha_c^2/4\alpha_i^2$, $t \simeq 1$. There is almost complete transmission with a penetration only limited by the absorption β in the material. The reflected wave is in phase with the incident one.

2. *Reciprocal space of nanostructures on a surface*

In general, either α_i or α_f are fixed, and the three remaining angular coordinates (δ, $\alpha_{i,f}$ and *omega*) are varied to explore the intensity scattered in reciprocal space. A schematic representation of a typical reciprocal space map (that of germanium nanostructures on top of a Si(001) surface) is shown in Fig. 2. The expressions of the intensity scattered by three-dimensional crystals, 2D crystals, surfaces of bulk crystals, and nanostructures deposited on a substrate can be found in standard text-books[40,41,59,77–79] or review articles[13,38,39,80–83]. The most important feature is that, since the interaction of hard X-rays with matter is weak, the kinematical approximation of single scattering, the so-called Born approximation (BA), or its application for grazing incidence geometry, the Distorted Wave Born Approximation (DWBA), are valid in most cases, except for perfect crystals near Bragg scattering[78]. Fig. 2

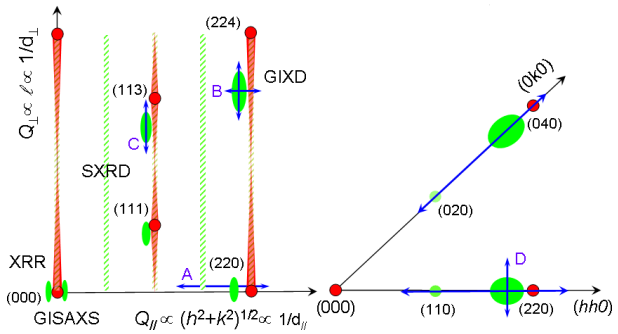

FIG. 2: (left side) Schematic representation of the reciprocal space of a three-dimensional crystal of the diamond (Si,Ge) structure, truncated by a (001) surface, giving rise to the crystal truncation rods (CTRs in red) with maximum intensity at the bulk Bragg positions (red disks) and quickly varying in between. In green the contribution from a strained two-dimensional, two-fold reconstructed epilayer is shown, yielding flat scattering rods (green shaded vertical rods) at the same position as bulk CTRs, since it is assumed that its lattice parameter parallel to the surface is fully strained to the one of the substrate. The scattering rod in half position is due to the (2×1) surface reconstruction. In case of three-dimensional islands, diffraction peaks that are closer to the origin with respect to the substrate peaks are expected, as the overlayer is supposed to have a larger lattice parameter (note that the spacing between substrate and overlayer Bragg peaks has been enlarged for the purpose of representation). This reciprocal space pattern is typical for the Stranski-Krastanow growth of Ge islands on Si(001) for instance. Typical scans are represented by blue arrows. (right side) Corresponding intensity distribution in the (001) surface plane

qualitatively shows the intensity scattered by nanostructures (or an epilayer) on top of a substrate, as a function of the in-plane and out-of-plane wavevector transfers. The semi-infinite crystal yields CTRs[38,39], and the nanostructures

yield wide Bragg reflections. They may be peaked at different $\mathbf{q}_\perp$ (or $\mathbf{q}_\parallel$) values if the out-of (in-) plane lattice vector differs from one to the other. This allows independent analysis of the out-of-plane and in-plane structural properties of the nanostructures, such as strain, composition and shape, without interference with the substrate. The strain relaxation in the nanostructures parallel and perpendicular to the surface can be analyzed separately by performing respectively $\mathbf{q}_\parallel$ scans (such as scan A of Fig. 2) around in-plane Bragg peaks and $\mathbf{q}_\perp$ scans (such as scans B or C of Fig. 2) around out-of-plane Bragg peaks. If the nanostructures are constrained to the substrate lattice parameter parallel to the interfacial plane, the corresponding peaks appear at the same $\mathbf{q}_\parallel$ position as the substrate CTRs and interferences occur between the waves scattered by the substrate and the nanostructures. Analysis of these interferences can provide information on the interface structure between the substrate and the nanostructures.

3. Advantages and drawbacks of X-ray techniques

The most widely used techniques to study the fluctuations of electron density on or below surfaces are imaging techniques such as Transmission Electron Microscopy (TEM), Scanning Electron Microscopy (SEM), and near field microscopies like Scanning Tunneling Microscopy (STM) and Atomic Force Microscopy (AFM). However, if these techniques may provide some of the required information, real space observations often suffer from slowness, sampling limits, and artifacts, such as those due to the inevitable convolution with the tip in the cases of STM and AFM, or the modifications induced by the necessary sample preparation (TEM, SEM). In addition, they are either difficult (AFM, STM, SEM) or impossible (TEM) to use *in situ*, *e.g.* in UHV during the growth of nanoparticles or on insulating substrates like oxides. These limitations can be overcome by techniques based on X-ray scattering. X-rays are adapted to any kind of materials without suffering from charging effects; they provide depth sensitivity, thus allowing to probe buried interfaces; they provide a statistical averaging over the whole sample area, thus sampling the same way as macroscopic characterization techniques; they can be used at any pressure or temperature, and in any king of sample environment in particular in UHV, during growth and sometimes in real time. Chemical sensitivity can be achieved by tuning the X-ray wavelength across an absorption edge to vary the atomic structure factor of a chosen element. The main drawbacks of X-rays are the nearly unavoidable use of synchrotron radiation to get reasonable counting time on nanostructures and data analysis that relies on modeling of reciprocal space measurements.

4. In situ GISAXS and GIXS, in UHV, during growth

In general, the structure and morphology of nanostructures (or an epilayer) on a substrate depend on many parameters, such as the initial structure of the substrate surface itself, the structure of the deposited material, the surface and interface energies, the lattice parameter misfit and the growth kinetics. The above GIXS technique (GIXS being taken as a generic name for GIXS, GIXD, GISAXS, XRR specular and off-specular, SXRD ...) is one of the very scarce tools that can be used *in situ*, for instance in UHV, to follow the evolution of the structure and morphology during growth, from sub-monolayer deposits to fairly thick films (up to μm in thickness). In principle, the factors influencing the overlayer growth, such as the defect density of the substrate, the temperature during growth and the incoming fluxes can be systematically varied. The structure of the substrate, either reconstructed or not, should be investigated first. Its average roughness can be deduced from analysis of the CTRs integrated intensities, and the surface domain size and average terrace width deduced from CTRs line-shape analysis. Systematic measurements during growth may then provide the evolution of the structure and morphology with the overlayer thickness; such as the interfacial distance between both materials in heteroepitaxy; the average in-plane and out-of-plane lattice parameters and strain distributions, the mosaic spread and the domain size parallel and perpendicular to the interface. In the case of a three-dimensional growth, the domain size is directly related to the size of the nanostructures. The shape and size of these growing nanostructures can be measured *in situ* by grazing incidence small angle X-ray scattering (GISAXS) experiments. GIXS can also be used to analyze different growth defects such as stacking faults, twins and dislocation nucleation. Indeed, stacking faults are planar defects, and thus yield rods of scattering perpendicular to the plane of the fault. Twinned crystals yield Bragg peaks that are related by mirror symmetry to those of the untwinned stacking. Finally, the nucleation of dislocations in the growing film leads to inhomogeneous deformations that may be detected through radial $\mathbf{q}$ scans. These kinds of studies require the sample to be in Ultra High Vacuum (UHV), so that the necessary vacuum hardware has to be combined with an X-ray diffractometer. The main difficulty is to associate the necessary precise movements of the sample with a UHV environment. Several diffractometers devoted to performing *in-situ* GIXS have recently been built with these requirements in many synchrotron facilities around the world.

B. Experimental considerations

1. Background minimization

The most interesting specificity of GISAXS is to probe the nanostructure morphology, *i.e.*, shape and size. As will be discussed later, these can be derived in principle from the form factor, *i.e.* the Fourier transform of the nanoparticle shape. However, the scattered intensity is (at least parallel to the surface) the product of the form factor by an interference function. In the case of concentrated systems, these two terms are strongly correlated at small q_y values[18]. Nevertheless, in disordered systems, the interference function tends to one as the wavevector transfer increases, and the GISAXS intensity is then entirely determined by the form factor. Hence, in order to discriminate between different shapes and accurately determine the nanostructure size and size distribution, the intensity must be measured (i) far from the origin of the reciprocal space and (ii) over several orders of magnitude. This requires a background as low as possible as the form factor decreases rapidly with increasing q_y values.
Because the signal is very close to the direct beam, a major constraint in GISAXS (like for any small angle X-ray scattering measurement) is to decrease as much as possible the background arising from the sample itself, from the beam divergence, from all the optical elements of the beamline, from beryllium windows placed in the beam path, and of course from air. This requires a bright beam with a very low divergence, high quality optical elements and several pairs of slits to define the beam and remove unwanted low-angle scattering. More importantly, when performing surface X-ray scattering in ultra-high vacuum (UHV) to study the growth by *e.g.* molecular beam epitaxy (MBE), a beryllium window is usually present to enter into and exit the UHV chamber. A Be window is also present at the end of the beamline and the X-ray beam passes through a small path of air between the beamline and the chamber. These Be windows and air-path generate large background scattering at small angles, which in addition varies very quickly with small, micrometric variations (which are inevitable on a synchrotron beamline) of the beam impact on the Be window. We have developed two different experimental setups to minimize these sources of background. We call them ID32 and BM32 from the names of the ESRF (European Synchrotron Radiation Facility, Grenoble-France) beamline on which they were developed.

2. In situ GISAXS setups: Simultaneous analysis of morphology and structure by GISAXS and GIXS on the BM32 beamline

A first setup, described at depth in Ref.[17],had been developed on the ID32 ESRF beamline to perfomed GISAXS *in situ*, in UHV during growth. The main characteristics are that the UHV chamber was directly hooked to the beamline, and no beryllium window was present between the sample and the X-ray source[17]. The only Be window was at the end of the beam path, just before the 2D detector; it did not provide any additional background as the unwanted diffuse signal was hidden by the beam stop before it diverges. Because it is no longer in use, we concentrate on the description of the BM32 setup.
This second experimental setup has been developed to allow simultaneously performing GISAXS, GIXS and X-ray Reflectivity measurements on the same sample, *in situ*, in UHV, at different growth stages. The sample position is kept fixed for all X-ray measurements, physical vapor deposition, as well as for sample preparation (ion bombardment and heating) and for characterization by Auger Electron Spectroscopy (AES) or Reflection High Energy Electron Diffraction (RHEED). For that sake, the setup is made of a sophisticated UHV chamber coupled to a large diffractometer. Fig. 3 shows a schematic drawing and Fig. 4 a photograph of the UHV chamber dedicated to X-ray diffraction, while Fig. 5 shows a schematic drawing of the setup to perform GISAXS. The instrument is located at the end of an ESRF bending magnet beamline: BM32 [84]. The white X-ray beam is first vertically collimated by a mirror coated with iridium; it is then monochromatized by a double crystal Si(111) monochromator, the second crystal focusing the beam in the horizontal direction; the beam is finally vertically focused at the sample location by a second mirror. The resulting beam size at the sample location is $\simeq 0.25$ mm (H) $\times$ $\simeq 0.15$ mm (V) (Full Width at Half Maximum (FWHM)), with a divergence of $\simeq 0.5$ mrad (H) $\times$ $\simeq 0.13$ mrad (V) (FWHM). It is further defined in the experimental hutch by two sets of vertical and horizontal entrance slits separated by 2 m (see Fig. 5). The first set defines the vertical beam size of typically 0.1 to 0.3 mm (V); the second set removes the unwanted scattering by the first slits. The incident beam then passes a filter box, and then a monitor based on two diodes measuring the scattering by a Kapton foil placed in the beam. It next enters the X-ray UHV chamber.
Because of many constrains, the UHV chamber could no longer be directly connected to the beamline: it had to be equipped with an entrance and an exit beryllium windows. These, together with the beamline slits and windows, generate background at small angles. This background is eliminated by a series of slits and beam-stop, in-vacuum and outside vacuum (Fig. 5), The first is a vertical slit placed inside the chamber, in UHV, just after the entrance Be window, which lets only the incident beam hitting the sample, and eliminates all the remaining unwanted X-rays, especially those scattered by the entrance Be window. Actually, a set of 3 tantalum slits with different fixed openings

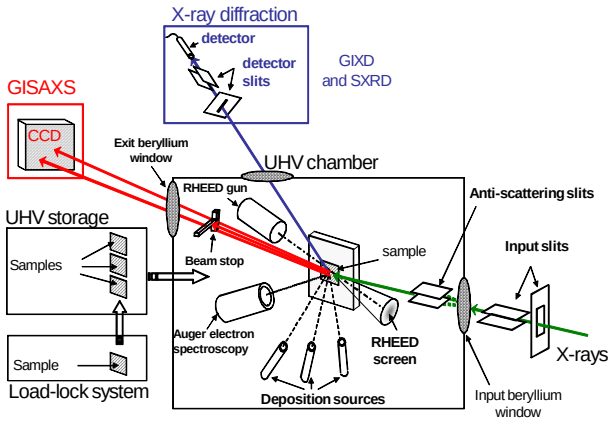

FIG. 3: Principle of the SUV/BM32 UHV chamber coupled to a diffractometer for GISAXS, GIXS and XRR measurements on the same sample, during growth. The doubly focused and monochromatic X-ray beam delivered by the beamline enters into the hutch from the right. Its size and divergence are further defined by slits working in vacuum. The beam hits the exit Be window of the beamline, then the entrance X-ray window of the UHV chamber. It it next scattered by the sample before exiting the UHV chamber, hitting again a Be window. The scattered beam can then be measured for GIXS or XRR measurements by a 0D (or 1D) detector placed after a pair of vertical and horizontal slits defining the direction of $\mathbf{k_f}$, or at small angle by a 2D detector for GISAXS. In GISAXS, background is nearly suppressed thanks to input guard slits and a knife edge placed in UHV just after the entrance Be window, suppressing all the unwanted X-rays before the sample, and thanks to a beam-stop placed after the sample, just before the exit Be window, blocking the incident beam, and thus avoiding any scattering by the exit Be window. In addition, the UHV chamber is equipped with a RHEED set-up and an Auger spectrometer, and can be equipped with up to 6 depositions cells, all apparatus looking directly at the sample when in position for X-ray measurements. Sample introduction is performed through a load-lock and a storage/introduction UHV chamber.

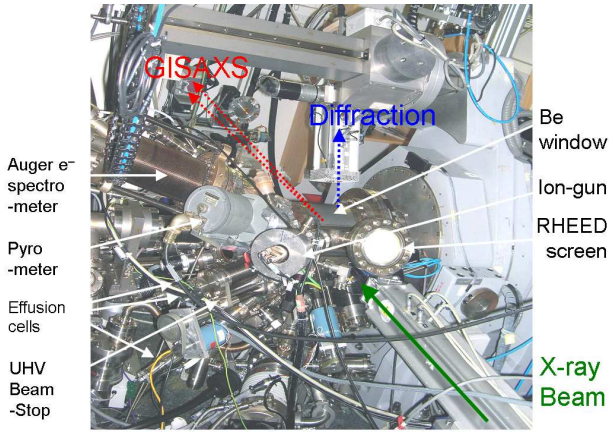

FIG. 4: Photograph of the core of the SUV/BM32 UHV diffractometer. The beam enters into the UHV chamber from the bottom right corner. The GISAXS 2D camera is at the top left corner; the slit/detector system for GIXD measurements is toward the top. UHV instrumentation and introduction are all around the UHV chamber. Parts are visible on the left and bottom sides of the photograph. On the right is the heavy-duty diffractometer holding the UHV chamber with all its pumps and instrumentation. A small part of the UHV chamber is visible at the center of the photograph, with the entrance and exit Be windows visible in gray. The sample, with a vertical surface, is held by a furnace allowing to reach 2500 K.

(0.25, 0.3 and 0.35 mm) can be used on purpose. The horizontal size of the beam being much larger than the projected sample size, because of the very small incident angle, it is also mandatory to eliminate most of the beam which is not used in this direction. This is done by the molybdenum sample holder on the back side of the sample, and by a tungsten knife-edge mounted on a translation on the front side. This knife edge is located in UHV between the entrance Be window and the sample. The last UHV tool is a T-shape beamstop made of tungsten which is placed inside the chamber, just before the exit window. Its role is to stop the incident and specularly reflected beams, while letting the small-angle scattering exit the chamber, thus avoiding unwanted scattering by the exit Be window. In

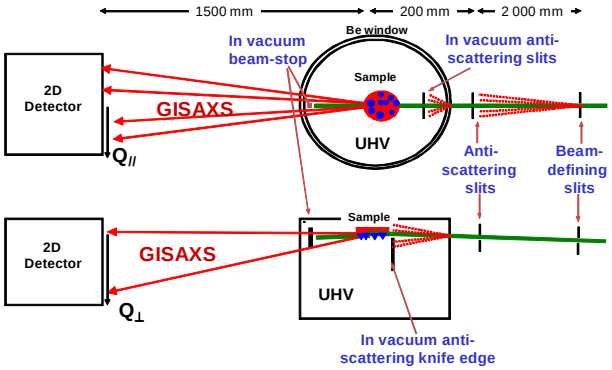

FIG. 5: Principle of the anti-scattering system for GISAXS measurements on the SUV/BM32 setup. The incident beam is schematizes by a green line arising from the right. Slits and anti-scattering slits, knife edge and beam-stop are schematised in blue. The small angle X-ray scattering is schematizes by red arrows.

principle, these three tools placed in UHV efficiently suppress the background scattering. If this is not the case, two additional T-shape tungsten beam-stops placed in air can be added: one just after the exit Be window, and one just before the 2D detector.

The 2D detector can be placed between 0.3 and 3 m downstream the sample, thus allowing to vary the measured fraction of reciprocal space over a wide range. A He-filled flight tube is usually inserted between the chamber and the detector to avoid absorption and scattering by air.

The UHV chamber can be equipped by as many as eight deposition sources; typically four effusion cells and four electron-bombardment cells. A large number of metals have been evaporated in this chamber, as well as semiconductors (Si and Ge). The chamber is equipped with a double-pass cylindrical mirror analyzer for AES measurements, and with a 35 keV RHEED apparatus. A quadrupolar residual gas analyzer is also available. The base vacuum is between 2×10^{-11} and 1×10^{-10} mbar according to preparation conditions.

The diffractometer, of "z-axis"[85] type, has been described elsewhere[10]. The reciprocal space can be explored at wide angles thanks to two detector rotations δ and $\beta(\equiv \alpha_f)$, in addition to the two sample ones ω and $\alpha(\equiv \alpha_i)$. The detector acceptance can be fitted with different sets of slits (typical angular acceptance 3.5 mrads). For GIXD, the footprint is a lozenge of variable angle given by the in-plane scattering angle δ, and the lengths of the sides are 0.3 mm and the width of the vertical detection slits. For GISAXS, the beam footprint is a long, 0.3 mm wide stripe, of length equal to the sample diameter. As a result, the instrument can be used not only for GISAXS measurements, but also for XRR and GIXS ones, on the same sample, with no realignment.

3. Detectors

The small angle scattering is typically collected on a high grade and high dynamic range Charge Coupled Devices (CCD) detectors. The 16-bit CCD from Princeton Instruments for most of the studies presented later has 1152×1242 pixels of 56.25×56.25 μm^2 size, with a rectangular acceptance of 65×70 mm^2 and a threefold demagnification insured by a tapered assembly of optical fibers. The phosphor screen of Gd_2O_2S is optimized for energies between 3 and 30 keV. The full well capacity is 3×10^5 electrons, with a readout noise of 7 electrons (for 100 kHz reading). The CCD is cooled down to -60°C by a four stage Peltier system, resulting in a very small dark current (< 0.02 electron/pixel/s). The detector is under vacuum, and the X-rays enter through a 90 mm diameter 0.02 mm-thick Be window. It is mounted on three translations (vertical and horizontal, along the beam and perpendicular to it, respectively), at a variable distance between 0.3 and 3 m from the sample. Depending on this distance, the maximum 2θ angle typically ranges from 0.2° to 5°, and the maximum exit angle from 0.2° to 10°.

After acquisition, the data are corrected from the flat field, the dark counts, the CCD distortions. In addition, when needed, the reference signal from the bare substrate prior to deposition is subtracted.

IV. WHAT IS CONTAINED IN GISAXS DATA: AN INTRODUCTION TO THE THEORY

A. Introduction

In the context of morphological characterization of nanoobjects, the GISAXS technique offers the opportunity to probe as a whole an assembly of nanoparticles and to define an "average particle". Not only the sizes and the particle density can be deduce from a proper analysis of the GISAXS scattering profile, but also others quantities like the particle shape, the width of the size distribution or higher order correlation parameters. The present section is aimed at introducing briefly the basic notion that are necessary to understand, and deduce, was is contained in 2D GISAXS data, such as the average inter-nanostructures distance, nanostructures shape, size, and size distribution. The rigorous theoretical foundations, which may be found in a recent review[25] are not detailed here.

B. The scattering cross sections

1. *Definition of the scattering cross section*

During an experiment, the measured quantity as function of the scattering angles is the differential scattering cross section, defined as the radiated power $d\sigma$ along a given direction $\mathbf{r}$ far away from the sample in a given solid angle $d\Omega$ per incident energy E_0^2.

2. *The Born Approximation of first order (BA)*

In the first order Born approximation (single or kinematic scattering), the total differential scattering cross section reads:

$$\frac{d\sigma}{d\Omega} = \frac{k_0^4}{16\pi^2}(\mathbf{e}_f^{s,p}.\mathbf{e}_i^{s,p})^2 \left| \int d\mathbf{r}' \delta n^2(\mathbf{r}') e^{i\mathbf{q}.\mathbf{r}'} \right|^2 . \tag{4.1}$$

where $\mathbf{e}_i^{s,p}$ and $\mathbf{e}_f^{s,p}$ are the polarization vector of the incident and scattered waves and $\mathbf{q} = \mathbf{k}_f - \mathbf{k}_i$ is the wave vector transfer. The dielectric constant $\epsilon(\mathbf{r}) = n^2(\mathbf{r})$ of the medium has been split in two parts:

$$n^2(\mathbf{r}) = n_0^2(\mathbf{r}) + \delta n^2(\mathbf{r}), \tag{4.2}$$

where $n_0(\mathbf{r})$ is the index of refraction of a reference medium. Hence, as obtained in standard textbooks on scattering[77,78], the Born approximation cross section is simply proportional to the square modulus of the Fourier transform of the dielectric index.

3. *The Distorted Wave Born Approximation (DWBA)*

When the incident angle α_i is close to α_c, the surface acts as a mirror and multiple scattering effects come into play, leading to the inadequacy of the Born Approximation (BA). Instead, DWBA is more suitable. The DWBA is an extension of the single scattering formalism including the contribution of different single scattering processes arising from perturbations of the incident, reflected and refracted wavefields by the nanostructures[56–58] on the reflection-refraction of waves at interfaces. The interested reader can refer to the many standard text books[40,41,59] or reviews[13,39,80,81,86–88] that deal with the theoretical and experimental aspects of scattering from surfaces. Let us consider two simple cases: that of density fluctuations buried below a surface, and that of nanoparticles deposited on a surface.

a. Buried density fluctuations Scattering from density fluctuations buried under a rough surface was evoked by Sinha[89] and fully treated by Rauscher *et al.*[57] under the assumption of the absence of cross correlation with the surface roughness. In that case, the scattering from the rough surface and from the density fluctuations add up incoherently, except along the specular rod. Special cases of δ-like layer at the surface, columnar structures, isotropic density fluctuations and layered structures were chosen as basic examples. Multilayers of density inhomogeneities and density fluctuations at a liquid surface were treated in Ref.[40].

For buried density fluctuations $\delta n^2(\mathbf{r})$ under a flat surface of a substrate of index n, the scattering cross section for $q_\parallel \neq 0$ can be written in the form:

$$\left(\frac{d\sigma}{d\Omega}\right)_{incoh} = \frac{k_0^4 A_i}{16\pi^2} \left|t^i\right|^2 \left|t^f\right|^2 \mathcal{C}(q_\parallel, q_z) \tag{4.3}$$

$$\begin{aligned}\mathcal{C}(q_\parallel, q_z) = \int d\mathbf{R}_\parallel e^{i\mathbf{q}_\parallel.\mathbf{R}_\parallel} \int_{-\infty}^{0} dz \int_{-\infty}^{0} dz' e^{iq_{z,1}z} e^{-iq_{z,1}^* z} \\ \left\langle \delta n^2(0,z) \delta n^{2*}(\mathbf{R}_\parallel, z') \right\rangle ,\end{aligned} \tag{4.4}$$

where $q_{z,1} = k_{f\,z,1} - k_{i\,z,1}$ is the wavevector transfer inside the substrate. The intensity is a kind of Fourier transform of the autocorrelation function of the dielectric contrast $\left\langle \delta n^2(0,z) \delta n^{2*}(\mathbf{R}_\parallel, z') \right\rangle$; however, at variance to the Born approximation, apart the transmission function prefactors, it is the wavevector transfer of the transmitted waves that comes into play in the formula. Only density fluctuations inside the scattering depth $1/\mathrm{Im}(q_{z,1})$ (which takes into account both incident and exit evanescent waves) contribute to the cross section. For scattering angles α_i, α_f above the critical angle of the substrate, only a slight shift of the scattering pattern as compared to BA is observed as $q_{z,1} \simeq q_z$ and $t^i, t^f \simeq 1$. On the contrary, below the critical angle, the scattering involves an evanescent wave; either $k_{f\,z,1}$ or $k_{i\,z,1}$ become imaginary leading to an enhanced surface sensitivity of the measurement as compared to classical transmission geometry.

b. The supported nanoparticle - dilute case The calculation of the scattering cross section under the DWBA was later obtained for free standing nanostructures[58,71], for pores in mesoporous thin films[90–93] and for holes in a substrate[94]. Let us consider a particle of shape $S(\mathbf{r})$ ($S(\mathbf{r}) = 1$ inside it; $S(\mathbf{r}) = 0$ outside) and index of refraction n_p, embedded in a medium of index n. The dielectric constant is decomposed according to:

$$n^2(\mathbf{r}) = n_0^2(z) + \delta n^2(\mathbf{r}) = n_0^2(z) + \Delta n^2 S(\mathbf{r}). \tag{4.5}$$

$\Delta n^2 = n_p^2 - n^2$ is the dielectric constant contrast between the particle and its embedding medium while $n_0(z)$ is the vertical profile of refraction index of the system (Note that the atomic structure is implicitly neglected because of the smallness of the scattering angles). For a nanoparticle on a substrate, $n_0(z) = 1$ for $z > 0$ and $n_0(z) = n_s$ for $z < 0$; the dielectric contrast is: $\Delta n^2 = n_p^2 - 1$ (the refraction index of vacuum being 1). The scattering cross section[18,24,58] from $\mathbf{k}_i$ to $\mathbf{k}_f$ can be written as:

$$\frac{d\sigma}{d\Omega} = \frac{k_0^4}{16\pi^2} \left|n_p^2 - 1\right|^2 \left|\mathcal{F}(\mathbf{q}_\parallel, k_{i\,z,0}, k_{f\,z,0})\right|^2 , \tag{4.6}$$

where the DWBA form factor of the nanoparticle

$$\begin{aligned}\mathcal{F}(\mathbf{q}_\parallel, k_{i\,z,0}, k_{f\,z,0}) = \\ & F(\mathbf{q}_\parallel, k_{f\,z,0} - k_{i\,z,0}) \\ & + r^f F(\mathbf{q}_\parallel, -k_{f\,z,0} - k_{i\,z,0}) \\ & + r^i F(\mathbf{q}_\parallel, k_{f\,z,0} + k_{i\,z,0}) \\ & + r^i r^f F(\mathbf{q}_\parallel, -k_{f\,z,0} + k_{i\,z,0}).\end{aligned}$$

is given in terms of the Fourier transform of the particle shape:

$$F(\mathbf{q}) = \int_{S(\mathbf{r})} e^{i\mathbf{q}.\mathbf{r}} d\mathbf{r}. \tag{4.7}$$

Note in passing that the superscript f in the reflection coefficients means that they are evaluated for the time inverted scattering wave vector $-k_{f\,z,0}$. A simple interpretation of each term of Eq. 4.7 is given in Fig. 6 as the interference between elementary scattering paths . The first term is nothing else than the Born one *i.e.* the direct scattering by the particle as if it was isolated in vacuum. The other terms involve a reflection of either the incident or the scattered beams on the substrate surface; the actual perpendicular wavevector transfer should be used and the corresponding form factor should be weighted by the corresponding reflection coefficient. As an obvious consequence, at variance to scattering in vacuum, $\mathbf{q}$ alone is not sufficient to describe the scattering.

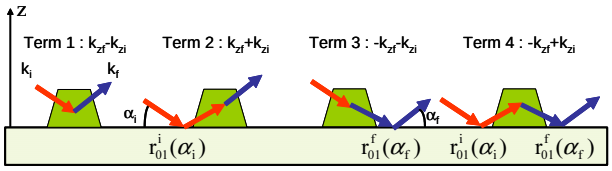

FIG. 6: "Diagrammatic" representation of the island scattering cross section in DWBA. Interpreted from Ref.[58].

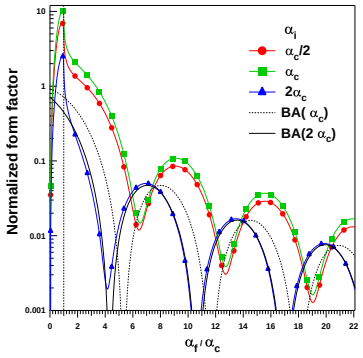

FIG. 7: DWBA form factor (Eq. 4.7) of a cylindrical nanoparticle as function of the emergence angle α_f/α_c and for several incidence angles. The intensity was normalized by the particle volume squared. As a matter of comparison, the Born form factor Eq. 4.7 is also plotted. Interpreted from Refs.[24],[18].

An enhancement of the intensity at $\alpha_f = \alpha_c$ appears in the typical plot of $\left|\mathcal{F}(\mathbf{q}_\parallel, k_{i\,z,0}, k_{f\,z,0})\right|^2$ of Fig. 7. This feature, known as the Yoneda peak[75], is due to the interplay between (i) the sharp variation of the amplitude and the phase of the reflection coefficients $r^{i,f}$ close to the critical angle α_c and (ii) the involved Fourier transforms $\mathcal{F}(\mathbf{q}_\parallel, \pm k_{i\,z,0}, \pm k_{f\,z,0})$. As shown in Fig. 8, except close to and below α_c, two contributions dominate the scattering for $\alpha_f > \alpha_c$: the Born one and that involving the reflection of the incident wave before scattering. The wavevector shift of $2k_{i\,z,0}$ between both combined with the behavior of r^i induce a blurring of the sharp interference fringes of the Born form factor; the zeros of $F(\mathbf{q}_z)$ become minima which positions depend on the incident angle α_i. The case

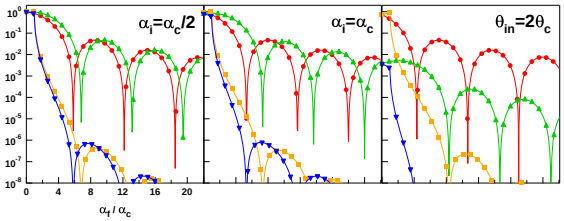

FIG. 8: Decomposition of the DWBA island form factor (Eq. 4.7) along the four scattering components shown in Fig. 6. The symbols ($\circ, \triangle, \triangledown, \square$) correspond to the four scattering events of Fig. 6 from left to right. Interpreted from Refs.[18,24].

of a nanoparticle on a thin layer on an infinite substrate is handled in a similar way and gives rise to (i) a coupling between the Kiessig fringes of the film and the oscillations of the form factor and (ii) a standing wave pattern below the critical angles of the substrate and the layer[95].

For substrates with an uncorrelated roughness, the Fresnel reflection coefficients may be modified by a decreasing exponential term depending on the Root Mean Square (rms) roughness, the z-component of the wave vector in vacuum and that of the wave vector in the substrate[40,59]. The form factor within the BA is recovered from the DWBA by setting $r(\alpha_i) = r(\alpha_f) = 0$. Hence, the BA is valid only when the reflection coefficients are negligible, *i.e.* when α_i and α_f are larger than $\simeq 3\alpha_c$. At powerful synchrotron facilities, it could be thought relevant to carry out GISAXS at $\alpha_i \gg \alpha_c$ so that some quick analysis could be done in the BA but at the expense of a loss of scattered intensity.

However, in this case, some information is lost for small q_z values, which may affect the result if the nanostructures are very high.
To conclude, as a general rule, when $\alpha_i, \alpha_f \gg \alpha_c$, the Born approximation is valid. For a matter of simplicity, in the following the discussion is most of the time restricted to the BA, which is almost valid when considering only the scattered intensity parallel to the surface.

4. The Fourier transform of particle shape

As shown in the earlier work of Von Laue[96,97], the 3D integral over the volume V in the particle form factor Eq. 4.7 can be transformed by means of the Green's theorem into a 2D integral over the particle surface S:

$$F(\mathbf{q}) = -\frac{1}{q^2}\int_S \frac{\partial e^{i\mathbf{q}.\mathbf{r}}}{\partial n} d^2\mathbf{r}, \tag{4.8}$$

in which $\frac{\partial}{\partial n}$ is the differentiation along the normal $\mathbf{n}$ (oriented outwards of the particle) of the surface element $d^2\mathbf{r}$. Noting $\mathbf{q}_n$ the component of $\mathbf{q}$ along $\mathbf{n}$, this becomes

$$F(\mathbf{q}) = -\frac{i}{q^2}\int_{S(\mathbf{r})} \mathbf{q}_n e^{i\mathbf{q}.\mathbf{r}} d^2\mathbf{r}. \tag{4.9}$$

The calculation can be further simplified if the crystal is bounded by a plane $\mathcal{P}$ for which $\mathbf{q}_n$ is constant; the contribution of this surface is:

$$F_{\mathcal{P}}(\mathbf{q}) = -\frac{i\mathbf{q}_n}{q^2} e^{i\mathbf{q}.\mathbf{r}_n} \int_{\mathcal{P}} e^{i\mathbf{q}.\mathbf{r}'} d^2\mathbf{r}'. \tag{4.10}$$

For a scattering vector oriented along the normal to the surface, the integral in the previous equation reduces to the area $S_{\mathcal{P}}$ of the plane $\mathcal{P}$ and $|F_{\mathcal{P}}(\mathbf{q})| = S_{\mathcal{P}}/q$ falls off inversely as q. Moving away from the surface normal at constant q, $F_{\mathcal{P}}(\mathbf{q})$ decreases rapidly. The spines (as Von Laue termed them) that extend along $\mathbf{q}_n$ (and its opposite direction because of the Friedel rule $|F(-\mathbf{q})| = |F(\mathbf{q})|$) are known as facet truncation rods. In an exactly analogous way, the surface integral in Eq. 4.10 can be casted into a line integral over the contour of the plane $\mathcal{P}$ and further simplified into the contribution of straight edges if any. Symmetry related faces or edges for polyhedrons can be paired and lead to pronounced interferences effects; intensity distribution have subsidiary spines in the direction perpendicular to well-defined edges. This reminds the notions of crystal truncation rod[38,39] in surface X-ray crystallography or of terrace truncation rod and step truncation rod for vicinal surfaces[19]. A clear experimental illustration of such phenomena in GISAXS was given by Vartanyants and coworkers[98] for Ge/Si quantum dots grown by liquid phase epitaxy.
A non-exhaustive library of $F(\mathbf{q})$ for basic shapes is given in Ref.[24]. If the particle displays special symmetries, the expression of $F(\mathbf{q})$ reduces to a 1D integral or is even fully analytical. Each particle is characterized by a set of characteristic zeros of the interference fringes as well as by a given Porod exponent[18] (see Sect. IV E 2 for definition and discussion).

5. Scattering from faceted particles

The rods of scattering by facets can be clearly revealed when one component of the wavevector transfer is perpendicular to the facet normal, which is achieved in GISAXS when the X-ray incident beam direction q_x is perpendicular to the facet normal. Fig. 9 shows the calculated scattering pattern of a square basis pyramidal particle which is typically encountered during the epitaxy of fcc metals on MgO(001). The particle is limited by (111) and (001) planes that make an angle of 54.7°. A scattering rod tilted by 54.7° from the surface normal shows up when the beam is aligned along the particle edge (Fig. 9-b). This anisotropic scattering feature disappears progressively upon rotation (Fig. 9-a) and broadening of the size distribution. If the base angle is increased up to 90° and the particle shape reaches that of a parallelepiped, this scattering rod becomes parallel to the $q_y \sim 2\theta$ axis.
This is illustrated on an experimental example in the Ag/MgO(001) system (Fig. 10). When the incident X-ray beam is along the [110] direction (Fig. 10-b), a scattering rod at 54.7° with respect to the surface normal is observed, corresponding to {111} side facets. It is not found when the beam is along the [100] direction (Fig. 10-a). Moreover, in the case of faceted nanostructures, a second and even sometimes third order scattering peaks perpendicular to the surface are present, indicative of a flat top (001) terrace and of a narrow height distribution. An additional feature

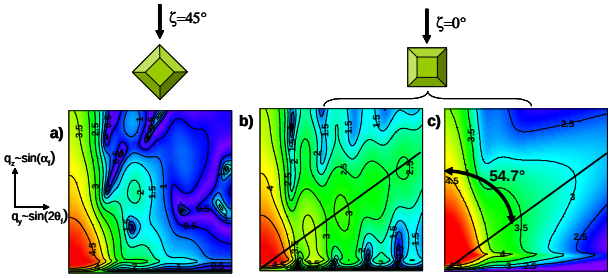

FIG. 9: Simulated GISAXS pattern of an square basis pyramidal island for two orientations ζ of the incoming beam with respect to the base edge: a) $\zeta = 0°$, b)c) $\zeta = 45°$. Patterns a,b corresponds to an isolated particle while in pattern-c a size distribution was accounted for. The angle between the lateral facet and the substrate surface is that between (111) and (001) planes in fcc lattice *i.e.* 54.7°. The scattering angles range between $0 < 2\theta, \alpha_f < 3°$ while $\alpha_i = \alpha_c$. The numerical parameters are $\lambda = 0.1$ nm, $R = H = 5$ nm. (Interpreted from Ref.[24])

can be deduced from a detailed comparison of Fig. 10-a with 10-b. Indeed, the intensity along the q_y direction, at the Yoneda peak position, is clearly larger when the X-ray beam is along [100] as compared to along [110]. This indicates that there is a scattering rod along the [010] direction. Hence, the Ag nanostructures also present {010} facets. All these features point to a truncated cubo-octahedron like average shape with {001}, {111}, and {010} facets, which is represented in the inset of Fig. 10-a.

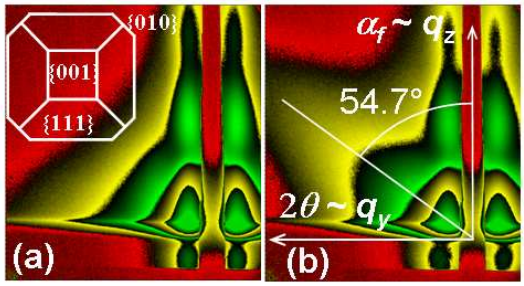

FIG. 10: GISAXS patterns of 2 nm of Ag deposited on a MgO(001) surface at 540 K, with the incident beam along the [100] a) and the [110] b) direction of the MgO(001) substrate. The intensity is represented on a logarithmic scale. Each black contour between two colors corresponds to an order of magnitude change in intensity. The q_y (respectively q_z) axis ranges from 0 to 2.7 nm^{-1} (respectively 3 nm^{-1}). Inset: top view of the truncated cubo-octahedron nanostructures shape with the {001}, {111}, and {010} facets. From Ref.[99].

6. Form factors of simple geometrical shapes

Information on the nanostructure shape can be gained from the symmetry properties that can be probed by rotating the sample around its surface normal. In addition, the shape of the nanostructures can, when it is simple enough, be directly inferred from simple characteristics of the form factor, as shown in Fig.11 for cylinders, truncated spheres and pyramids, according to the orientation of the incident x-ray beam. For a cylinder, the pattern is composed of well separated lobes along both parallel and perpendicular directions (see Fig. 11-a). For a complete sphere, one main zero order lobe is present, with a first order arc-shaped lobe (cf. Fig. 11-b). The 2D map for a complete pyramid is characterized by a main lobe elongated along the perpendicular direction with a monotonous intensity decrease. The case of pyramid-like nanostructures (cf. Fig. 11-c-e) has just been discussed.
Hence, a simple qualitative inspection of a 2D GISAXS pattern may allow a first guess of the average nanostructure shape, *e.g.*, symmetry, facets... Moreover, the inspection of the intensity zeros or minima may be of great help to determine the average size if the size distribution is sufficiently narrow[18]. Nevertheless, the size polydispersity is usually large and the above criteria are not sufficient. As discussed later, In simple case, the asymptotic behavior at high $\mathbf{q}$ may allow extracting the average shape. When this is not enough; a complete quantitative analysis of

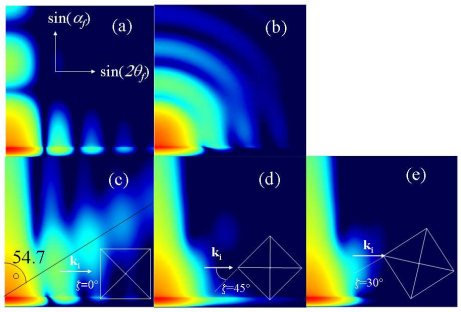

FIG. 11: The 2D $|\mathcal{F}(\mathbf{q})|^2$ factor calculated within the DWBA of a) a cylinder ($R = 5$ nm and $H/R = 1$), b) a complete sphere ($R = 5$ nm), c) a complete pyramid with $R = 5$ nm with the beam aligned along a face ($\zeta = 0°$), d) same as c) but with the beam aligned along an edge ($\zeta = 45°$), and e) same as c) but with $\zeta = 30°$. The intensity is represented on a logarithmic scale; 2θ and α_f angles range from 0 to 3°. $\lambda = 0.1$ nm. From Ref.[18].

the intensity evolution as a function of q_y and q_z becomes necessary to extract the nanostructure morphologycal characteristics.

7. *Miscellaneous remarks*

As expected from classical small angle scattering[100,101], the intensity is proportional to the contrast of dielectric constants between that of the embedding medium and that of the nanoparticles.
For very small angles $\alpha_i, \alpha_f \ll \alpha_c$, the smallness of $k_{i\,z}, k_{f\,z} \simeq 0$ allows the factorization for the island form factor Eq. 4.7:

$$\begin{aligned}\mathcal{F}(\mathbf{q}_\parallel, k_{i\,z}, k_{f\,z}) \simeq & \\ & F(\mathbf{q}_\parallel, 0)(1 + r^i_{0,1} + r^f_{0,1} + r^i_{0,1} r^f_{0,1}) \\ & = F(\mathbf{q}_\parallel, 0)(1 + r^i_{0,1})(1 + r^f_{0,1}) \\ & = F(\mathbf{q}_\parallel, 0) t^i_{0,1} t^f_{0,1}.\end{aligned}$$

and the DWBA expression for buried nanoparticles is recovered. Remarkably, this factorization is also possible for very small islands for which the two DWBA calculations (buried particles and particles on substrate) are equivalent.

8. *Link between coherence length and coherent and incoherent scattering cross sections*

If a well-collimated X-ray beam impinges at glancing angle on a rough sample, coherent scattering gives rise to a specularly reflected beam and a single refracted-transmitted beam, whereas incoherent scattering causes diffusely reflected and transmitted radiations. The question arise of how the scattered intensity is related to the statistical description of the sample although the sample morphology (roughnesses, fluctuations of density etc...) is by itself deterministic, and how the experimental imperfections are taken into account, in particular the finite angular and wavelength spreads of the incident beam and the angular aperture of the detector.

Let us first suppose that the incident and scattered beams are perfectly collimated. In the case of a perfect point like detector, the whole sample of size L scatters coherently; the pattern recorded as function of scattering angles involves spiky behavior, the so-called "speckle", with typical frequencies given by the inverse of the beam footprint on the sample. However, the experimental imperfections, in particular the wavelength spread $\Delta\lambda$, the beam divergences in-plane $\Delta\alpha_i$ and out-of-plane $\Delta 2\theta_i$ and the finite detector acceptance $\Delta\alpha_f, \Delta 2\theta$, make necessary the introduction of the coherence length of the x-ray beam L_{coh} at the sample surface (see Fig. 12). Above this distance, the field emitted by two dipoles at the surface are no more phase matched and interfere no more coherently in the far field (detector). Therefore, the collected intensity over the solid angle $\Delta\Omega = \Delta\alpha_f \Delta 2\theta$ is given apparently by an incoherent sum of intensities scattered by domains of size L_{coh}. The speckle behavior is replaced by a continuous average intensity if the illuminated area A_i or beam footprint contains a large number of coherent domains. The smearing of the speckles can be understood as the folding of the scattering with the instrumental resolution function[40,80]. Three

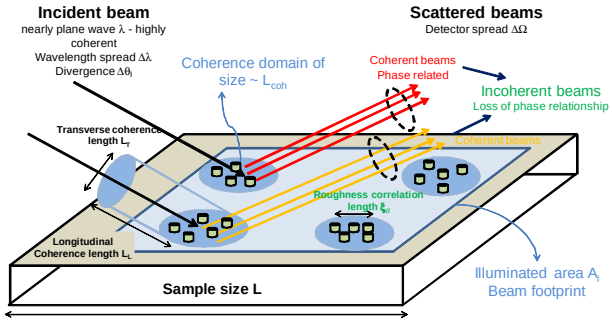

FIG. 12: Sketch of the interplay between coherence domains, statistical properties of the sample roughness and diffuse scattering.

lengths define the volume of coherence of the incident beam[59]: the transverse coherence lengths $L_{T,\alpha_i} = \lambda/2\Delta\alpha_i$, $L_{T,2\theta_i} = \lambda/2\Delta 2\theta_i$ and the longitudinal one $L_L = \lambda^2/2\Delta\lambda$. Due to the grazing geometry, a projection effect increases L_{T,α_i} by a factor $1/\sin(\alpha_i)$. The detector spread gives rise to similar length definitions L_{T,α_f}, $L_{T,2\theta}$. An other important assumption is that the coherent domains are sufficiently large so that all domains have exactly the same statistical properties, provided that the sample is spatially homogeneous. To sum up, if the following inequalities are fulfilled $L \geq \sqrt{A_i} \gg L_{coh} \gg \xi_{\parallel}$ for a surface characterized by an in-plane correlation length $\xi_{\parallel}$, the scattering cross section can be obtained by an ensemble average along the surface. The system is called ergodic if the scattered intensity from one deterministic sample accounting for the measurement imperfections is equivalent to an average over many samples. From now on, this hypothesis is assumed to be fulfilled. Indeed, the standard figures on a synchrotron beamline are:

- $\lambda/\Delta\lambda \sim 10^4$, $L_L \sim 0.5\,\mu$m,
- $\Delta\alpha_i \sim 0.5\,$mrad, $L_{T,\alpha_i} \sim 0.1\,\mu$m, $L_{T,\alpha_i}/\sin(\alpha_i) \sim 30\,\mu$m
- $\Delta 2\theta_i \sim 0.1\,$mrad, $L_{T,2\theta_i} \sim 0.5\,\mu$m
- $\Delta\alpha_f \sim \Delta 2\theta \sim 5\,10^{-5}\,$mrad, $L_{T,\alpha_f} \sim L_{T,2\alpha_f} \sim 1\,\mu$m
- $A_i \sim 300 \times 1000\,\mu$m^2

for $\lambda \sim 0.1\,$nm, $\alpha_i \sim 0.2°$ a 2D CCD detector pixel size of $50\,\mu$m and a sample-detector distance of 1 m. As a consequence, $\xi_{\parallel}$ should be smaller than a few hundreds of nm. A more rigorous treatment of the interplay between coherence and instrumental resolution function relies on the notion of mutual coherence function; the interested reader can refer to Refs.[102–105] and references therein. This theoretical problem was renewed during the last decade with the advent of scattering experiments with highly coherent beams.
Hence, under our experimental conditions, the beam is said incoherent over its size, and an ensemble average of the calculated cross section has to be performed for comparison with the experimental data. When doing this, the average value $\langle \delta n^2(\mathbf{r}) \rangle$ can be isolated:

$$\left\langle \left| \delta n^2(\mathbf{r}) \right|^2 \right\rangle = \left| \langle \delta n^2(\mathbf{r}) \rangle \right|^2 + \left\langle \left| \Delta\delta n^2(\mathbf{r}) \right|^2 \right\rangle \tag{4.11}$$

with $\delta n^2(\mathbf{r}) = \langle \delta n^2(\mathbf{r}) \rangle + \Delta\delta n^2(\mathbf{r})$. As a results, two contributions appear in the total cross section:

$$\left(\frac{d\sigma}{d\Omega}\right)_{tot} = \left(\frac{d\sigma}{d\Omega}\right)_{coh} \left(\left| \langle \delta n^2(\mathbf{r}) \rangle \right|^2 \right) + \left(\frac{d\sigma}{d\Omega}\right)_{incoh} \left(\left\langle \left| \Delta\delta n^2(\mathbf{r}) \right|^2 \right\rangle \right). \tag{4.12}$$

The first one is called the "coherent intensity" and the second one is known as "incoherent, diffuse or non-specular intensity". The incoherent scattering is due to variations of the dielectric index with respect to the average one[106]. If the surface inhomogeneity or roughness is statistically homogeneous and random along the sample plane, $\langle \delta n^2(\mathbf{r}) \rangle = \delta n^2(z)$ is a function of only the $z-$coordinate; the coherent cross section is thus a Dirac peak at $q_{\parallel} = k_{f,\parallel} - k_{i,\parallel} = 0$ (see for instance, the Born cross section Eq. 4.1). For this reason, it is also called specular intensity or specular rod. However, one has to bear in mind that because of all the resolution imperfections, both cross sections mix up along the specular rod giving rise to a finite width of the rod inversely proportional to the coherence length L_{coh}. In other words, there is diffuse scattering along the specular direction.

C. Accounting for the particle-particle correlations : concentrated assembly of nanoparticles

1. Introduction

When the particle concentration increases, the waves scattered by different particles can interfere in a way that depends on their spatial organization, their size and shape distribution and on the coupling between both, which is described in many textbooks dealing with X-ray scattering or diffraction from crystals[77,78,97,100], amorphous materials[107] or nanoparticles in bulk[100,101]. The most important points are recalled below for particles lying in a plane. We refer to *e.g.* Refs.[93] for the case of particles assembled in 3D. Another complexity arises because for shallow angles, which will be treated later when presenting the model of the graded interface: the scattered wave may be scattered again by an other particle *e.g.* the layer of particles itself influences the propagation of the incident and scattered waves.

2. General formalism of the partial interference functions : coherent versus incoherent scattering

For a large numver N of particles of shape $S_i(\mathbf{r})$ located at $\mathbf{r}_{\parallel\, i}$, the scattering potential is:

$$\delta n^2(\mathbf{r}) = \Delta n^2 \sum_{i=1}^{N} S_i(\mathbf{r}) \otimes \delta(\mathbf{r} - \mathbf{r}_{\parallel,i}). \tag{4.13}$$

$\otimes$ stands for the folding product; the dielectric contrast Δn^2 varies from one type of morphology to another. Taking benefit of the decoupling between the parallel and perpendicular directions in DWBA, scattering cross section may be written:

$$\begin{aligned}\left(\frac{d\sigma}{d\Omega}\right)_{tot} &= \frac{k_0^4}{16\pi^2}|\Delta n^2|^2 N \left(\frac{d\sigma}{d\Omega}\right)_{part}, \\ \left(\frac{d\sigma}{d\Omega}\right)_{part} &= \frac{1}{N}\left|\sum_{i=1}^{N} \mathcal{F}_i(\mathbf{q}_\parallel, k_{i\,z}, k_{f\,z}) e^{i\mathbf{q}_\parallel \cdot \mathbf{r}_{\parallel\, i}}\right|^2 .\end{aligned} \tag{4.14}$$

As just discussed, a real measurement is sensitive only to an ensemble average $\langle \ldots \rangle$ of the cross section per particle over the "coherent domains". The size of the coherent domains A_{coh} is limited by the coherence of the incident beam (wavelength spread and angular divergence) and by the angular resolution of the detector. If A_{coh} is sufficiently large (but still smaller than the footprint of the incident beam) and if the sample is homogeneous, it is possible to use statistical quantities that are representative of all the sample. The particles can be sorted out by classes α of size and shape with a probability density p_α, while their relative positions can be described through the reduced partial pair correlation functions $g_{\alpha\beta}(\mathbf{r}_\parallel)$. According to Faber and Ziman[107,108], if n_S is the number of particles per surface unit, $n_S p_\beta g_{\alpha\beta}(\mathbf{r}_\parallel) d\mathbf{r}_\parallel$ is the number of particles of kind β at a position $\mathbf{r}_\parallel$ from a central one of kind α. $g_{\alpha\beta}(\mathbf{r}_\parallel) = g_{\beta\alpha}(\mathbf{r}_\parallel)$ and $g_{\alpha\beta}(\mathbf{r}_\parallel \to \infty) \simeq 1$ for disordered systems. The ensemble average of Eq. 4.14 can be written in the form[24,100,101]:

$$\begin{aligned}\left(\frac{d\sigma}{d\Omega}\right)_{part} = N\left|\left\langle \mathcal{F}(q_\parallel = 0, k_{i\,z}, k_{f\,z})\right\rangle\right|^2 \delta(q_\parallel) \\ + \Phi_0(\mathbf{q}_\parallel, k_{i\,z}, k_{f\,z}) \\ + \sum_{\alpha,\beta} p_\alpha p_\beta \mathcal{F}_\alpha(\mathbf{q}_\parallel, k_{i\,z}, k_{f\,z}) \mathcal{F}^*_\beta(\mathbf{q}_\parallel, k_{i\,z}, k_{f\,z}) S_{\alpha\beta}(\mathbf{q}_\parallel),\end{aligned}$$

$$\Phi_0(\mathbf{q}_\parallel, k_{i\,z}, k_{f\,z}) = \left\langle \left|\mathcal{F}(\mathbf{q}_\parallel, k_{i\,z}, k_{f\,z})\right|^2 \right\rangle - \left|\left\langle \mathcal{F}(\mathbf{q}_\parallel, k_{i\,z}, k_{f\,z})\right\rangle\right|^2,$$

$$S_{\alpha\beta}(\mathbf{q}_\parallel) = 1 + n_S \int_A \left(g_{\alpha\beta}(\mathbf{r}_\parallel) - 1\right) e^{i\mathbf{q}_\parallel \cdot \mathbf{r}_\parallel} d\mathbf{r}_\parallel .$$

$\langle \ldots \rangle$ is the average over the size-shape distribution p_α. The star symbol corresponds to the complex conjugate. The partial interference function $S_{\alpha\beta}(\mathbf{q}_\parallel) - 1$ appears as the Fourier transform of $g_{\alpha\beta}(\mathbf{r}_\parallel) - 1$. The -1-term in the above equation singles out the oscillatory behavior of $g_{\alpha\beta}(\mathbf{r}_\parallel)$ around its asymptotic value.
Three terms appear in the above cross section:

(i) a "specular rod" at $q_\parallel \simeq 0$. This term is proportional to the number of particles in the "coherent domain" ($n_S \int_{A_{coh}} e^{i\mathbf{q}_\parallel \cdot \mathbf{r}_\parallel} d\mathbf{r}_\parallel \to N\delta(q_\parallel)$ when $A_{coh} \to \infty$) and is modulated by the particle form factor at $q_\parallel = 0$. The specularly reflected beam adds up on this rod at $\alpha_f = \alpha_i$. The shape of this rod is given by all sources of coherence loss. Scarcely measured in GISAXS geometry as it is hidden by the beam stop, the specular rod intensity can be integrated through offset scans in reflectivity.

(ii) an incoherent term $\Phi_0(\mathbf{q}_\parallel, k_{i\,z}, k_{f\,z})$ due to the fluctuations of sizes and shapes of particles. An analogy can be drawn with the incoherent neutron scattering length due to isotopic effects or the Debye-Waller-like uncorrelated thermal background[59,77,78].

(iii) a coherent term that includes the interferences between waves scattered by different particles.

The practical use of the above equations for data analysis is hampered by the lack of knowledge of all the partial pair correlation functions. Modeling $g_{\alpha\beta}(\mathbf{r}_\parallel)$ would require a knowledge of the correlations of location between particles of different sizes or shapes, which is beyond the scope of a simple analysis of experimental GISAXS patterns. Analytical results about small angle scattering by systems of interacting polydispersed particles have been obtained only for hard spheres in 3D[109–111]. The use of fluid thermodynamics theory applied to mixtures of different components with arbitrary interaction potential is restricted only to very few components because of the cumbersome resolution of coupled integro-differential equations. Moreover, in many cases, interaction potentials between particles are unknown if they are relevant. For instance, the spreading of islands grown on a substrate results from a subtle interplay between random nucleation process, growth and coalescence kinetics, strain effect etc... that can not be traced back to a "potential". This is one of the reason of the use of approximations to handle the problem of partial pair correlation functions. To go further the size and spatial correlations between neighboring particles must be precisely known. For instance MBE growth of nanostructures leads usually to a depleted zone (capture area) around each particle[35,112,113] which scales with the particle size. Because it is in general impossible to describe the system in terms of partial correlation function, approximations are required. We briefly present below the two most commonly used: the Decoupling Approximation and the Local Monodisperse Approximation. Two more sophisticated approximations (Size-Spacing Coupling and Scaling) will be discussed later.

3. Decoupling Approximation

The Decoupling Approximation (DA)[77] consists in neglecting all the correlations between the kind of scatterers and their relative location. As sketched in Fig. 13, DA offers no restriction about particle overlap as a consequence of the

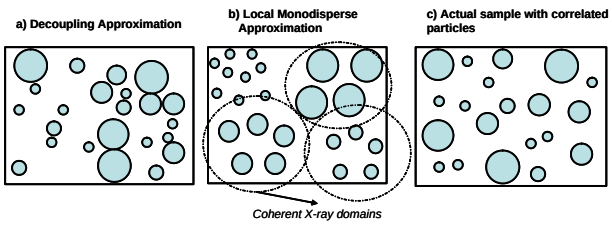

FIG. 13: Sketch of the morphology that would correspond to various approximations used to treat scattering from an ensemble of nanoparticles.

underlying unrestricted disorder. DA is known in the theory of liquid mixture as the Random Mixture Approximation.

With this approximation of completely uncorrelated spatial disorder, all the partial pair correlation $g_{\alpha\beta}(\mathbf{r}_\parallel)$ are replaced by a common function $g(\mathbf{r}_\parallel)$ obtained for a suitable monodisperse system[114]:

$$\left(\frac{d\sigma}{d\Omega}\right)_{part} = \Phi_0(\mathbf{q}_\parallel) + \left|\left\langle \mathcal{F}(\mathbf{q}_\parallel, k_{i\,z}, k_{f\,z})\right\rangle\right|^2 S(\mathbf{q}_\parallel), \tag{4.15}$$

$$S(\mathbf{q}_\parallel) = 1 + n_S \int_A \left(g(\mathbf{r}_\parallel) - 1\right) e^{i\mathbf{q}_\parallel \cdot \mathbf{r}_\parallel} d\mathbf{r}_\parallel. \tag{4.16}$$

$S(\mathbf{q}_\parallel)$, the Fourier transform of the total reduced pair correlation function, is known as the total interference function irrespective of the particles type (see Sect. IV C 5).

The first successful numerical applications of DA to colloid fluid was made by Kotlarchy and Chen[115]. The authors already noticed that the applicability of the modeling was restricted to low concentration or low size polydispersity. In fact, DA overestimates the diffuse scattering[18] close to the specular rod because of the too intense incoherent contribution $\Phi_0(q_\parallel)$.

4. Local Monodisperse Approximation

This approximation introduced by Pedersen[116–119] is widely used to analyze scattering from correlated systems. At variance to the DA, a nearly perfect correlation between the size and shape of neighboring particles is assumed[120]. As the monodisperse domains interfere incoherently, the LMA cross section reads:

$$\left(\frac{d\sigma}{d\Omega}\right)_{part} = \left\langle \left|\mathcal{F}_D(\mathbf{q}_\parallel, k_{i\,z}, k_{f\,z})\right|^2 S_D(\mathbf{q}_\parallel)\right\rangle_D . \tag{4.17}$$

where $\langle \ldots \rangle_D$ is the average over the domain D in which the local interference function $S_D(\mathbf{q}_\parallel)$ can depend on the particle size.

Hence, the intensity in LMA is obtained as the incoherent sum of scattering by each domain weighted according to the actual size-shape distribution p_α. As the interference function of each sub-system $S_D(\mathbf{q}_\parallel)$ can be scaled on the particle size, LMA is, in practice, an efficient way to reintroduce partial correlation between particles, in particular the excluded volume effect. Pedersen[116] suggested to use for $S_D(\mathbf{q}_\parallel)$ the hard core interacting one (see Sect. IV C 5) with an excluded volume that scales linearly with the actual particle size. This mimics the expected behavior of the capture area of each particle during growth.

The LMA cross section Eq. 4.17 can be recovered from the most general expression above by assuming no correlation between particles of different kinds *i.e.* $g_{\alpha\beta}(\mathbf{r}_\parallel) = 0$ if $\alpha \neq \beta$, and that $S_\alpha^{mono}(\mathbf{q}_\parallel)$ can be replaced by the interference function $S_D(\mathbf{q}_\parallel)$ of a truly monodisperse system of density $n_S p_\alpha$. In other words, $g_{\alpha\alpha}(\mathbf{r}_\parallel)$ is assumed to be the pair correlation function of a monodisperse domain although by definition, it includes the existence of the other kinds of particles. Pedersen justified this approximation on the ground of a physical picture of slow variation of the size of the particles at a length scale lower than the coherence length (see Fig. 13). This means that each particle is surrounded by neighbors of the same size and shape. The accuracy of LMA in 3D was tested against scattering from computer generated polydisperse systems[119,121] as well as the solvable Vrij scattering from hard core interacting spheres[114]. The failure of DA even at very small polydispersity was evident not only at small q but also from the shape of the correlation peak. LMA gives better agreement but without reproducing exactly the first peak shape. As will be discussed later in 1D[120], a smooth transition between DA and LMA can be obtained by gradually increasing the size correlation between neighbors.

5. The interference function

a. introduction As usual in X-ray crystallography[77], for a collection of particles, two kinds of disorders can be distinguished, leading to different behaviors of the interference function. The disorder of the first kind keeps the long range order in the system and gives rise only to a decrease of the Bragg peaks intensity at high angles while the disorder of the second kind is characterized by a broadening of the peaks at high angles due to a progressive loss of correlation between particle positions.

b. Pair correlation function in disordered systems Disordered systems characterized by the loss of long range order are defined by their reduced total pair correlation function $g(\mathbf{r}_\parallel)$. For an homogeneous system, it depends only on the relative position of the scatterers irrespective of their size or shape. The autocorrelation of the particle position $z(\mathbf{r}_\parallel)$ is related to $g(\mathbf{r}_\parallel)$ through:

$$z(\mathbf{r}_\parallel) = \frac{1}{N}\left\langle \sum_{i,j} \delta(\mathbf{r}_\parallel - \mathbf{r}_{\parallel,i} + \mathbf{r}_{\parallel,j})\right\rangle = \delta(\mathbf{r}_\parallel) + n_S g(\mathbf{r}_\parallel). \tag{4.18}$$

as $n_S g(\mathbf{r}_\parallel)$ counts the number of particles per surface unit located at $\mathbf{r}_\parallel$ from a central one. The average value n_S is often singled out to enhance the oscillatory part of $g(\mathbf{r}_\parallel)$ around its mean value: $z(\mathbf{r}_\parallel) = \delta(\mathbf{r}_\parallel) + n_S + n_S(g(\mathbf{r}_\parallel) - 1)$.

By Fourier transform of the last equation, the total interference function $S(\mathbf{q}_\parallel)$ shows up:

$$S(\mathbf{q}_\parallel) = 1 + N\delta(\mathbf{q}_\parallel) + n_S \int_A \left[g(\mathbf{r}_\parallel) - 1\right] e^{i\mathbf{q}_\parallel \cdot \mathbf{r}_\parallel} d\mathbf{r}_\parallel. \tag{4.19}$$

Once broadened by limited instrumental resolution, the $N\delta(\mathbf{q}_\parallel)$ term is nothing else than the specular rod which is often dropped in the interference function as its is hidden by the beam stop. For 2D isotropic samples, $g(r_\parallel)$ and $S(q_\parallel)$ depend only on the modulii $r_\parallel$ and $q_\parallel$ and are related through a Hankel transform:

$$S(q_\parallel) = 1 + N\delta(q_\parallel) + n_S \int_A \left[g(r_\parallel) - 1\right] J_0(q_\parallel r_\parallel) r_\parallel dr_\parallel. \tag{4.20}$$

In a general way, $g(r_\parallel)$ (respectively $S(q_\parallel)$) shows broader and broader peaks upon increasing $r_\parallel$ (respectively $q_\parallel$) which spacings are related to the mean distance between particles D (its inverse $2\pi/D$) while $g(r_\parallel), S(q_\parallel) \to 1$ when $r_\parallel, q_\parallel \to +\infty$. Practical modeling of $g(r_\parallel)$ function relies on the interaction between particles. Theoretical models like the Percus-Yevick or the hyper-netted chain approximations were developed in the field of fluids thermodynamics[122] to compute $g(r_\parallel)$ from the pair potential interaction between molecules. The most simple case is that of particles interacting through a hard core potential. It is analytical in 3D while only approximate solution are known in 2D[123]. From Fig. 14, a preferential ordering at a distance equal to the diameter is observed. However, depending on the studied system and the elaboration method, particles (in particular in hard condensed matter) do not interact through a well defined potential and the correlations between particles (size and spacing) are dominated by kinetic effects (*e.g.* random nucleation process).

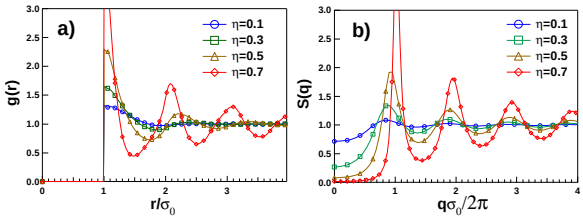

FIG. 14: a) Pair correlation function $g(r_\parallel)$ and b) interference function $S(q_\parallel)$ of hard core interacting disks of diameter σ_0 as function of the surface coverage η.

c. Scattering by ordered systems As in conventional crystallography, scattering or more precisely diffraction by an ordered lattice of particles gives rise to Bragg peaks at the nodes of the reciprocal lattice defined with two basis vectors $\mathbf{a}^*$ and $\mathbf{b}^*$ The total interference function is made of sharp Bragg rods extending perpendicular to the surface:

$$S(\mathbf{q}_\parallel) = \sum_n \sum_m \mathcal{S}(\mathbf{q}_\parallel - n\mathbf{a}^* - m\mathbf{b}^*). \tag{4.21}$$

For perfectly organized particles, the in-plane rod shape $\mathcal{S}$ is a Dirac peak; in practice, those rods are broadened by defects, by finite size effects and by limited coherence of the beam. Their shape depends on the prevailing disorders[24] and the inverse of their width is a direct measure of the coherence length of the lattice. In the case of diffraction by a super lattice of particles, the curvature of the Ewald sphere is no more negligible contrary to disordered systems for which the approximation $q_\parallel \simeq q_y$ is appropriate. Some experimental illustrations are given later for patterned silicon substrates or for the self-organized growth of Co/Au(111).

d. Paracrystalline domains The paracrystalline description of scattering[77–79,124–126] belongs to the second kind of disorder. The paracrystal lattice of nodes is a one-dimensional Markov chain where the loss of long range order is introduced in a cumulative way from point to point through the knowledge of the distance probability $p(x)$ between two neighboring nodes. The corresponding (1D) interference function is given by:

$$S(q) = \mathrm{Re}\left[\frac{1 + \mathcal{P}(q)}{1 - \mathcal{P}(q)}\right]. \tag{4.22}$$

where $\mathcal{P}(q)$ is the characteristic function of the probability law $p(x)$ *i.e.* its Fourier transform. Finite size effects can be easily accounted for by restricting the sum to a given number of nodes[79,127–130]. For normally distributed

distances,

$$p(x) = \frac{1}{\sigma_D\sqrt{2\pi}} e^{-\frac{(x-D)^2}{2\sigma_D^2}}, \quad \mathcal{P}(q) = e^{\pi q^2 \sigma_D^2} e^{iqD}. \tag{4.23}$$

the interference function is known as the Hosemann one[79,124]:

$$S(q) = \frac{1-\phi(q)^2}{1+\phi(q)^2 - 2\phi(q)\cos(qD)}, \quad \phi(q) = \exp\left[\pi q^2 \sigma^2\right]. \tag{4.24}$$

As shown in Fig. 15, the reflections get broader and broader upon increasing the width of the distance distribution σ. The generalization to higher dimensions[79,131,132] is possible only in the framework of the perfect paracrystal for

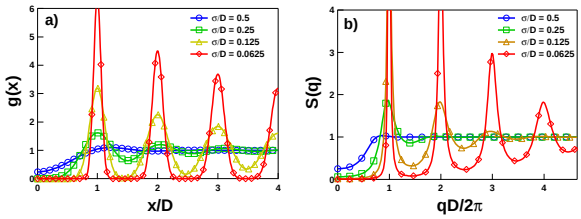

FIG. 15: a) Pair correlation function $g(x)$ and b) interference function $S(q)$ of a paracrystral with Gaussian statistics. σ and D are respectively the square-root of the variance and the mean value of the distance probability. The curves are plotted against normalized units. From Ref.[24].

which the unit cells are parallelograms. The inherent restriction is the uncoupling of the distance distributions along all directions of space. This leads to an unphysical divergence of the scattering close to the origin and to scattering patterns that do not fulfill the symmetry of the mean unit cell. Those drawbacks can be cured by finite size effects[79,129] and a symmetrisation procedure[133]. Averaging over orientations allows to define a radial pair correlation function in dimension higher than one[24,127,128].

Among others, several applications of the paracrystal modeling to GISAXS data analysis can be found in Refs. [20,21,94,134–136]. Scattering from stepped surfaces (see Ref. [19] and references therein) is a special application of such paracrystal modeling for which the distances between neighboring terraces is exactly related to their sizes.

e. The problem of the interference function Many theoretical or *ad hoc* interference functions (or equivalently pair correlation functions) can be used to analyze the GISAXS data[24]. The most usual are the Debye hard core[77] interference function, the Gaussian pair correlation function[137], the Lennard-Jones pair correlation function[100], the gate pair correlation function, the Debye hard core with power-law decrease[77], the Zhu pair correlation function[138], the Venables pair correlation function[139], or the bidimensional hard core pair function[123]. Some other very useful interference functions are those deduced from 1D or 2D paracrystals just discussed. If the relative positions of the nanostructures could result from an interaction pair potential, the pair correlation function could be deduced using a thermodynamics approach based on an interacting gas[122], if the system is at equilibrium and nearly monodisperse. However, the repartition of nanostructures grown on substrates is often the result of many competing phenomena that are dominated by the kinetic conditions and thermodynamic trends, so that the notion of "interaction potential" between nanostructures is meaningless. As a result, in many cases, none of these functions allow to satisfactorily reproduce the exact shape of the first maximum of the GISAXS data parallel to the surface, as well as the intensity evolution close to the origin of reciprocal space. It might then be useful to resort to an *ad hoc* interference function deduced from other experimental investigations such as plane view transmission electron microscopy (TEM), scanning electron microscopy (SEM) or Atomic Force Microscopy (AFM) data. Such an analysis has been performed in the cases of Pd and Ag deposited on MgO(001)[18,99,140,141]. Digitalized TEM plane views of some representative deposits were used to define an *ad hoc* interference function. Large scale pictures with a few thousands of nanostructures allowed to derive the nanostructure pair correlation function, $g(r)$. The interference function $S(q_{\|})$ deduced by Fourier transform was fitted with a two parameter (the average inter-nanostructure distance D and a disorder parameter σ) function in order to introduce it in the fit procedure. Ultimately, this function, determined on the final deposits, was found much more appropriate than the model functions to fit the GISAXS data for all deposits.

f. Nanostructures spacing and maximum of the interference function In many simple GISAXS analysis[43,44,50], the average inter-nanostructure distance D is determined through the position of the GISAXS intensity maximum q_m by $D = 2\pi/q_m$. However, as the GISAXS intensity is the product of the interference function $S(q_y)$ by the square modulus of the form factor, the GISAXS peak position q_m is shifted from the $S(q_y)$ peak position noted q_p

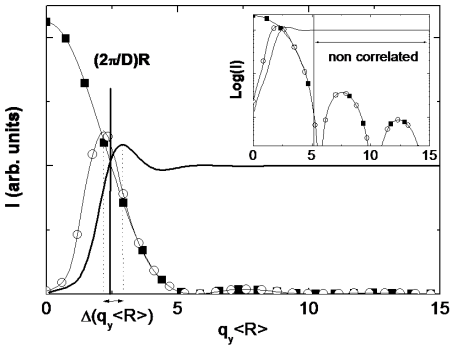

FIG. 16: Open circles: GISAXS intensity calculated within the BA as function of the parallel wavevector transfer $q_y \langle R \rangle$ and at $\alpha_f = 0$ for cylindrical nanostructures on a substrate in a disordered state. Filled squares: form factor of a cylinder. Continuous line: interference function with a distance between nanostructures of $D = 2.4 \langle R \rangle$. The difference between the maximum of the interference function and that of the GISAXS intensity is $\Delta q_y \langle R \rangle$. The inset shows the same evolution with the y-axis on a logarithmic scale. From Ref. [18].

accordingly to the form factor slope. This behavior is illustrated in Fig. 16 within the typical context of metal/oxide studies[16,18] for cylindrical nanostructures of mean radius $\langle R \rangle = 7.5$ nm. The GISAXS intensity maximum is located at $q_m \langle R \rangle = 2.20$, corresponding to a distance of $2\pi/q_m = 21.5$ nm, whereas the maximum of the interference function (evaluated from TEM) is at $q_p \langle R \rangle = 2.92$, which corresponds to a distance of $2\pi/q_p = 16.2$ nm. There is a large discrepancy between these two distances. Nevertheless, the distance determination from the interference function by $2\pi/q_p$ is not exact either, as the exact mean inter-nanostructure distance from the TEM analysis is $D = 18.0$ nm. As a consequence, in order to get a precise determination of the mean inter-nanostructure distance, it is extremely important to fit the experimental scattered intensity with an adequate model for the interference function.

6. Two other approximations: Size-Spacing Correlation Approximation and Scaling Approximation

a. introduction The two above approximations, DA and LMA, allow describing the scattering in a simple way, by separating the form factor from the interference function. However, they rely on two oppposite hypotheses which are often both unphysical. As already discussed, for the case of a disordered assembly of nanoparticles obtained by physical deposition from an atomic vapour on a substrate, the whole nucleation and growth process (resulting from adsoption, diffusion, evaporation, nucleation, aggregation, coalescence processes) leads in general to assemblies in which large (small) particles are farther (closer) to each other. On the contrary, in the case of organized growth on a patterned substrate having a regular network of nucleation-growth sites, larger islands tend to be surrounded by smaller ones. Hence, in general the sizes of neigboring particles can be correlated to each other as well as are to their spacing. We discuss below two approximations that have been developed to acccount for these size-size or size-spacing correlations.

b. The Size-Spacing Correlation Approximation (SSCA) The Size-Spacing Correlation approximation (SSCA)[21,120,135] is a one-dimensional analytical modeling of scattering from correlated particles that gives a fairly good illustration of the problem at hand although its applicability to actual measurements[135] is questionable owing to its 1D character. SSCA is derived from the paracrystal (see Sect. IV C 5) by filling nodes along a line with polydispersed particles and by accounting for a coupling between the sizes of two neighbors and their spacing on a statistical point of view (the reader is refered to the publications[21,25,120,135] for details). The contribution of coupling between the sizes and the spacing of neighboring scatterers in SSCA[21,120] is illustrated in Fig. 17 for several values of the parameter κ describing this coupling. Of course, whatever the approximation, the scattering at high wavevector transfer ($q_{\|} \gg 2\pi/D$) is only given by the mean form factor. In disordered systems, the introduction of correlations leads to a strong modification of the shape of the correlation peak as compared to DA or LMA. Its smearing lies in the contribution of all the partial interference functions[120] while its position is no longer simply related to the mean particle spacing D. For a constant average spacing D, the peak position shifts toward low $q_{\|}$ value upon increasing the coupling, until merging with the specular rod.

The model was also used to model 2D GISAXS, for which an interesting cross coupling between the parallel 2θ and perpendicular α_f directions has been evidence (see Fig. 17-b) for 3D particles of fixed aspect ratio. Because the

largest (and thus highest) particles are farther apart, they scatter closer to the specular rod and to the sample horizon. As a result, the scattering lobes along α_f are tilted toward the origin, even though the particles were modelled as cylinders. The tilt angle can be used as a measure of the coupling parameter between size and distance of particles if the particle aspect ratio is constant, which is the case when the thermodynamic equilibrium shape is reached[99]. A

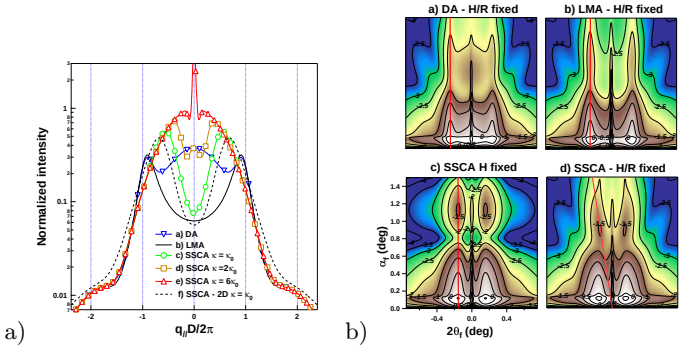

FIG. 17: Scattering from a line of size distributed cylinders. The size distribution and intrinsic fluctuations of distances are normal with $\sigma_R/R = \sigma_D/D = 0.25$ and $D = 3\langle R\rangle$. Either the particle aspect ratio is constant $H/R = 1$ or its height $H/\langle R\rangle = 1$ *i.e.* that the particle volume scales with R^3 or R^2. modeling has been performed in DA, LMA or SSCA using the same underlying paracrystal. κ_0 is the correlation parameter between average separation and sizes of neighboring nanoparticles. The intensity is normalized by $\langle V^2\rangle$. a) 1D cut of intensity at $q_\perp = 0$ for different κ values. b) Simulated GISAXS patterns for supported gold particles on $TiO_2(110)$. From Ref.[21]

comparison between SSCA and LMA including correlations through a linear link between the inter-particle distance and the size in each monodisperse domain was done in Ref.[21,135]. The main conclusion was that D between LMA and SSCA differs by 10-30% while the discrepancies on the other parameters (κ and σ_D) are larger. The interesting finding was that LMA and SSCA agree nearly perfectly on the estimate of the total fluctuations of particle spacing but not on its decomposition into paracrystal plus size distribution.
Strictly speaking, SSCA can not be used to analyze actual data. However, experimentally in the case of gold islands on $TiO_2(110)$[135], SSCA and LMA were compared assuming interference functions given by the 1D paracrystal or by a 2D function deduced from hard core interacting disks model[123] (Fig. 14) with a hard core radius that scales linearly with the actual radius[116]. The introduction of correlations was mandatory to reproduce the shape of the correlation peak. In the high $q_{\|}$ range *i.e.* where the average particle form factor is suitably fitted, LMA and SSCA agree within the error bars on the most important parameters $\langle R\rangle, \sigma_R$ and D, giving confidence in their evolution. The discrepancies comes only from the disorder description κ, σ_D. Both LMA and SSCA end up with a Voronoï cell size which is fully determined by the radius of the central particle. This finding is in line with what is expected from the growth theory of supported nanoparticles and with the overall self similar behavior that was observed in this system[142].

c. The Scaling approximation (SA) The Scaling Approximation (SA) is an approximation introduced by Gazzillo et al[114,143], which assumes a conformality of all the partial pair correlation functions according to $g_{\alpha\beta}(r) \simeq g_{mono}(r^*\lambda_{\alpha\beta})$; where g_{mono} is the pair correlation function of a monodisperse system which is assumed to depend only on a reduced distance r^*. For particles interacting through a pair potential, SA is a further step after the hypothesis of conformal mixtures for which it is the interaction potential itself $u_{\alpha\beta}(r)$ which is conformal to that of a monodisperse reference system. This conformality hypothesis is well suited to particles interacting through an hard core potential for which $u_{\alpha\beta}(r) = 0$ if $r < \sigma_{\alpha\beta}$ and $r^* = r/\sigma_{mono}$. Gazzillo and coworkers proposed the following scaling: $\lambda_{\alpha\beta} = \langle\sigma^2\rangle^{1/2}/\sigma_{\alpha\beta}$ and $\sigma_{mono} = \sqrt{\left\langle\sigma^2_{\alpha\beta}\right\rangle}$ leading to $g_{\alpha\beta}(r) \simeq g_{mono}(r\langle\sigma^2\rangle^{1/2}/\sigma_{\alpha\beta})$. The choice of this scaling ensures that g_{mono} has to be evaluated at the same coverage $\eta = n_S\left\langle\sigma^2_{\alpha\beta}\right\rangle = n_S\sigma^2_{mono}$ of the whole mixture. At variance to DA or LMA, SA takes better into account the excluded volume effect although SA incorrectly assumes that pair correlation functions have the same value at contact $g_{\alpha\beta}(\sigma_{\alpha\beta}) \simeq g_{mono}(\sigma_{mono})$. In terms of the involved partial interference function, SA reads:

$$S_{\alpha\beta}(q_{\|}) = 1 + \langle\sigma^2\rangle^{1/2}/\sigma_{\alpha\beta}\left[S_{mono}\left(q_{\|}\sigma_{\alpha\beta}/\langle\sigma^2\rangle^{1/2}\right) - 1\right]. \tag{4.25}$$

SA[114,143] was compared in 3D systems to either the analytical solution of Vrij for polydisperse hard spheres[109,110] or to molecular dynamics simulations considering a Lennard-Jones interaction potential. The accuracy of SA is surprisingly

good whatever the packing or the degree of polydispersity. The shape as well as the height of the correlation peak is very well reproduced. The only discrepancy comes from the low q behavior of the total interference function. SA is unable to reproduce the exact fluctuations of the particle density[77] but, in the total cross section, this drawback is balanced by the product with the particle form factor. One of the drawback of SA scattering cross section is that, instead of DA, LMA or SSCA, it involves a double sum over the size-shape distribution. Even though very appealing in terms of accuracy, to our knowledge, SA was never applied to actual data analysis.

D. The graded interface model and the nanoparticle form factor

Up to now, the nanoparticles have been treated as independent or isolated perturbations of the wavefields obtained on flat interfaces. The linearity of the wave propagation equation allows to decouple the parallel and perpendicular directions and to introduce the notion of parallel interference function. However, increasing the particle packing leads to an enhanced absorption and refraction of both the incident and the scattered beams inside the particle layer itself. This is all the more true than the angles α_i, α_f are close to the critical angle and the beam paths in the particle layer is large. More accurate results are expected if the reference medium is taken as the graded interface that includes the particles themselves.
This method, developped by Lazzari[21,135], has been applied to the case of nanostructures randomly distributed on a surface. The reference medium is defined through the average dielectric index perpendicular to the surface. The perturbation to the refraction index is brought by the particles as well as by the vacuum holes in between. The effect of a large density of particles can be dramatic as shown in Fig. 18 for monodispersed supported full spheres (in which case the shape of the profile of dielectric index is parabolic). The zero-coverage case corresponds to isolated particles.

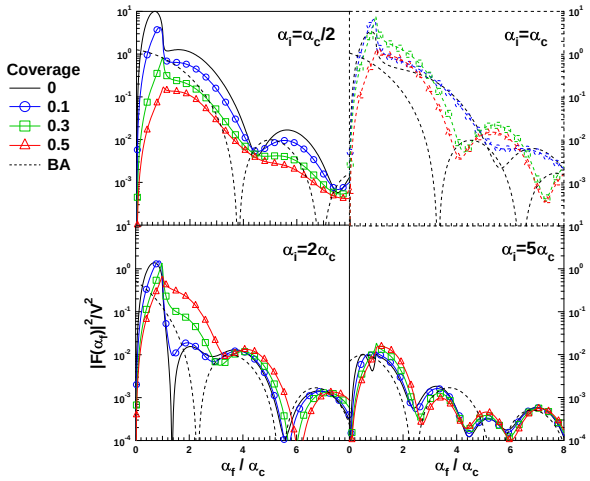

FIG. 18: Form factor $\mathcal{F}(\mathbf{q}_{\|} = 0, k_{i\,z}, k_{f\,z})$ of a full sphere of Au on $TiO_2(110)$ calculated in the framework of the graded interface as function of the particle coverage η and the incident angle α_i. The case of a dilute system Eq. 4.7 corresponds to a null coverage $\eta = 0$. The chosen dielectric contrast is strong enough to see the influence of the refraction index profile. From Ref.[21].

Fig. 18 demonstrates that the diffuse scattering is highly dependent on the coverage even for monodispersed particles in particular for angles close to and below the critical angle. Both the Yoneda peak shape and the location of the interference fringes are modified because of the propagation and attenuation of the waves inside the layer of particles. The discrepancies between the two models, namely DWBA on the flat substrate and graded interface appear on the experimental results of Fig. 19. The cut of intensity from Au islands grown on $TiO_2(110)$ have been fitted with the graded interface model using a truncated sphere shape. The obtained morphology allowed to deduce the profile of refraction index (inset of Fig. 19) and to simulate the expected curve accounting only for the substrate. The Yoneda peak intensity is overestimated as the damping of the evanescent wave below the critical angle of the layer itself is forgotten. The same behavior is observed at higher angle because of the Croce-Névot factor.

E. Deducing nanostructure size and shape from a rapid data analysis

Lazzari[24,51] has written a complete program called `IsGISAXS` to perform full quantitative analyses of 2D (or even composite 3D) GISAXS data. However, such analyses are complex and lengthy. It is thus important to obtain as much information as possible on the average nanoparticle shape, size and separation by simpler analyses of the data, *e.g.* following some of the the ideas presented below.

1. *The small polydispersity case*

In the case of small polydispersity, *i.e.* when all nanostructures are close in size and shape, the position of the zeros of the form factor are indicative of the morphological parameters. This is illustrated in Fig. 20 which represents the square modulus of the form factor as a function of $q_y \langle R \rangle_h$, where $\langle R \rangle_h$ is the average of the half parallel characteristic size R of the nanostructures over the coordinate h perpendicular to the interface. For isotropic nanostructures like cylinder and sphere based shapes, all the $|F(q_y \langle R \rangle_h)|^2$ functions are expressed with a Bessel function in the parallel plane and thus have their first zeros at $q_y \langle R \rangle_h \simeq 3.9$, as shown in Fig. 20-a. For a pyramid based shape, for the beam aligned along a face, all the $|F(q_y \langle R \rangle_h)|^2$ functions are expressed with a linear combination of $\sin(x)/x$ functions and thus have their first zeros at $q_y \langle R \rangle_h \simeq 3.3$, as shown in Fig. 20-b. For cylinder, sphere, and pyramid with the beam aligned along a face, the $|F(q_y \langle R \rangle_h)|^2$ function presents several well pronounced lobes. For the beam along an edge, the first zero or minimum is at $q_y \langle R \rangle_h \simeq 4.5$ for a heavily truncated pyramid (typically, $H/R \leq 0.5$) as shown in Fig. 20-c. This value corresponds to the previous zero value (beam aligned along a face) times $\sqrt{2}$. On the contrary, the $|F(q_y \langle R \rangle_h)|^2$ function decreases in a monotonous way for a complete ($H/R = 1.4$) or slightly truncated pyramid (typically, $H/R \geq 0.9$).

2. *The large polydispersity case: nanostructure size distribution*

Nanostructure shape and size distribution is a natural consequence of the growth-coalescence process. The exact size distribution law is a central information in numerous theoretical approaches of crystal growth. Nevertheless, depending on the growth stage (nucleation, growth or coalescence), the type of nucleation process (homogeneous or heterogeneous), the growth kinetics parameters (trapping energy, diffusion coefficient), the type of lattice mismatch relaxation, etc ..., it is difficult, if not impossible to predict it. Usually, the observed lateral size distribution is well described by a lognormal probability distribution, which is asymmetric (Fig. 21). The obvious effect of the size distribution (see Fig. 21) is to smooth the scattering curve. Poorly known also is the height distribution and the cross correlation between lateral size and height distributions. On a practical point of view, they are either fitted independently or are supposed to be fully or partially correlated[135]. Fitting procedures used in SAXS[144] could be also applied to GISAXS to deduce the size distribution from the lineshape of the scattering but we are unaware of any GISAXS data analysis based on this approach, maybe because of limited counting dynamics.

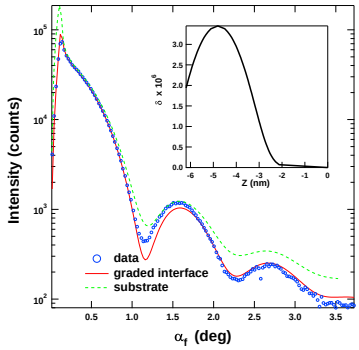

FIG. 19: Experimental cut of intensity from GISAXS of Au nanoparticles on TiO_2(110). The full line corresponds to the fit assuming size distributed truncated spheres and using the graded interface model (see Ref.[21] for further details). The dotted line is the calculated scattered intensity starting from the substrate only *i.e.* by assuming isolated particles. The profile of index of refraction $n = 1 - \delta - i\beta$ is displayed in the inset.

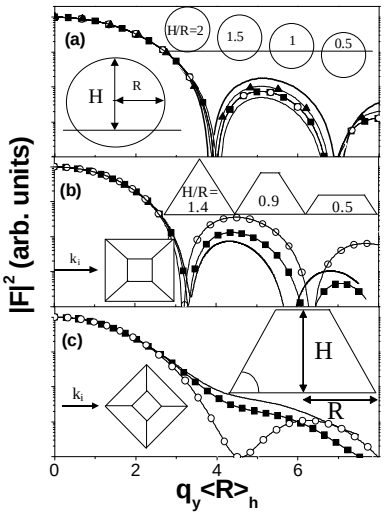

FIG. 20: Square modulus of the form factor calculated within the BA at $q_x = q_z = 0$ versus $q_y \langle R \rangle_h$. $\langle R \rangle_h$ is the average of the parallel nanostructure characteristic half size R over the coordinate h perpendicular to the surface/interface. a) Isotropic nanostructures. Bold line: cylinder; filled triangles: sphere with $H/R = 1.5$; open circles: $H/R = 2$; filled squares: $H/R = 1$; line: $H/R = 0.5$. b) Pyramid with the beam aligned along a face. Line: $H/R = 1.4$; filled squares: $H/R = 0.9$; open circles: $H/R = 0.5$. c) Same as b) but with the beam aligned along an edge. From Ref.[18].

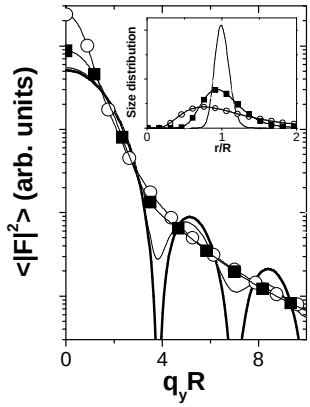

FIG. 21: The $\left\langle |F(q_y R)|^2 \right\rangle$ function calculated within the BA for a cylinder at $q_x = q_z = 0$. Bold line: without any size distribution; thin line: with a lognormal distribution $\sigma = 1.1$; filled squares: $\sigma = 1.3$; open circles: $\sigma = 1.7$. The inset shows the corresponding lateral size distributions. From Ref.[18].

3. The large polydispersity case: asymptotic behavior of the form factor

In size distributed samples, further insight may be gained by studying the asymptotic (or close to) behavior of the mean form factor, limit which is currently named the Porod approach in the field of small angle scattering on bulk samples. Whatever the approximation is, for disordered systems, the intensity at large $\mathbf{q}$ vectors is proportional to the average of the square modulus of the form factor. The curves $\log\left(\left\langle |F|^2 \right\rangle\right)$ versus $\log(q_y)$ or $\log(q_z)$ shown in Fig. 22 for simple geometrical shapes demonstrate that, for sufficiently distributed sizes, the intensity varies as q^{-n} with an exponent n that depends on the sharpness of the nanostructure shape. For instance, $n = 3$ for a cylinder, 4 for a hemisphere or a pyramid in the parallel direction, whereas $n = 2.5$ for a cylinder, 3 for a hemisphere or a pyramid in the perpendicular direction in a range where $\log(q_y R)$ or $\log(q_z H)$ are comprised between 0.5 and 1 (note that this is not streacly speaking the asymptotic behaviour, but an intermediate range). Hence, providing that measurements are performed sufficiently far away in the reciprocal space (typically $q_y R$ or $q_z H > 3.5$) over a wide dynamic range, each considered nanostructure shape is fully characterized by a set of slopes in both directions. It is

also worth noticing that the difference with the 3D-case where $n = 4$ for continuously curved interfaces is due to the reduced dimensionality and the absence of the orientation average as supposed in the 3D-Porod limit.

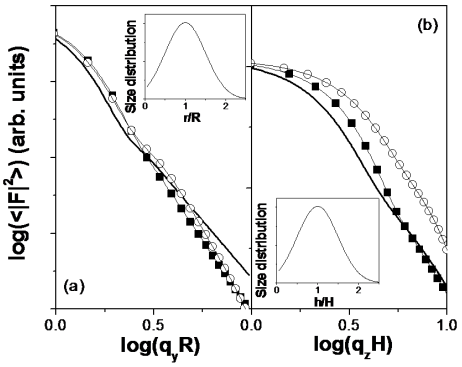

FIG. 22: Plots of $\log(\langle|F|^2\rangle)$ calculated within the BA a) at the q_z position of total external reflection versus $\log(q_y R)$, and b) at the q_y position of the interference maximum versus $\log(q_z H)$. Continuous line: cylinder $H/R = 1$; filled squares: hemisphere; open circles: pyramid $H/R = 0.9$, and $\zeta = 0°$. The insets of a) and b) show, respectively, the lateral and vertical lognormal size distributions of $\sigma = 1.7$. Similar results are obtained within the DWBA. From Ref.[18].

F. Summary on GISAXS data analysis

The quantitative analysis of GISAXS patterns starts by the acquisition of good data with the widest dynamical range. This obvious prerequisite includes background minimization[17] or subtraction (a promising procedure being the use of anomalous scattering[145]), detector correction and normalization, account for the resolution function (beam divergence, wavelength spread, detector acceptance, sample curvature and homogeneity) and measurements far away in reciprocal space to be sensitive to the particle form factor only. Extracting precise morphological parameters such as average lateral size, height and separation distance needs the use of an appropriate model, that accounts for the exact shape of the islands, the distribution of sizes, an appropriate island-island pair correlation function, as well as refraction effects when the incident or exit angles are close to the critical angle for total external reflection. The method to perform an extensive, quantitative analysis of GISAXS patterns is described in details in several papers[18,24,58]. The `IsGISAXS` software[24,51] written by Rémi Lazzari allows such a quantitative analysis through a simultaneously fitting of several cuts of the 2D GISAXS data, performed in any direction before simulating the complete 2D picture. In general, the fitting procedure starts with one cut parallel to the surface at the q_z position of maximum intensity, and another one perpendicular to it at the q_y position of the interference maximum. The analysis of GISAXS data relies on direct modeling using non linear χ^2 minimization[146] for fits (Levenberg-Marquadt χ^2-minimization). One has to be aware of all the pitfalls of such a procedure in terms of global minimum finding, accuracy and reliability[144]. As a rule of thumb, for a random distribution of nanoparticles, accurate measurements can be obtained for the mean values (in-plane and out-of-plane size, distance between particles) while larger error bars are obtained for the width (and therefore the shape) of the size distribution or the fluctuations of distances. The systematic error introduced by the used approximation to treat partial correlation (DA, LMA, SSCA, SA) should be balanced by a careful fit of the high q range even at the expense of the correlation peak.

V. *IN SITU* GISAXS MEASUREMENTS IN ULTRA-HIGH VACUUM, DURING GROWTH

A. 3D-island growth: the metal/oxide interfaces case

1. *Motivations*

The oxides and their interplay with metals are of central importance in environmental and earth science as well as in technological applications[147,148] such as catalysts, gas sensors, optical, electronic and magnetic devices[149]. Vapor-deposited metals grow generally on oxide surfaces in the form of three-dimensional (3D) nanometer-sized clusters rather than in a monolayer-by-monolayer mode[13,29]. A variety of related parameters are involved in the growth process (the surface free energies of the two materials, the interface energy, their respective electronic and crystalline

structures, the lattice parameters, kinetic factors) which condition the shape and the size of the metallic nanoclusters. The cluster morphology and their statistical organization on the substrate determine in turn the physical and reactive properties of the overall system[150–152]. Many other questions have to be addressed to characterize the growth, among which, the type of nucleation, homogeneous or heterogeneous, the type of coalescence, static or dynamic, the adhesion energy between the metal and the oxide substrate, the diffusion energy of metal on the oxide surface, the equilibrium shape of the islands, the spread of the island size and shape, the possible existence of correlations between the sizes and separation of neighboring islands, most of these properties depending on growth temperature and thickness. In a mass non conserved system *i.e.* upon arrival of new material on the surface, two main coalescence mechanisms are often invoked:[35,112] static or dynamic. In static coalescence, neighboring growing islands merge when they touch, leading to a new island occupying the center of mass of the two primary islands. In all theoretical studies, the coalescence times and the reshaping time are supposed to be very small compared to the (inverse) flux of incoming atoms so that the islands are supposed to keep always the same shape. By contrast, dynamic coalescence involves the diffusion of islands (in the form of clusters of adatoms or small particles) on the surface. Deltour *et al.*[153] showed that the island diffusion can be significant for non-epitaxial or non-coherent, small enough islands (typically less than 1000 atoms/island). Despite these numerous studies, very few experimental works are available regarding the type of nucleation, the diffusion energy, the coalescence mechanisms or the adhesion energy between metal and oxide surfaces. It is thus fundamental to characterize the morphology during the growth. For all these metal/oxide systems, many electron or tunneling-based tools available to characterize the morphology are hampered by the insulating character of the insulating substrate. *In situ* GISAXS is thus very useful to overcome these limitations. In addition, if many studies of the early stages of nucleation and growth exist, none or only few deal with the growth and coalescence regimes, which is the object of the GISAXS studies summarized below.

2. Investigated systems

In this section, we discuss the different growth of metals on oxide surfaces that were investigated *in situ* by GISAXS: growth of Ag[23,140,154], Pd[18,99], Pt [20] and Fe[66] on MgO(001); Co/NiO(111) [155]; Au/TiO_2(110) [135]; Ag/ZnO(0001)[94,156].

a. Metal/MgO(001) The non-reactive Ag/, Pd/ and Pt/MgO(001) systems are test beds for the fundamental issues regarding the contact between dissimilar materials[13,29,151,157,158] because they offer favorable conditions for both experimental and theoretical investigations. Moreover, these systems have been thoroughly investigated as model catalysts[29,151]. The structural and epitaxial properties of these interfaces have been investigated in depth both experimentally (Ag/MgO[9,159,160], Pd/MgO[15], Pt/MgO[20] and Ni/MgO[161]) and theoretically[162–164], however, much remained to be done regarding the exact growth modes.

b. Ag/ZnO(0001) Zinc oxide exhibits physical (direct band gap in the UV region, high exciton binding energy, ...) and chemical (mixing of covalent-ionic characters, high solubility of group III donor impurities or transition metal atoms) properties[165] which give it considerable potential in many fields. Concerning metal-oxide interfaces, ZnO is already employed on industrial scale as a support of copper for methanol synthesis and water-gas shift reaction[166] and the use of ZnO as a support of silver for low-emissive and anti-solar coatings on glazing[167,168], the metal film acting as a mirror in the infrared wavelength range. A central concern in manufacturing the coatings is the way the silver film wets the oxide support. The peculiarity of the growth of noble and late transition metals on the basal planes of zinc oxide, namely the (0001) Zn-terminated and the $(000\overline{1})$ O-terminated surfaces, is its enhanced two-dimensional character. The critical coverage, defined as the fraction of the surface covered by the metal at the onset of the formation of the second layer, has been estimated equal to 1 for platinum[169–171] and equal to 0.55[151] (0.35[172]) for copper on O (Zn) face. Copper has been shown to form flat-top clusters[151,173] and a pseudo layer-by-layer growth is inferred,tentatively explained considering either electronic transfer from metal to surface states[174] or purely kinetic mechanisms[151].

c. Au/TiO_2(110) Recently, catalysts made of gold nanoparticles[175] have attracted the interest of numerous scientists because of their potential applications to many reactions of industrial and environmental importance. Nanoscale gold particles are extraordinary active for the oxidation of CO at room temperature. The titania support is the warhorse of numerous fundamental studies aimed at understanding the catalytic mechanisms and at elucidating the origin of this surprising reactivity as neither titania nor bulk gold alone are active. Because the cluster morphology seems a key parameter in the understanding of the catalytic activity of gold[176], many studies were performed by using vacuum techniques on planar TiO_2(110) substrate (see reviews Ref.[177,178]). The growth of gold on titania was characterized by microscopy techniques (STM[150,179–188], HRSEM and HRTEM[189,190]) and Low Energy Ion Scattering[152,172,191]. At low coverage (0.1 ML), the gold clusters grow as quasi-2D particles of one or two atomic layers high, with diameters between 1-2 nm, which appear to be the most catalytically active[150]. For higher coverages (> 0.2 ML), they are rapidly mixed with hemispherical 3D particles with a diameter in the range 2.5-4 nm. The biggest particles

(diameter larger than 4 nm) have a higher contact angle ($\theta_c \simeq 122°$).

d. Co/NiO(111) The Co/NiO(111) interface was investigated[155] because it involves a ferromagnetic medium on an antiferromagnetic. It is then involved in the fabrication of spin valves sensors, used as magnetic read heads in computer hard drives, position sensors, and magnetic random access memory elements. The interfacial magnetic characteristics and behaviors are often explained by speculations on the interface properties such as roughness, diffusion, etc. A detailed *in situ* study of the structure and morphology evolution during growth was then thought to be mandatory.

3. Examples of extensive data analysis of GISAXS patterns from metal/oxide systems

All measurements reported hereafter were performed in UHV. The experimental GISAXS data look similar in all the cases encountered. In all cases, qualitatively, the experimental GISAXS patterns (see for instance Fig. 23) present two wide intensity lobes visible along the parallel direction, separated by the specular rod, which is partly hidden by the beamstop. They arise because the islands are not completely distributed at random, but are separated by a preferential nearest neighbor (center-to-center) distance D. As a consequence, for a given value of q_y, there are constructive interferences between the waves scattered by neighboring island. The absence of intensity minima parallel to the surface reveals a wide distribution of lateral sizes. The separation between the two main lobes is inversely proportional to the average separation between neighboring islands. The extent of the intensity parallel (resp. perpendicular) to the surface is inversely proportional to the average lateral size (resp. height) of the island.

a. First example: Pt/MgO(001) The first example concerns the growth of Pt/MgO(001)[20](Fig. 23). The analysis

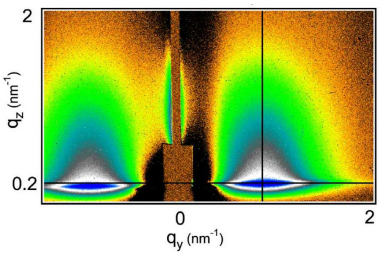

FIG. 23: A typical experimental GISAXS pattern of Pt deposited on MgO(001), with two scattering lobes in the (q_y, q_z) plane. The two characteristic line cuts used in the fit procedure are shown as bold line. From Ref.[20].

used the DWBA[58] and LMA[116,117] formalisms. The one-dimensional paracrystal[79] with Gaussian statistic was chosen as the theoretical model to account for the interference between scatterers. The size distributions parallel and perpendicular to the substrate were modeled by coupled or uncoupled log-normal or Gaussian laws. Two cross sections (Fig. 24) along q_y and q_z at the maximum of scattered intensity *i.e.* at the positions of the correlation and Yoneda's peaks, respectively, are first simultaneously fitted. To improve statistics, additional profiles collected farther away in the reciprocal space were also fitted. Different island shapes of increasing complexity were considered to analyze the data. Scattering patterns from Pt/MgO(001) films deposited at 600 K, 800 K and 1000 K were analyzed at several thicknesses. Films grown at 600 K (Fig. 24) and 800 K were simply fitted by means of truncated sphere shapes. Indeed, the GISAXS intensity maps did not show any anisotropy upon rotating the sample, nor any scattering rod characteristic of oriented facets, and the behavior of the intensity at high wavevector transfer[18] ("Porod's regime") was characteristic of such a shape. The quality of the model was judged by the way it reproduced the intensity profiles (Fig. 24-c,-d) and the 2D-GISAXS pattern (Fig. 24-b). However, models based on cylindrical and spherical particle shapes failed in the case of films deposited at 1000 K. Good fits were instead obtained only by representing clusters by a truncated pyramid with a square-basis. The fitted angle of the side facets corresponds to islands that display (111) planes in cube-on-cube $(001)_{\mathrm{MgO}} \parallel (001)_{\mathrm{Pt}}$ epitaxy. Consistently, diffuse scattering rods[16] inclined by 54.7° were observed on some GISAXS images.

b. Second example: Pd/MgO(001) The second example concerns the growth of Pd/MgO(001) at different temperatures[16,18] (550, 650 and 740 K), and for different thicknesses (0.1, 0.9, 1, and 3 nm). The general GISAXS formalism[24,25] has been used, within the DWBA and the LMA. For a 0.1 nm thick Pd/MgO(001) deposit at 650 K, the mean island shape used to fit the GISAXS, a truncated pyramid with a square base was deduced from microscopy works for similar temperature and island size conditions[192]. A very good agreement was obtained between simulated and experimental data, with only a very small size distribution. For a 1 nm thick Pd/MgO(001) deposit at 650 K, Fig. 25 displays the 2D GISAXS experimental patterns and the corresponding analysis with the incident beam along

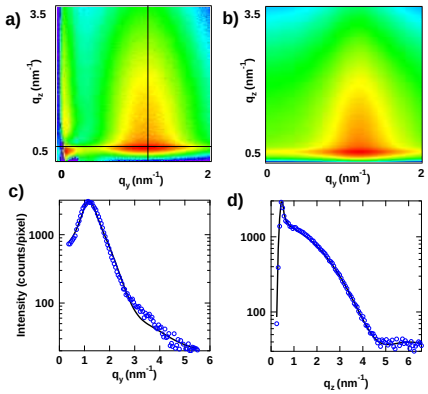

FIG. 24: 2D GISAXS patterns for a 0.3 nm thick Pt deposit on MgO(001) at 600 K. a) Experimental 2D pattern and b) GISAXS pattern simulated with the parameters obtained from the fits made along the c) parallel and d) perpendicular linear cuts through the intensity maximum (shown in a-map). In c) and d), the continuous lines correspond to the best fits and the dots to data points. Images are plotted on a logarithmic color scale. From Ref.[20].

the MgO[110] (resp. MgO[100]) direction). The 2D GISAXS patterns present a scattering rod at 54.7° with respect to

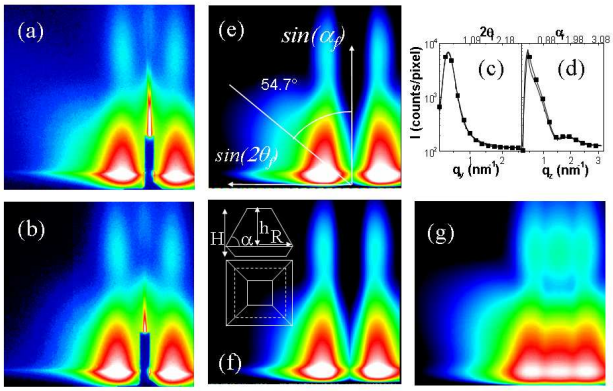

FIG. 25: 2D GISAXS intensity for a 1.0 nm thick Pd/MgO(001) deposit at 650 K: a) Experimental patterns with the incident beam along the MgO[110] direction and b) same as a) but with the incident beam along the MgO[100] direction. Black lines show the positions of the two cuts used to fit the data, parallel and perpendicular to the surface. For sake of clarity, are only shown c) parallel and d) perpendicular cuts for the 2D GISAXS pattern taken with the beam along the island edge b). Continuous line: experimental cuts; filled squares: best fit of experimental cut. e) and f) Simulated 2D GISAXS patterns of a) and b) respectively obtained after fitting the above experimental cuts and using an island shape of a truncated octahedron with a square base schematically drawn. g) Same as e) but within DA. The intensity is represented with a logarithmic scale, the 2θ (resp. α_f) axis ranges from 0 to 2.9° (resp. 3.3°). From Ref.[18].

the surface normal in the ⟨110⟩ direction but not in the ⟨100⟩ direction. This indicates that palladium forms oriented faceted islands with {100} and {111} facets on the MgO(001) surface. Moreover, in case of faceted islands, the second and even sometimes third order scattering peaks perpendicular to the surface are indicative of flat (001) terraces and of narrow height distribution. All these features point to a truncated octahedron-like average shape as also seen from TEM plane views. The simulated GISAXS patterns well reproduce the general features of the experimental ones, especially the scattering rod along the (111) direction visible in Fig. 25-a. As an example, one experimental GISAXS map (that with a scattering rod at 54.7° with respect to the surface normal in the ⟨110⟩ direction) has been simulated within the DA (cf. Fig. 25-g). Notice that neither the DWBA-LMA, nor the DWBA-DA correctly reproduces the experimental diffuse scattering close to the beam stop, which will be discussed later.

4. General trends during growth and coalescence of islands

a. Introduction For most metal/oxide systems studied, and whatever the growth temperature, the 2D GISAXS patterns and their evolution during growth look qualitatively similar: they are characteristic of the Volmer-Weber three dimensional growth mode expected from the poorly adhesive noble metal-oxide systems[151]. We thus illustrate the *in situ* GISAXS measurements during growth on only two systems: Ag/MgO(001) for two deposition temperatures (Fig.26): 300 K and 540 K, and Au/TiO_2(110) at 300 K (Fig. 28). Measurements were always performed with the incident X-ray beam oriented along at least the [100] and [110] directions of the MgO(001) substrate and several in plane directions of the TiO_2(110). When growth proceeds, the two scattering maxima along the parallel direction

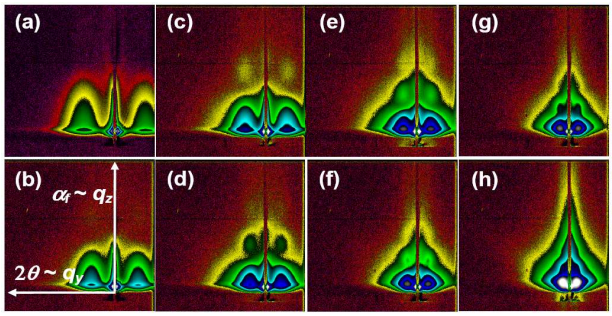

FIG. 26: Evolution of the 2D GISAXS patterns during the *in situ* growth of Ag on a MgO(001) surface at 300 K (ID32 setup), with the incident beam along the MgO[100] direction, for different equivalent deposited thicknesses: a) 1 nm, b) 1.8 nm, c) 2.2 nm, d) 3.6 nm, e) 4.4 nm, f) 6.2 nm, g) 7 nm, and h) 10 nm. The intensity is represented on a logarithmic scale. Each black contour between two colors corresponds to an order of magnitude change in intensity. The q_y (respectively q_z) axis ranges from 0 to 2.5 nm^{-1} (respectively 2.6 nm^{-1}). From Ref.[99].

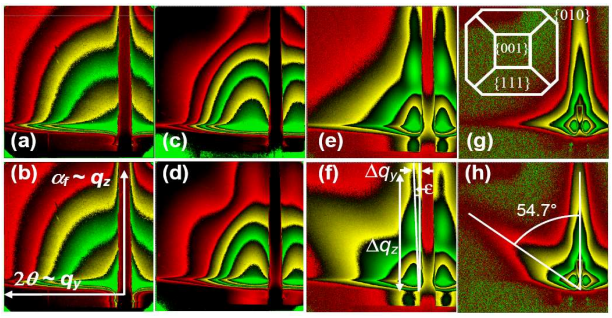

FIG. 27: Evolution of GISAXS patterns during the *in situ* growth of Ag on a MgO(001) surface at 540 K with the incident beam along the [100] direction of the MgO(001) substrate for a), c), e), g) and with the incident beam along the [110] direction for b), d), f), h). Several equivalent thicknesses are reported : a) and b) 0.1 nm, c) and d) 0.3 nm, e) and f) 2 nm, g) and h) 7 nm. The intensity is represented on a logarithmic scale. Each black contour between two colors corresponds to an order of magnitude change in intensity. The q_y (respectively q_z) axis ranges from 0 to 2.7 nm^{-1} (respectively 3 nm^{-1}). Inset: top view of the truncated cubo-octahedron island shape with the {001}, {111}, and {010} facets. From Ref.[99].

move toward the origin and become more intense as the metal deposit increases. This reveals an increase of the average inter-island distance D, which can only be explained by the coalescence of neighboring islands. In addition, the overall diffuse scattering becomes more and more concentrated toward the origin of the reciprocal space, revealing the increasing island sizes. The observed evolution is thus characteristic of a growth and coalescence mechanism.

b. Ag/MgO(001) In the Ag/MgO(001) case (Fig. 26 and 27), for large enough thicknesses, a second and even a third order maxima along the perpendicular direction are observed (*e.g.* at Ag thicknesses of 2.2 nm and 3.6 nm for the 300 K growth), meaning that the height of the islands is well defined, with a small distribution. Note that the second order maxima are at a smaller q_z coordinate than the specular one. As a matter of fact, the separation in q_z of the off specular peaks is inversely proportional to the average height of the islands, while that of the specular peaks is inversely proportional to the average film thickness. Hence, this q_z coordinate difference is linked to the metal morphology. Finally, in the case of Ag, this third and then second order maxima along the perpendicular

direction disappear and the GISAXS pattern looks like an apex (at a Ag thickness of 10 nm), meaning that the islands become flatter. This corresponds to the percolation regime, in which neighboring islands become connected and evolve toward very large, flat islands, exposing a top (001) surface and side {111} facets[193].

c. Room temperature growth of Au/TiO$_2$(110) In this case[135], upon increasing coverage (Fig. 28), (i) interference fringes appear in the perpendicular direction (0.6 nm) up to show three bounces and (ii) the Yoneda's peak becomes round and shifts from the critical angle α_c of TiO_2 (0.1311°) to a value close to α_c of gold (0.2528°) (inset of Fig.28). Shift and rounding cannot be accounted for by the standard DWBA which refraction effect only comes

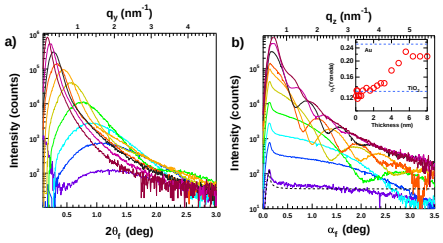

FIG. 28: Intensity cross sections of the GISAXS patterns measured during the growth of Au on TiO_2(110). The cuts are made a) along the 2θ direction at the location of the Yoneda's peak and b) along α_f at the location of the correlation peak. The intensities have been rescaled accordingly to the counting time. The equivalent thicknesses are (from bottom to top) 0.05, 0.15, 0.3, 0.6, 1.2, 2.0, 2.8, 4.0, 5.6 and 8.0 nm. The inset shows a plot of the Yoneda's peak location as function of deposited thickness while the dotted curve in Fig. b corresponds to the transmission function of TiO_2. From Ref.[135].

from the substrate[21]. In the parallel direction, the in-plane correlation peaks are clearly separated from the specular rod. As previously suggested[18], the analysis of such a profile is not tractable within the Decoupling Approximation[77,79,100,101,115] as neglecting all correlations leads to a too intense incoherent diffuse scattering for size distributed island collections. The Local Monodisperse Approximation (LMA)[114,116,121,194] would better fit the result, but it assumes scattering by independent monodisperse domains, an unphysical hypothesis in the present context. In an attempt to overcome these difficulties, the analysis of the data has been performed through two new approximations developed by Lazzari *et al.*[21], the DWBA on the graded interface (see Sect. IV D) and the SSCA model (see Sect. IV C 6). Note that for the RT growth of Au/TiO_2(110), GISAXS patterns were nearly independent from azimuthal rotation[135]. Thus, the analysis was limited to data collected with the X-ray beam aligned along the $[1\bar{1}0]_{TiO_2}$ direction.
As explained in Ref.[18], the sensitivity to the particle shape is found in the high-q wave vector transfer range. The Porod's plot of the 8 nm film (Fig. 29) demonstrates a power law behavior in the high-q range $I(q_{\parallel}) \sim q_{\parallel}^n$ and $I(q_{\perp}) \sim q_{\perp}^m$. If considering only shapes with z-revolution axis, the found exponents $n = 4.02$ and $m = 3.63$ are

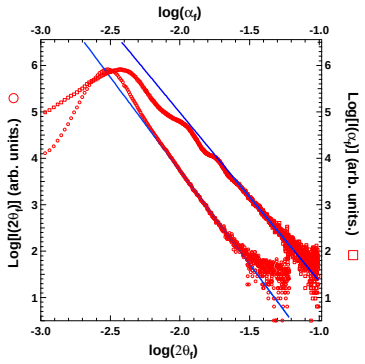

FIG. 29: Growth of Au/TiO_2(110): Log-Log plot of the cross sections for the 8 nm deposit with a power law fit of the high q-range. From Ref.[135].

consistent with a truncated sphere profile ($n = 4, m = 2$ for a hemisphere; $n = 4, m = 4$ for a sphere; $n = 3, m = 2$ for a cylinder[18]). Analyses were consistently performed with truncated spheres over the entire study. The radius

R and height H distribution have been taken as a joint-normal law with a correlation coefficient ρ between R and H. The data have been fitted with the `IsGISAXS` software[24,51] using a χ^2 criterion, with error bars proportional to the square-root of the intensity, as checked from the fluctuations of data points along each cross section. At each coverage, two cross sections (averaged over a window of five pixels to keep the resolution on the Yoneda's peak) were fitted, (i) along $\alpha_f \sim q_z$ at the correlation peak and (ii) along $2\theta_f \sim q_y$ at an exit angle α_f equal to three times that of the Yoneda's peak ($\alpha_f = 3\alpha_c$). To avoid distortions in fitting the sharp Yoneda's peak, the fit was only performed on data points $\alpha_f > 3\alpha_c$. The total χ^2 and the total reliance factor R_B[24] laid always below 4 and 0.12, respectively, at any coverage. The shape of the correlation peak, the decrease in intensity near the specular rod and the high-$q_{\|}$

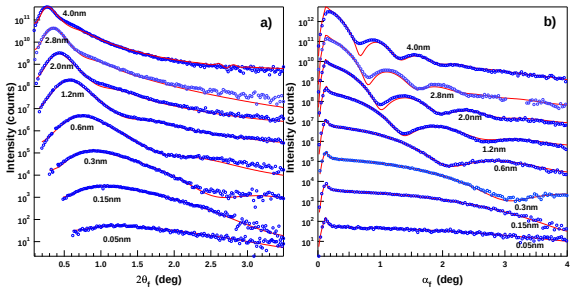

FIG. 30: Au/TiO_2(110): Fits (continuous line) of the GISAXS intensity cross sections (circles) all along the growth. The equivalent deposited thicknesses are given on the figure. Data have been modeled by scattering from size distributed truncated spheres within the SSCA and the DWBA on the graded interface. The curves have been shifted for clarity. From Ref.[135].

range were well reproduced. The agreement was also good in the perpendicular direction (Fig. 30-b), except perhaps fringes at the highest coverage. A likely explanation is the oversimplified description of the particle shape and size distribution. If fitted, the incident angle α_i was found close to that determined from sample-beam alignment. The good modeling of the Yoneda's peak (even though not explicitly included in the fit process !) gives confidence in the theoretical treatment of DWBA on the graded interface.

The experimental and simulated 2D GISAXS patterns for a 1.6 nm-thick deposit at room temperature are compared in Fig. 31. A good agreement between experimental and simulated image is achieved except near the specular rod. The simulated lobe displays a diffuse tail due to (i) the interplay between the size-spacing coupling and (ii) the strong correlation between the island radius and height[135]. The discrepancy with the experimental image could result an effect of shadowing by the beam stop.

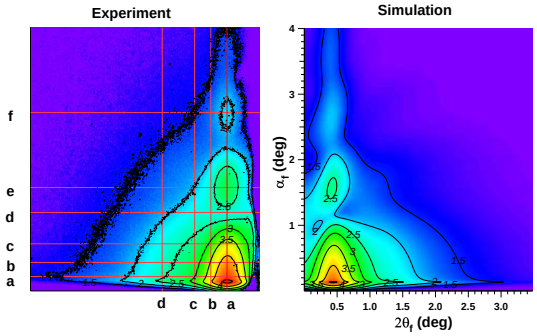

FIG. 31: Experimental (left) and simulated (right) GISAXS patterns of a 1.6 nm thick RT Au deposit on TiO_2(110). The color scale is logarithmic as given by the contour lines. From Ref.[135].

The above examples, for which the experimental 2D GISAXS maps are very well reproduced by the simulations, demonstrate on many different cases that the theoretical treatment presented above is well adapted to analyse 2D GISAXS data, at least when the islands are not ordered. The cases of ordered island repartition on the substrate will be treated in Sect. V C.

5. Evolution of morphological parameters with thickness: nucleation, growth and coalescence

For all the metal/oxide growth studies mentionned above, the average morphological parameters, lateral size (d or half-size R), separation (D) and height (h or H), were deduced for different growth temperatures as a function of deposited thickness. These evolutions were first used to identify the successive steps of the growth process: nucleation of islands, followed by growth and then coalescence. A decrease of the average separation D (hence an increase of the average island density , $\rho \sim 1/D^2$, is a signature of the nucleation stage. A steady separation D corresponds to growth at constant density, while and increase of D (a decrease of ρ) indicates coalescence. The value of ρ at the beginning of the growth may provide information on the nucleation process: heterogeneous (on defects) or homogeneous. Possible power-law behaviour of the morphological parameters may provide useful information on the detailed growth or coalescence processes. A constant aspect ratio H/D indicates that the shape is likely well defined, and thus probably the equilibrium one. By applying the Wulff-Kaischew or Young-Dupré constructions[195,196], this allows deducing the adhesion energy. In addition, a comparison between the thickness deduced from the quantitative GISAXS analysis and the actual deposited thickness (as calibrated either *in situ* during the experiment by *e.g.* x-ray reflectivity or by use of a quartz microbalance, or *ex situ*, on the last deposit by *e.g.* electron microscopy or Rutherfod Backscattering) allows determining the sticking coefficient and its evolution with deposit thickness. A few examples of such analyses are given below. Note that since the growth process is interrupted during GISAXS acquisitions, before comparing with theoretical models, it should be determined whether the film might evolve during the measurements upon coarsening. Such coarsening can fortunately be discarded for Au on TiO_2(110) at 300 K[152], as well as for Ag/MgO(001) and Pt/MgO(001) at all studied temperatures. As shown below, for these three cases, the growth exponents lead to very similar conclusions.

For instance,the growth of Pt/MgO(001) was investigated at three temperatures (600 K, 800 K and 1000 K). A comparison between the mean film thicknesses deduced from GISAXS and the calibrated ones shows that the sticking coefficient of Pt/MgO(001) is between 0.35 and 0.55 at the studied temperatures. At the smallest coverage of 0.3 nm, the inter island distance is around 2.5 nm at 600 and 800 K, which is characteristic of nucleation on defects because the corresponding density of particles is very high ($\rho \sim 1/D^2 = 1.6\,10^{13}$ cm^{-2}) and does not depend on temperature. For the same coverage at 1000 K, $D = 6$ nm is twice higher probably because of a temperature-enhanced detraping of atoms from defect sites and an increase of the critical nucleus size needed to avoid dissolution. The continuous increase of inter island distance D evidenced that coalescence occurs all along the deposition and that the nucleation-growth step happens before the start of the GISAXS measurements, *i.e.* before 0.25 nm thickness. Data points at all temperatures could be represented by power laws ($d \sim t^{0.5}$ and $D \sim t^{0.3}$) with evaporation time. The coalescence mechanism may involve the static meeting of particle growing at fixed position or a dynamic diffusion of clusters. If the reshaping of particles is faster than the time scale of impinging atoms, analytical models, scaling descriptions and numerical simulations[197–199] of static coalescence agree on a $d \sim t^1$ power law behavior. Power laws relative to the spacing between clusters are more scattered: $D \sim t^1$ (Ref.[197,198]), $D \sim t^{0.135}$ (Ref.[200,201]) for homogeneous nucleation and $D \sim t^{0.5}$ (Ref.[201]) for heterogeneous nucleation. The discrepancy with the actual measurement on the diameter d rules out the static mechanism. Instead, the actual $d \sim t^{0.5}$ and $D \sim t^{0.3}$ laws are close to that derived for dynamic coalescence in breath figures[202] in a case in which the diffusion of droplets leads to a bimodal size distribution where the biggest particles follow $d \sim t^{0.48}$ and $D \sim t^{0.25}$.

In the Pd/MgO(001) case, at the very beginning of growth, in the nucleation regime, the 0.1 nm thick Pd/MgO(001) deposit has small vertical and lateral size distributions, which are similar. Then, for a Pd deposit from a few 0.1 to several nm, a striking result is that the height distribution is smaller than the lateral size distribution whatever the temperature is from 550 to 740 K. This behavior, which seems to be independent of temperature and film thickness, is believed to originate from growth mechanisms. First, the denser (111) faces grow faster than the (001) facets. Second, while the (111) side facets grow from both vapor phase and atom diffusion, the (001) top facets grow mostly from the vapor phase as if they were isolated, because of the high energy barrier an atom has to overcome to jump from a (111) to a (001) facet[203,204].

The RT growth of Au on TiO_2(110) is discussed in more details. the average radius R, height h and distance between islands D are shown in Fig. 32. During the first stage of growth at constant particle density, *i.e.* (nucleation and growth regime), the power law $R \propto t^{0.31\pm0.1}$ corresponds to that expected ($R \propto t^{1/3}$) for particles growing by a diffusion limited mechanism (and not an attachment limited one) with a negligible direct impingement on the particle and a nearly full condensation[197,205]. A similar result comes from the analytical solution of the growth of a droplet by attachment of diffusing monomers with a constant flux at infinity[202]. The found exponent is closer to that expected from the rate equations of growth[139] for nucleation on defects ($R \propto t^{1/3}$) than a homogeneous nucleation behavior ($R \propto t^{2/9}$) in the case of complete condensation. Indeed, on one hand the sticking coefficient is found close to one and on the other hand, strong re-evaporation would lead to $R \propto t$. The corresponding density of particles

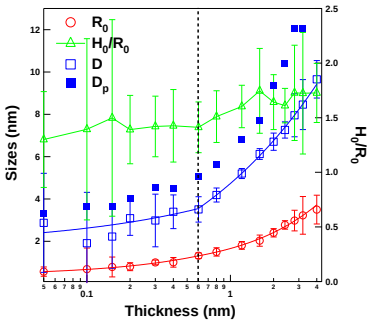

FIG. 32: Evolution of the $Au/TiO_2(110)$ morphological parameters as function of the deposited thickness a) Average radius R (red open circles), b) Average height over radius h/R (green open triangles), c) Average spacing between islands D (blue open square) and the value D_p (blue filled squares) as deduced from the location of the correlation peak $D_p = 2\pi/q_y^p$. The island shape was taken as a truncated sphere and the (R,H) size distribution has been chosen as joint-normal. The separation (vertical dotted line) between growth and coalescence is characterized by the power law fits of $R \propto t^{0.31\pm0.1}, t^{0.54\pm0.07}$ and $D \propto t^{0.15\pm0.2}, t^{0.51\pm0.05}$ (continuous lines). In passing, note that this corresponds to the onset of decrease of catalytic activity toward the oxidation of CO of Au clusters on $TiO_2(110)$[150]. From Ref. [135].

$1/D^2 \propto 10^{13}$ cm^{-2} is a typical concentration of defects (vacancies and step edges) on $TiO_2(110)$ surface obtained by ion bombardment and annealing procedure[177]. The regime observed at higher coverage likely corresponds again to dynamic coalescence. Theoretical works on dynamic coalescence of 3D particles on a 2D substrate are scarce[112]. For a mass conserved system, a logarithmic correction was found for the exponents of the power laws $R \propto [t/\ln(t)]^{1/3(1-\gamma)}$ and $D \propto [t/\ln(t)]^{1/2(1-\gamma)}$ within simulations in which the Brownian particle diffusion coefficient scales with the volume of the particles $D_F \propto R^{3\gamma}$ (Ref.[199]). Fitting the data leads to $\gamma_R = 0.63 \pm 0.18$ for the radius and $\gamma_D = 0.20 \pm 0.14$ for the distance, thus to an enhanced diffusion of the biggest particles.

In a similar way for the Ag/MgO(001) system, the hypothesis that the deposited thickness is proportional to an equivalent "deposition time" of a hypothetical growth without interruption is validated by the fact that, for all deposits and all temperatures, the GISAXS data were found steady during annealing. This arises because the diffusion energy of Ag on MgO(001) (0.05 eV, see below) and of Ag on Ag (less than 0.1 eV)[206] are very small. As a result, the islands and their distribution on the substrate reach their equilibrium state just after the deposit is made, in a time much shorter than the measurement time. In Fig. 33, two regimes can be distinguished, as a clear slope break appears on the inter-island distance for a deposited thickness of 2-3 nm. Below this value, at least at 300 and 540 K, the inter-island distance is nearly constant and the lateral size increases according to a power law $d \propto t^m$, with $m \simeq$0.32-0.35. This regime can be assigned to the nucleation and growth of islands at nearly constant density with an increase of surface coverage (Fig. 34). Again, the $m \simeq 1/3$ exponent on the lateral size power law corresponds to the growth of islands by capture of diffusing species in their surface of influence with a negligible direct impingement on the islands[197]. Above a 2-3 nm thickness, the inter-island distance increases according to a power law $D \propto t^{0.70-0.85}$ in the temperature range 300-640 K. The lateral size also increases according to a power law $d \propto t^{0.62-0.64}$. This regime can be assigned to coalescence with a nearly constant surface coverage (30-40% according to the temperature) (Fig. 33) below the jamming limit of 55% for the percolation and formation of interconnected structures[112,207]. A static coalescence process would yield a power law $d \propto t^1$ for the island lateral size, and can thus be ruled out as the dominant process[197–199]. The smaller exponant corresponds rather to dynamic coalescence. The logarithmic correction for the power law of the droplet diameter and distance given above in the Au/TiO_2 case are verified with $\gamma \simeq 0.8$. This positive value leads to a behavior of enhanced diffusion of the largest islands contrary to what is expected from standard models[208] of diffusion of the center of mass of the particle through periphery atom mobility. As a matter of fact, in this dynamic coalescence regime, the Ag islands are no longer in coherent registry on MgO(001), and display interfacial dislocations[160]. As a result, they may diffuse much more easily than coherent islands as shown by molecular dynamics simulations[153]. This behavior has been already observed for Au islands on amorphous Al_2O_3 combining TEM and Kinetic Monte Carlo Simulation,[209], as well as for small Pd islands on MgO(001)[210]. In summary, the three above examples show how the growth modes can be inferred from GISAXS measurements. Similar analyzes, not discussed here, were performed in the other metal/oxide growth studies.

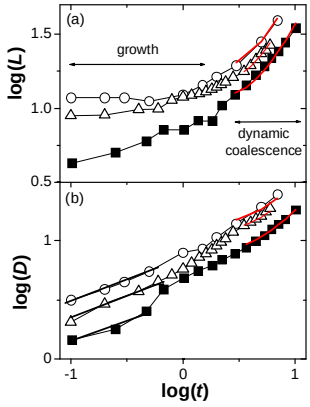

FIG. 33: Growth of Ag/MgO(001) analyzed by GISAXS. Double-logarithmic representation of a) the inter-island distance D and of b) the lateral size d obtained by GISAXS as a function of time, for different deposition temperatures. The parameter t is the Ag deposited thickness. Filled squares, T=300 K; open circles, T=540 K; up triangles, T=640 K. The thick black lines correspond to the approximated slopes used to determine n and m in $D \propto t^n$ and $d \propto t^m$. The thick red lines correspond to the fit with γ=0.8 in the laws $D \propto [t/ln(t)]^{1/2(1-\gamma)}$ and $d \propto [t/ln(t)]^{1/3(1-\gamma)}$. From Ref.[99].

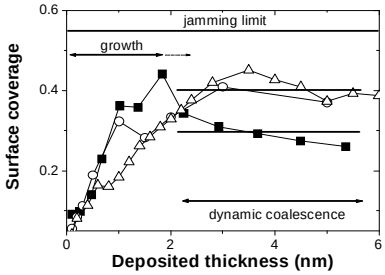

FIG. 34: Growth of Ag/MgO(001) analyzed by GISAXS. Surface coverage obtained by GISAXS as a function of the deposited thickness. Filled squares, T=300 K; open circles, T=540 K; up triangles, T=640 K. From Ref.[99].

6. Equilibrium shape, Wulff-Kaischew construction and adhesion energy

GISAXS yields unique information on the island shape, *in situ*, not destructively, which is especially interesting on a theoretical point of view. In most of the studied systems, there are regimes in which the islands reach there equilibrium shape, allowing to deduce the adhesion energy. Indeed, when the metal diffusion on the surface is fast enough, the islands reach their equilibrium shape on a time scale much shorter than that of the measurements, *i.e.* a sub-second time-scale. This procedure has been applied in the different growth cases presented above for Pd/MgO(001)[16,18], Pt/MgO(001)[20], Au/TiO_2(110)[135] and Ag/MgO(001)[99].

In this last case, for instance, at 640 K, the island shape is a truncated octahedron whose aspect ratios, height over width H/d, and $r_H = h/(H-h)$ between the top and bottom height, are constant below 1.6 nm deposited (Fig. 35). The adhesion energy is related to the aspect ratio by application of the Wulff-Kaischew construction[195,196] as:

$$\beta = \sigma_{001}(1 - 1/r_H), \tag{5.1}$$

where σ_{001}=1.20 J.m^{-2} (Ref.[211]) is the surface free energy of the (001) facet of Ag. $r_H \simeq 3.0$ yields $\beta \simeq 0.80 \pm 0.1$ J.m^{-2}, which compares well with the most recent determination. In the deposition thickness range of 1.6-2.2 nm, the ratio H/d decreases, meaning that the islands become flatter. This is expected as during the nucleation and growth regime, the islands grow mostly by capture of diffusing species in their surface of influence rather than by direct impingement on them. Indeed, while the (111) side facets grow from both vapor phase and atom diffusion, the (001) top facets grow mostly from the vapor phase as if they were isolated, because of the high energy barrier an atom has to overcome to jump from a (111) to a (001) facet[203,204]. Then, above a deposited thickness of 2.2 nm, the ratio H/d increases. During the coalescence regime, it has been pointed out that the facets play an important role. Due to the facets, the diffusion is not the limiting process, but the limiting step of the relaxation following the coalescence is the

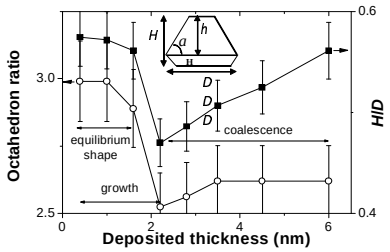

FIG. 35: Growth of Ag/MgO(001): Evolution of the island shape as a function of the deposited thickness at 640 K. Filled circles, octahedron aspect ratio *i.e.* $h/(H-h)$ with Y-axis on the left hand side; filled squares, H/d with Y-axis on the right hand side. Inset: side view of a truncated octahedron. From Ref.[99].

nucleation of a germ of the size of the smallest facet on a larger facet[212,213]. In the considered cubo-octahedron, the larger facets are the {001} and {111} facets of the upper island part, and the smaller facets are the {111} and {011} facets of the bottom part. Due to experimental uncertainties, one can not distinguish which facet among {001} or {111} is the largest. The increase of the H/d ratio would indicate that the island growth occurs preferentially on the {001} facet, which would be the largest facet of the cubo-octahedron.
In the $Au/TiO_2(001)$ case, during the coalescence stage, the aspect ratio H/R is nearly constant while the correlation coefficient ρ between the particle height and radius is close to one, indicating that clusters are close to equilibrium. The truncated sphere shape and the full size distribution allow to calculate a mean contact angle θ_c and an adhesion energy from the Young-Dupré formula $E_{adh} = \gamma_{Au}(1+\cos\theta_c)$, where $\gamma_{Au} = 1.131$ J/m^{-2} is the surface energy of gold[151], as a function of the coverage. The value of $\theta_c = 130 \pm 5^\circ$ for the contact angle of large particles is again in good agreement with the most precise determinations[178]. The finding of a change in contact angle (adhesion) around a mean size of $R >\sim 1.3$ nm (~ 500 atoms/cluster, average thickness of 0.6 nm) at the onset of the particle coalescence is compatible with the transition from "flat" 3D shape to spherical 3D shape around a coverage of 0.4-0.6 nm[178,179]. The GISAXS measurements are less sensitive to the 2D or quasi-2D particles seen by low energy ion scattering[191] or scanning tunneling microscopy[179]. These quasi-2D particles are dispersed on terraces and appear at the early beginning of the growth (below 0.2 nm); their height is between 1 and 3 monolayers. But they are in fact mixed with "flat" 3D clusters that mainly grow along the step edges[179,184], a fact that may explain the slight GISAXS anisotropy observed at the beginning of the growth on the mean spacing between particles in the $[1\bar{1}0]_{TiO_2}$ and $[001]_{TiO_2}$ directions. The morphological transition from 2D or quasi-2D to "flat" 3D particles was interpreted by a stabilization of "flat" 3D particles thanks to an accumulation of vacancies on the substrate below the particles[184].

B. Surface nanofacetting: the case of Pt on W(111)

The importance of bimetallic catalysts has been increasing in recent decades[214]. In particular refractory metals (W, Mo, Re, etc...) with Pt-group metals are active catalysts for hydrogenation and hydrogenolysis reactions[215–218]. The large majority of the studies devoted to these systems have focused on the interaction of ultrathin metal films with atomically smooth, close packed substrates, *e.g.* *fcc*(111), *fcc*(100), *bcc*(110), *bcc*(100) etc... Structural rearrangement in the overlayer have been observed, with little or no change in the substrate. By contrast, recent studies have addressed the interaction of ultrathin metal films on unstable atomically rough substrates [219–221]. For instance, a *bcc* metal like W exposing a (111) surface covered with 1 ML of another metals (Pt, Pd, Rh, Ir, Au). In this case, the surface undergoes a massive reconstruction (Fig. 36) to form three-sided pyramids of nanometer scale dimensions exposing {211} facets[222,223]. The process is activated at temperatures larger than 700 K and is reversible: after evaporation of Pt, a flat W(111) surface is recovered. The faceting transition has been attributed to the surface energy anisotropy[222,224,225] and is kinetically limited by surface diffusion. The fundamental questions of surface morphology instability in a bimetallic system like Pt/W(111) against faceting have initiated a wealth of experiments using different techniques (STM[222,223], LEED, AES, LEEM[226,227], XPS[228]). However, none of them allow to follow *in situ*, in real time, the faceting transition combining a crystallographic and a morphological (nanometer scale) characterization. In addition nanostructured surfaces can be used as templates to grow ordered dots exhibiting for instance magnetic properties. For that sake, a detailed study of the faceting of Pt/W(111) has been performed by GISAXS[136] as a function of time and temperature to determine the appropriate conditions for the ordering of small nanopyramids. Then this template has been used to grow Co nanostructures.

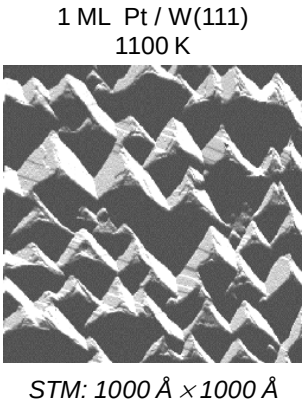

FIG. 36: STM image of Pt/W(111) which has undergone faceting after thermal treatment at 1100K. Notice the three side {211} nanopyramids. Courtesy of T.E. Madey.

1. *Nucleation and growth of 3-fold symmetry nanopyramids*

The first onset of nanofaceting of 1 ML of Pt on W(111) was observed by GISAXS at 715 K, and its evolution was followed for increasing temperatures up to 1340 K. Fig. 37 shows and example of GISAXS pattern (and analysis) at 800 K. Two well defined scattering lobes are visible indicating that neighboring pyramids are short range ordered at this temperature. The lobe located at $q_{\|} > 0$ extends farther along the q_z direction than the lobe at $q_{\|} < 0$, because of the 3-fold symmetry of the nanopyramids and because the Friedel law does not apply for GISAXS images[58]. The measurement of the tilt angle of the facets with respect to the surface plane is difficult because of the broadness of the scattering rods and because the interference function tends to re-orientate the scattering rods perpendicular to the surface plane and not perpendicular to the facets. The exact orientation of the facets (*i.e.* 211)has been obtained at this stage by measuring the facet truncation rods by GIXD (see Ref.[136]). Indeed, at wide angles, the information concerning the short range order between pyramids is lost and thus the truncation rods are perpendicular to the facets. The surface morphology (symmetry, pyramid shape, facet orientation, see Fig. 38) was deduced from full quantitative

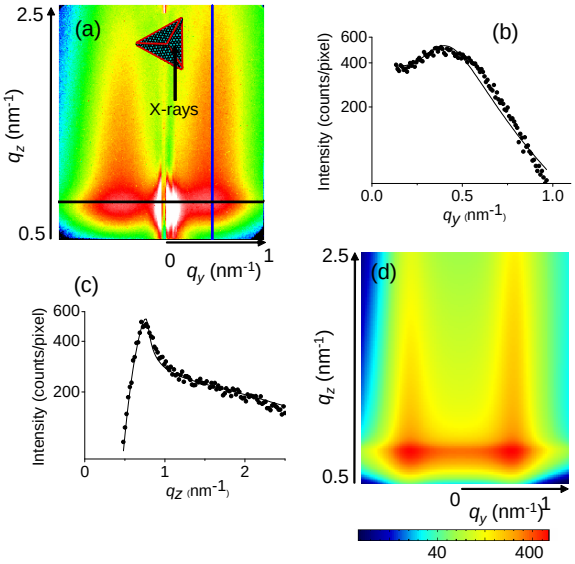

FIG. 37: a) GISAXS image (and scattering geometry in inset) for 1.1 ML of Pt on W(111) annealed at 800K. b) Cross section of the experimental image parallel to the surface plane (thick black line) and best fit. c) Cross section of the experimental image perpendicular to the surface plane (thick black line) and best fit. d) GISAXS image simulated with the parameters obtained from the fit of both cross sections. Note that the specular beam is not simulated. From Ref.[136].

GISAXS analyses. Previous analysis by STM[227] has shown that the faceted surface is made of pyramids and pits (inverted pyramids) to keep the amount of matter constant. The three-sided pyramids were modeled with a W-core

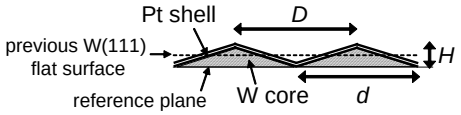

FIG. 38: Sketch of the morphology of the faceted Pt/W{211} surface.

and a 1 ML Pt-shell ($\Delta d = 0.27$ nm and $\Delta H = 0.10$ nm). Distributions of lateral sizes and heights were taken into account using Gaussian probability laws. The spatial organization of the pyramids has been modelled comparing the different approximations LMA[116] and DA[115] using a 1D paracrystal [79,130] , and SSCA[21,135], Sect. IV C) to better accound for size-spacing correlations, as evidence by STM Ref.[229]. We refer to the publication[136] for more details on the quantitative analysis. The average morphological parameters increase slowly between 715 and 800 K and then faster above 800 K. The ratio of the distance between pyramids and their lateral size (D/d) is approximately constant (1.1-1.2) which shows that the the pyramids are connected at all temperatures and the surface is fully faceted. This is confirmed by the absence of CTR's from the W(111) surface (see Ref.[136]). The nucleation density of pyramids (3.10^{12} cm^{-2}) has been estimated from the mean inter-pyramid distance at the onset of nanofaceting. Interestingly the minimum lateral size of the nanopyramids measured by GISAXS is estimated to be 5.16 nm. This minimum size for the nucleation arises from the competition between the surface energy gain and the energy cost of the facet edge to buckle and make a 3-sided pyramid. The energy per unit length of the facet edges (η=2.5 eV/nm at 715 K) has been deduced from geometric arguments. The sizes and separation of the pyramids were found to increase with temperature until the interference effect was no longer visible at 1040 K. Above this temperature, the angle of the facets is clearly defined (19.5°), corresponding to {211} facets. The facet rods get more intense and narrow as the facets size increases.

2. Validity of the DWBA: GISAXS as function of the incident angle

The large pyramids obtained after annealing at 1340 K were used to investigate the effects of grazing angles of incidence and exit and the validity of the first order DWBA in GISAXS. Fig. 39) shows GISAXS patterns recorded for different incident angles. For $\alpha_i \ll \alpha_c$ ($\alpha_i = 0.1°$ in Fig. 39a), only one (label 1) is visible. For $\alpha_c/2 \ll \alpha_i \ll \alpha_c$, (see Fig. 39b-c) , a second rod appear (label 2). The rod with the smallest emergent angle, pointing to the direct beam, is due to the single scattering process (BA term). The rod with the largest emergent angle comes from the second scattering process in Eq. 4.7, which takes into account first the reflection of the incident beam on the surface and then the scattering of the reflected wave by the pyramids. The angle separating these two scattering rods is $\Delta\alpha = 2\alpha_i$. Cross sections perpendicular to both scattering rods clearly show that the FWHM of the upper scattering rod is much larger than the FWHM of the BA scattering rod, which is not accounted for by the standard DWBA. This broadening arises because the reference surface can not be taken as flat: a higher order DWBA[230] would be needed. When $\alpha_i > \alpha_c$, the upper scattering rod vanishes (see Fig. 39d) because, above α_c, the Fresnel coefficient of reflection decreases very quickly as function of the incident angle. However in Fig. 39d, a new characteristic feature appears: a broad scattering rod (label 3 of Fig. 39-d) points toward decreasing exit angles (α_f) and after an elbow changes into a narrow scattering rod pointing toward increasing emergent angles. The first part originates from the third process in Eq. 4.7. It results from the scattering of the incident wave by the pyramids followed by a reflection of the scattered wave by the average surface plane. This is because, as α_f decreases, the wavevector transfer perpendicular to the surface reads: ($p_z = -k_{f\,z} - k_{i\,z} = 2\pi/\lambda[-\sin(\alpha_f) + \sin(\alpha_i)]$) decreases, and thus the scattering rod points toward decreasing angles. At $\alpha_f < 0$, the scattering rod is hidden by the surface plane. It crosses the BA scattering rod at $\alpha_f = 0$ making an elbow. For the same reason as before, the FWHM of the scattering rod arising from the third process in Eq. 4.7 is much larger than for the BA scattering rod. This highlights the breakdown of the first order DWBA to reproduce correctly broadening effects. The fourth term in Eq. 4.7, could not be isolated because it gives a significant contribution only for $\alpha_i \ll \alpha_c$ and $\alpha_f \ll \alpha_c$. As a conclusion the main features of the GISAXS images can be simulated in the framework of the first order DWBA. However to make a detailed study of supported nanostructures, they must be small enough, *i.e.* $q_z\sigma < 1$ and $p_z\sigma < 1$, where σ is the roughness of the surface[56].

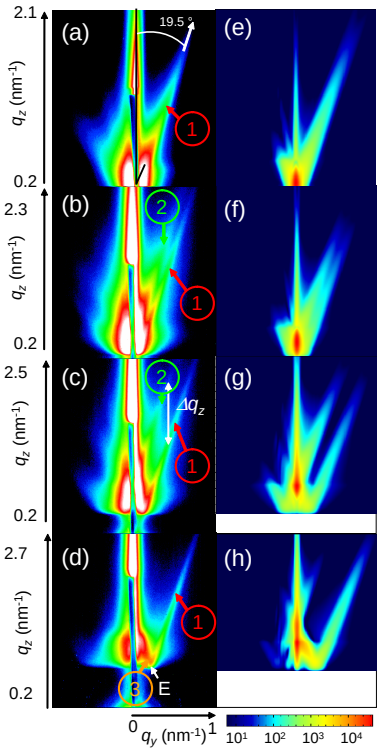

FIG. 39: a)-d) GISAXS images at increasing incident angles (0.1°, 0.22°, 0.42° and 0.68°) for a faceted Pt/W{211} surface. The labeled rods refer to the first, second and third term in the first order DWBA expression. The letter E stands for the elbow (see text). e)-h) Corresponding GISAXS simulations. The intensity scale is logarithmic.) From Ref.[136].

3. The growth of Co on a faceted Pt/W{211} surface

The nanofaceted Pt/W{211} surface with the smallest three-sided pyramids (obtained by a 10 min annealing at 715 K) has been used as a nanotemplate for the growth Co nanostructures. Although Co and Pt form ordered alloys [231], and Pt has a strong tendency to segregate[232], we expect a preferential nucleation of Co nanostructures induced by the surface morphology, *i.e.* at the apex of the pyramids or at the bottom of the pits. The surface was covered at RT by 4 ML of Co. The corresponding GISAXS image was more intense in agreement with the increase of matter. Moreover the asymmetry of the image was preserved (3-fold symmetry) suggesting that Co does not alter the initial morphology of the surface. The increase of intensity was interpreted as arising from 3D nanostructures of Co correlated with the Pt/W nanopyramids. The evolution of the system upon annealing was rather complex and will not be commented any further here.

C. Self-organized growth of nanostructures

The miniaturization of devices makes their production lengthy and expensive when using conventional techniques like lithography. An alternative is the self-organized growth process, which takes advantage of a regular surface nanopatterning to control the nucleation and growth processes, avoiding random nucleation, and giving rise to collections of nanoparticles with a narrow size distribution and an ordered spatial arrangement. Several routes have been explored for nanostructured surface: vicinal surfaces[233] (exhibiting a regular step array), surfaces strained by buried nanostructures[234], ordered phases of adsorbates[235], surface reconstructions[52,236,237], thin films of a few monolayers having coincidence lattice sites with the substrate[206,238] or buried dislocation networks[1,239]. However fabricating a regular pattern is not enough, it is necessary to avoid homogeneous nucleation in order to grow only one nanostructure per unit cell[206]. The parameters of control for the growth are the temperature and the flux of atoms deposited on the surface. To find the optimal experimental conditions, the use of *ex situ* characterization tools may be very time consuming. At variance *in situ* and more suitable real time X-ray techniques techniques offer the opportunity of a feed back control of the growth processes to tune the growth parameters (fluxes, temperature) toward self-organization.

They provide the crystallographic structure (GIXD) as well as the shape, size and spatial organization (GISAXS) of a macroscopic number of nanostructures. In the following, we focus on recent GISAXS studies of ordered growth of Co or Ni nanostructures on different kind of surfaces: (i) the Au(111) surface reconstruction as a model system[22]; (ii) a kinked vicinal surface of Au(111)[19,240]; (iii) a thin film of Ag strained by a misfit dislocation network buried at the interface with a MgO(001) substrate[1]; (iv) a cobalt-oxide thin film induced patterned by a buried misfit dislocation network[241].

1. *The ordered growth of Co on Au(111)*

The growth of Co nanostructures on Au(111) is certainly one of the most popular example of ordered growth of nanostructures on metal surfaces[32,52]. The main advantages of this system are (i) its robustness in temperature since the growth is ordered in a wide range of temperature[242] (120 K to 400 K); and (ii) the large size of its unit cell. The Au(111) surface exhibits a $(22 \times \sqrt{3})$ reconstruction that has been characterized by GIXD[243], STM[244], and Helium Atom diffraction[245]. Top layer atoms are successively in *fcc* and *hcp* stacking and both domains are separated by stacking-faults. As the Au(111) surface has a threefold symmetry, three different variants of the reconstruction coexist on the surface. A superstructure involving two variants of the reconstruction, rotated at 120° and separated by a kink, is called herringbone reconstruction. For length scales of about 100 nm, different domains of the herringbone reconstruction rotated at ±120° are observed in agreement with the symmetry of the surface. Consequently the Au(111) surface is spontaneously ordered over areas of 100×100 nm^2 and more importantly it is a template for the ordered growth of Co nanostructures. The nucleation of Co on Au(111) is heterogeneous and occurs at the kinks of the herringbone reconstruction (see Fig. 40a-c) thanks to an insertion mechanism[246]. Different questions have been addressed by GISAXS: in the submonolayer regime, the size and content of the unit cell of Co nanostructures have been studied as a function of deposit. At the coalescence of the Co nanostructures and beyond, the structure of the Co thin film has been investigated by Anomalous GISAXS and GIXD. At last, in order to increase the blocking temperature of the Co nanostructures, nanopillars have been grown by sequential deposition of Co and Au.

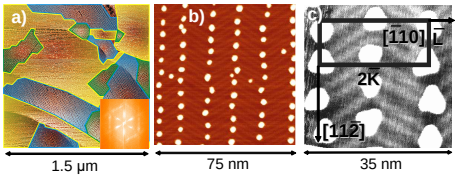

FIG. 40: a) STM images of the self-organized growth of Co nanostructures on the Au(111) herringbone reconstruction. a) Large scale image ($1.5 \times 1.5 \mu m^2$) and its Fourier Transform (Inset). The three different domains of the Co nanostructures network are highlighted by different colors. b) Image of one domain for 0.05 ML of Co. c) Small scale image. A sketch of the unit cell is shown (from Refs.[22,247]).

a. Qualitative interpretation of the scattering rods by the Co nanostructures network The network of Co dots is characterized by a unit cell (**A**,**B**) of rectangular shape of about $7.7 \times 15 - 50$ nm^2 (Ref.[248]) filled with two nanostructures of approximately two monolayers high (see Fig. 40c). The main crystallographic axis of the Co dots network are aligned along the $\langle 11\bar{2} \rangle$ and $\langle 1\bar{1}0 \rangle$ directions referring to the *fcc* lattice of Au. We call intra-row spacing the distance between the nanostructures in the $\langle 11\bar{2} \rangle$ direction, *i.e.* governed by the size of the $22 \times \sqrt{3}$ reconstruction. The inter-row spacing is the distance between the nanostructures in the $\langle 1\bar{1}0 \rangle$ direction (kink periodicity). Figures 41a and b show respectively two GISAXS images measured for an incident beam aligned along the main crystallographic orientations $\langle 1\bar{1}0 \rangle$ and $\langle 11\bar{2} \rangle$. They are both characterized by correlation peaks in the surface plane showing the presence of a bidimensional order. The normalized FWHM of the scattering rods of the intra-row spacing ($\Delta q_{\parallel}/q_{\parallel} = 3\%$) is very small (see Fig. 41a). This reveals a long range order arising from the underlying $N \times \sqrt{3}$ reconstruction for which the periodicity is very well defined ($N = 22 \pm 1$). About the inter-row spacing (see Fig. 41b), the scattering rods are much broader revealing a short range order. A one-dimensional analysis gives a mean distance of 8.5 nm and a standard deviation of 2.1 nm. The quality of the order in this direction can be assigned to the fluctuations of the spacing between two kinks of the reconstruction. Fluctuations are large because the energetic equilibrium of the surface structure is mainly controlled by the $22 \times \sqrt{3}$ reconstruction and the kink spacing is a second order effect. In the direction perpendicular to the surface the scattering rods are very extended due to the very small height (2 ML) of the nanostructures as put in evidence earlier by STM [52].

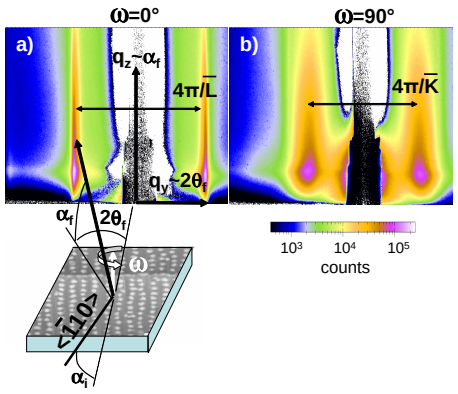

FIG. 41: a) Sketch of the principle of a GISAXS measurement and experimental image for an incident X-ray beam aligned along the $\langle\bar{1}10\rangle$ direction. The distance separating the scattering rods is inversely proportional to the intra-row distance (L). b) Experimental GISAXS image obtained for the beam aligned along the $\langle 11\bar{2}\rangle$ direction. The inter-row distance (K) is probed (from Ref.[22]).

b. 3D characterization of reciprocal space of Co/Au(111) by GISAXS In order to fully characterize the supercrystal of Co nanostructures, a mapping of the reciprocal space has been performed at the nanometer scale. In Fig. 42 a map of the reciprocal space in the surface plane is shown for a deposit of 0.9 ML of Co, *i.e.* for half-coverage of the surface. This map results from 85 GISAXS images measured at different azimuths, rotating the sample by step of 1°. The intensity at $q_z \simeq 0$ (*i.e.* at the Yoneda peak) has been extracted for each GISAXS images. The sixfold symmetry is in agreement with the threefold symmetry of the surface combined with the Friedel law $I(\mathbf{q}) = I(-\mathbf{q})$ (see Sect. IV B 5) which applies for $q_z = 0$[58]. Let us consider the contribution of only one variant of the surface reconstruction. From the schematic drawing of the unit cell shown in Fig. 43c the position of the different peaks can be assigned. The main peak arises from the intra-row spacing (01), narrow and intense (Fig. 42). The second one is given by the inter-row spacing and is much broader. It is called (20) in agreement with the pattern of the unit cell which is statistically centered along the $\langle 1\bar{1}0\rangle$ direction. The (10) and (30) peaks are forbidden in agreement with the previous remark. From these simple arguments the mean position of the Co nanostructure inside the unit cell reads $(\overline{K}, y)$ where $\overline{K}$ is the mean inter-row spacing and y has to be determined (see Fig. 43c). This preliminary analysis gives some insight into the structure of the unit cell of Co nanostructures, however due to disorder much caution is necessary and a quantitative analysis is mandatory to go further on.

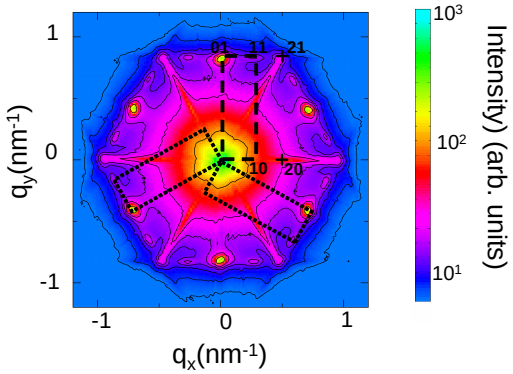

FIG. 42: Map of the reciprocal space of the Co dots network in the surface plane. It has been measured for 0.9 ML of Co. The three variants of the herringbone reconstruction are observed at ±120° and one can define the rectangular elementary unit cell of the reciprocal space. The narrow intra-row peak (01) and the broad inter-row peak (20) are clearly evidenced, as well as the (11) et (21) crossed peaks. From Ref.[22].

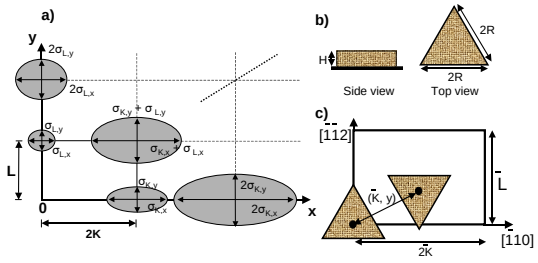

FIG. 43: a) Sketch of the probability density of the first neighbors distance in the 2D paracrystal model. The gray areas bound the most probable areas of the probability distribution. $2\overline{K}$ and $\overline{L}$ are the mean distances between the nodes. $\sigma_{K,x}$, $\sigma_{K,y}$, $\sigma_{L,x}$ and $\sigma_{L,y}$ are the standard deviation of the nearest neighbor distance distributions. In the paracrystal framework, the disorder propagates in a cumulative way from nodes to nodes. b) Shape and size of the Co nanostructures. c) Rectangular unit cell of the Co nanostructures network. From Ref.[22].

c. Modeling and quantitative analysis of the growth of Co/Au(111) In order to calculate the intensity scattered by the network of Co nanostructures a model is built relying on the above analysis of the growth of Co on Au(111) and previous STM images (*e.g.* Fig. 40).

- The spatial organization is modeled by two perpendicular paracrystals[79] (see Sect. IV C 5) which describe the intra-row and inter-row spacings (Fig. 43a). In the framework of this model, both directions are independent (ideal paracrystal). The probability laws of the distances between first neighbors are bidimensional with a Gaussian shape and characterized by the mean distances ($\overline{L}$ and $2\overline{K}$) and the standard deviation ($\sigma_{K,x}$, $\sigma_{K,y}$, $\sigma_{L,x}$ and $\sigma_{L,y}$).
- The unit cell is built by two nanostructures of triangular shape (see Fig. 43b). One is located at the node of the lattice and the other one, rotated by 180°, is close to the center of the unit cell $(\overline{K}, y)$ (Fig. 43c). The fluctuations of positions inside the unit cell are modeled by a Debye-Waller type disorder.

To fit the parameters of the model, cross sections of the GISAXS images have been extracted. Then the parameters are fitted minimizing the total χ^2. As an example, let's consider the cases of 0.2 and 1 ML of Co deposited at RT (see Fig. 44a-f and g-l). Two GISAXS patterns have been measured for both deposits with the X-ray beam impinging in the main azimuthal directions $\langle 1\bar{1}0 \rangle$ and $\langle 11\bar{2} \rangle$. The extracted cross sections are shown with dotted lines. The parameters are fitted simultaneously and finally a GISAXS image is simulated and compared to the experimental one (see for instance Fig. 45).

The morphological parameters of the Co network are shown in Table I. First the relative uncertainty on the parameters of the 2D-paracrystal is much smaller (a few %) than the uncertainty on the Co dots size and position in the unit cell (20%). The mean inter-row and intra-row distances are: $2\overline{K} = 16.9$ nm and $\overline{L} = 7.7$ nm and the standard deviations are approximately constant. Therefore we confirm that the spatial organization is controlled by the surface reconstruction of Au(111) which induces preferential nucleation sites. The size and position of the Co dots are in agreement with previous STM studies until half-coalescence. The small y value shows that the inner Co dot is close to the edge of the unit cell (typical STM image Fig. 40c).

Above 1 ML of deposit, the fit of the parameters does not give reliable values revealing that the same modeling is not suitable to describe the observed GISAXS pattern beyond coalescence.

d. Beyond coalescence of Co nanostructures Using a simple model, and considering 2 ML high dots, the total intensity should decrease from 1 ML of deposit down to zero at 2 ML, when the film is continuous. Surprizingly, the experimental scattering rods were found to increase until 2 ML, and then decrease slowly, with sizeable intensity remaining even well beyond coealscence, for a coverage larger than 8 ML[248]! Moreover the scattering rods parallel to the surface plane do not broaden, indicating that the order quality is preserved at the coalescence of the nanostructures (see Fig. 46). To understand this experimental result, a topographic analysis of STM data has been performed by O. Fruchart *et al.* [22,248]. It was shown that a residual roughness still exists on the surface after coalescence of the Co dots with the same periodicity as the surface reconstruction of Au(111), which could explain some remaining intensity until 4 ML deposited, but not beyond. The origin of the signal for thicker deposits cannot be explained only by the topography. It was suggested that the intensity might arise from the underlying Au substrate, which could be strained periodically by the Co dots. Other effects such as interdiffusion are also possible since Au adatoms are very mobile at RT and the surface energy of Au is much smaller than the Co one. To check these hypotheses, Multiple

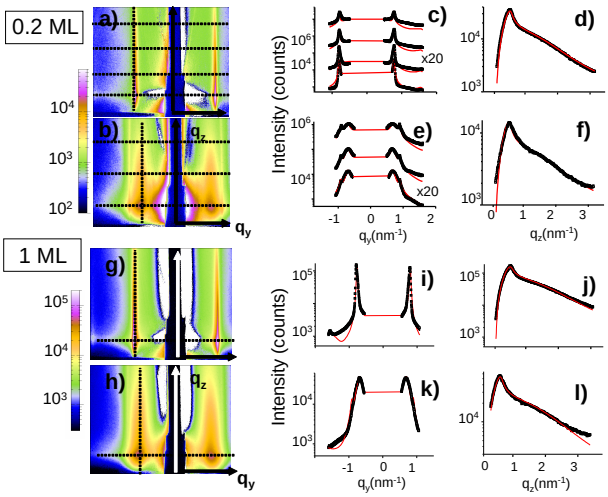

FIG. 44: GISAXS patterns and cut of intensities for a deposit of 0.2 ML of Co on Au(111) for an incident beam along $\langle 1\bar{1}0\rangle$ (a,c,d) and $\langle 11\bar{2}\rangle$ (b,e,f) azimuths. The dotted lines show the positions of the cross sections extracted for the fit displayed on the right of the image ($q_{\parallel}$ (c,e) and $q_{\perp}$ (d,f) cuts). The full line corresponds to the fit while the squares are the data points. From g) to j), same as from a) to f) but for 1 ML of Co on Au(111). Adapted from Ref.[22].

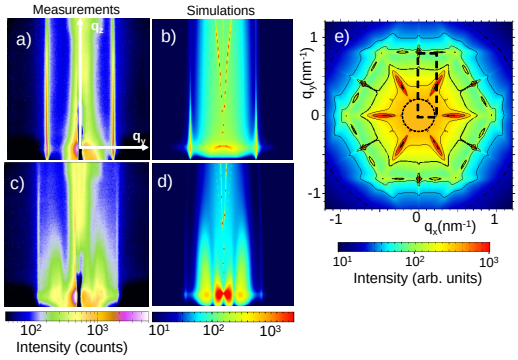

FIG. 45: For 0.3 ML of Co: a) and b) GISAXS patterns and their simulations for the beam along the $\langle 1\bar{1}0\rangle$ direction. c) and d) Same as a),b) but with the beam along the $\langle 11\bar{2}\rangle$ direction. e) Corresponding simulation of a map of the reciprocal space in the surface plane ($q_z = 0$), the agreement with Fig. 42 is remarkable. From Ref.[22].

Anomalous GISAXS measurements have been performed[22] in order to discriminate the contributions of Co and Au in the scattering rods.

e. Multiple Anomalous GISAXS[22] The principle of Multiple Anomalous GISAXS is to measure the intensity at different energies around an absorption edge of a chemical element of the sample. This modifies its scattering factor giving the opportunity to extract the structure factor and phase shift of each compounds assuming that preliminary absorption calibrations have been performed. GISAXS images have been collected at 9 energies around the Co-K edge (7.709 keV). In the framework of the DWBA and assuming that Co nanostructures have a small height and the depth of the electronic density variations of Au are small enough (< 1nm), the total intensity reads approximately (see Sect. IV B 7):

$$\frac{d\sigma}{d\Omega}(\mathbf{q}_1, E) \simeq |t_{01}(\alpha_i)t_{01}(\alpha_f)|^2 \left|F^0_{\mathrm{Co}}(\mathbf{q}_1) + F'_{\mathrm{Co}}(\mathbf{q}_1, E) + iF''_{\mathrm{Co}}(\mathbf{q}_1, E) + F^0_{\mathrm{Au}}(\mathbf{q}_1)e^{i\varphi}\right|^2 \tag{5.2}$$

where $F^0_{\mathrm{Co}}(\mathbf{q})$ and $F^0_{\mathrm{Au}}(\mathbf{q})$ are the Thomson scattering form factors of the Co nanostructures and the Au substrate respectively. $F'_{\mathrm{Co}}(\mathbf{q}, E)$ and $F''_{\mathrm{Co}}(\mathbf{q}, E)$ are the anomalous contributions of the Co nanostructures. φ is the phase

Co amount (ML)	Paracrystal parameters					
	$2\overline{K}$ (nm)	$\overline{L}$ (nm)	$\sigma_{K,x}$ (nm)	$\sigma_{K,y}$ (nm)	$\sigma_{L,x}$ (nm)	$\sigma_{L,y}$ (nm)
0.2	16.82±0.20	7.68±0.01	2.34±0.13	0.99±0.05	0.83±0.05	0.66±0.02
0.3	16.89±0.11	7.66±0.01	2.34	1	0.70±0.04	0.63±0.02
1	16.90±0.06	7.69±0.01	2.37±0.03	1.01±0.01	0.86±0.02	0.66±0.01
Co amount (ML)	Unit cell parameters					
	R (nm)	σ_R/R	H (nm)	y (nm)	Δ (nm)	Thickness (ML)
0.2	1.96±0.37	0.46±0.15	0.41	0.12±0.08	0.13±0.03	0.25±0.1
0.3	2.84±0.40	0.43±0.16	0.42	0.10±0.03	0.05±0.02	0.4±0.15
1	3.01±0.14	0.1	0.39	0.098±0.016	0.065±0.005	0.5±0.05

TABLE I: Results of the quantitative analysis of the GISAXS images. The parameters of the spatial organization are first presented (paracrystal) and then the parameters of the unit cell.

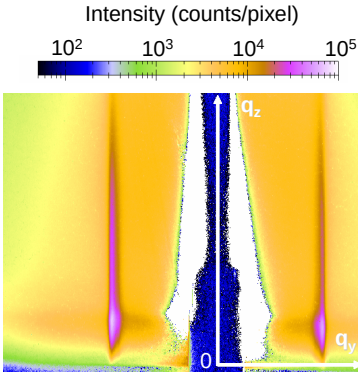

FIG. 46: GISAXS image measured for 6 ML of Co on Au(111). The incident beam is along the $\langle 1\bar{1}0 \rangle$ direction. Very narrow and intense scattering streaks are still visible with the initial periodicity of the Co dots network. However, there is a large background scattering compared to images measured for less than 1 ML of Co (from Ref.[22]).

shift between Co and Au arising from the different positions of the scatterers (see Fig. 47a). The experimental measurements have been performed for a deposit of 2 ML for which the Co dots have just coalesced in the intra-row direction[248,249]. The scattering rods have been analyzed in the direction perpendicular to the surface integrating the signal parallel to the surface plane to increase the signal/noise ratio (see Fig. 47b). The results show that almost all the intensity arises from the Co film (see Fig. 47c); the Au contibution being within the error bar. Hence, the hypothesis of a periodic interdiffusion of Au or strain field inside the substrate can be ruled out. We suggest that, in addition to a remaining topopgraphic effect, the Co still contribute to the GISAXS signal through the grain boundaries resulting from the partial coalescence of the Co nanostructures, the electronic density around these defects being smaller than in the unfaulted Co. This is supported by high resolution STM measurements[52,248] revealing the presence of defects at the coalescence due to the non commensurability of the Co and Au crystallographic lattices (see Fig. 48). The presence of these regular defects was also consistent with GIXD measurements[22].

f. Growth of Co nanopillars[247,248] The small size of the Co dots results in superparamagnetism at low temperatures. Larger islands are required to get potentially useful magnetic properties. Such large objects can be obtained in the form of Co pillars by sequential deposition. The basic idea relies on the observation in semiconductors[250] that, due to strain modulation, dots tend to stack vertically in successive layers; the in-plane organization then evolving toward a 3D organization. This method has been applied to the growth of Co pillars on Au(111) by O. Fruchart *et al.* (see Ref.[247]), obtained by repeating the alternate growth of a fraction of 1 ML of Co and with the amount of Au neede to complete a layer, thus yielding a smooth surface. Altough existence of these pillars had been proven by indirect

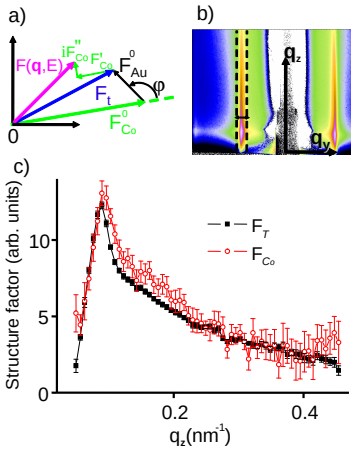

FIG. 47: a) Principle of anomalous scattering. $F(\mathbf{q}, E)$ and $F_T(\mathbf{q})$ are respectively the total scattering factor, and the Thomson scattering factor, *i.e.* without the anomalous contribution. b) The intensity is extracted from the scattering rod of the intra-row periodicity at the coalescence stage. c) The total structure factor (F_T) of the scattering rod of the intra-row distance is shown as well as the contribution of Co as deduced from the fit (F_{Co}). The Co term is clearly predominant. From Ref.[22].

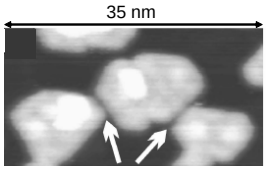

FIG. 48: STM image of 1.1 ML of Co on Au(111). The arrows show trenches between the Co nanostructures. They correspond to further grain boundaries (From Ref.[248]).

methods, *i.e.* STM and magnetic measurements, a more direct proof of the growth of ordered pillars was highly desirable. We thus performed *in situ* GISAXS measurements during the alternate growth beleived to lead to orderd Co pillars. The different steps were: (i) growth of ordered Co dots on Au(111) dots at RT (0.4 ML); (ii) subsequent growth of Au (3.6 ML) at 425 K to complete a smooth surface of 2 ML; (iii) sequential growth of Co (0.4 ML) and Au(0.6 ML) at 500 K (15 times). The intensity of the intra row and inter row rods was found to increase steadily during this process, confirming that the volume of matter of in the pillars was continuously increaseing. Moreover the intra-row scatering rods were found to stay very narrow, proving the preservation of the order during the process. Two GISAXS images of the pillars network and a map of the reciprocal space in the surface plane ($q_z = 0$) for 15 ML of Co and Au are shown in Fig. 49. The in-plane peaks shows that the order has not been destroyed and the map can be successfully compared to the previous one obtained for 0.9 ML of Co/Au(111) (see Fig. 42). The same peaks can be measured at the same positions.

g. Conclusion GISAXS has been applied to the study of the model system Co/Au(111). In the submonolayer regime the unit cell and the spatial ordering of the Co nanostructures have been characterized. At the coalescence and beyond anomalous GISAXS have shown (with complementary GIXD and STM) that a 2D network of grain boundaries persists for a 8ML-thick film of Co. At last a direct proof of the growth of Co nanopillars by sequential deposition of Co and Au is put in evidence. This Co/Au(111) example highlights the capability of the GISAXS technique to probe buried density fluctuations.

2. The ordered growth of Co on a kinked vicinal surface of Au(111)

The growth of Co on Au(111) is well ordered over areas of 100×100 nm^2. However at larger scales, the three-fold symmetry of the surface implies that other variants of the herringbone reconstruction exist on the surface thus

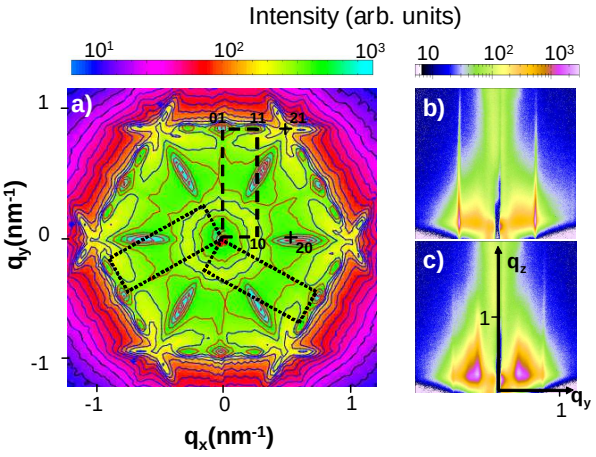

FIG. 49: a) Map of the reciprocal space of pillars at $q_z = 0$ (from Ref.[22]). b) and c) GISAXS images for an incident beam aligned respectively in the $\langle 1\bar{1}0 \rangle$ and in the $\langle 11\bar{2} \rangle$ directions.

limiting the long-range order (see Fig. 40a). Moreover defects, mainly steps, affect the coherence of the network. The use of vicinal surfaces allows to solve both drawbacks. Breaking the symmetry, only one variant of the reconstruction is favored and steps, which were the main defects, are now ordered and participate to the patterning of the surface. The first studies of the growth of Co on vicinal Au surfaces have been performed in the group of Sylvie Rousset[246,251]. They have put in evidence the crucial role of temperature[252] in the long range order quality of the Co dots network. GISAXS experiments were performed on the SUV instrument of the BM32 beam line (ESRF) to study the growth of Co on a slightly kinked vicinal surface of Au(111). As shown below, complementarity between GISAXS and STM is clearly put in evidence.

a. The kinked Au(677) surface - a combined STM and GISAXS study The kinked vicinal surface of Au(111) (see Fig. 50a) is made of a regular staircase of monoatomic steps (0.235 nm). Contrary to the nominal Au(111) surface, only one variant of the reconstruction is observed due to an energetic raised degeneracy thanks to the symmetry breaking. The reconstruction is put in evidence by STM showing a surface corrugation with double lines in the $\langle \bar{2}11 \rangle$ direction, revealing the presence of stacking faults between domains of *fcc* and *hcp* crystallographic structures as already seen in the case of the Au(788) surface[246]. The surface under study is close to a Au(677) surface but the step

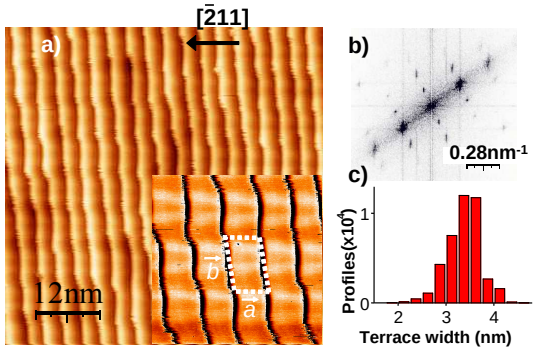

FIG. 50: a) STM image of the kinked Au(677) surface. Inset: Zoom on the surface where the vicinal staircase has been subtracted numerically to highlight the double stacking fault lines of the reconstruction. **a** and **b** are the base vectors of the unit cell. The kinks are visible as diffuse and tilted areas. The angular offset ε between the average step direction and the $[0\bar{1}1]$ direction is $5° \pm 1°$. b) Fourier transform of an image. The periods of the step network and the reconstruction/kinks are visible. c) Histogram of the terrace width performed over 20000 profiles. From Ref.[240].

edges are slightly misoriented with respect to the $\langle 0\bar{1}1 \rangle$ direction. This is revealed by the occurrence of kinks at the

step edges as seen by STM (Fig. 50a). A more precise analysis shows that they are not monoatomic kinks, but they pack periodically and make tilted and diffuse areas, and are trapped in between the stacking fault lines, inside *fcc* stacking areas. This behavior has already been observed on the Au(111) surface by Repain *et al.* [253]: the stacking fault lines cross only the {111} step edges and never the {100}. The kinks are therefore excluded from the *hcp* areas and pack together in the *fcc* areas.

3D GISAXS measurements were performed to obtain statistical information of the kinked Au(677) surface morphology. 2D GISAXS patterns were collected at different azimuth rotating the sample by steps of 1° over a large angular range (140°), yielding a tomographic measurement of the reciprocal space close to the origin. A projection of the GISAXS intensity in the surface plane is shown in Fig. 51. The (10) and (20) scattering rods from the step network are visible, as well as those, (01) and (02), arising from the kink long-range order, turned by $\pi/2-\varepsilon$; where the angular shift ε arises from the rotation of the mean step edge orientation induced by the kinks. The (11) and (12) higher order scattering rods coming from both periodicities have also been measured. There existence shows that the surface cannot be described by a simple superposition of two 1D networks (steps and kinks): a global model has to be developped to calculated the diffuse scattering. However one may wonder if the GISAXS intensity comes from the

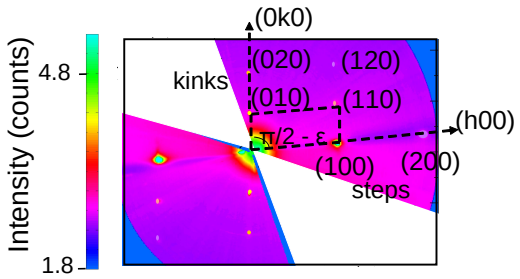

FIG. 51: Experimental map of the reciprocal space in the surface plane of the kinked vicinal surface of Au(111). The angular offset ε deduced from this map is ε =4.95° (from Ref.[240]).

surface topography and/or the surface reconstruction which modifies also the electronic density contrast. GISAXS measurements performed on the Au(111) surface did not reveal any signal from the reconstruction. Assuming that the dilatation effects induced by the reconstruction on Au(111) and Au(677) are similar, the kinks are probably responsible for the diffuse scattering observed at the periodicity of the reconstruction. Thus the intensity scattered by the kinked Au(677) surface can be evaluated only by a topographic model.

b. The paracrystal model: a tool to describe kinked vicinal surfaces[19,120,240] The calculation of the intensity scattered by surface morphologies is a classical problem in surface science. In the case of a perfectly ordered surface, only the calculation of the structure factor of the unit cell which repeats on the surface is necessary. In the non ideal case, a statistical description of the surface is necessary. Since the pioneer work of Lent and Cohen[254] and Pukite *et al.*[255], many analytical results have been obtained[256,257]. However until now these calculations were based on a 1D description of the surface topography and focused on Spot Profile Analysis Low Energy Electron Diffraction (SPA-LEED)[258,259], Helium Atom Scattering (HAS)[260–262] or Reflection High Energy Electron Diffraction (RHEED)[263] techniques. A method based on the paracrystal model allows to extend older works in the framework of X-ray scattering considering a 3D description of the surface morphology[19,120,240]. Details of this approach are given in the following for the kinked vicinal surface. A fixed step height h and a fixed kink size a are first assumed when modelling the surface topology, in order to simplify the calculation. An elementary building block is defined in the form a parallelepiped of height h and lateral size a, semi-infinitely extended in the y direction (Fig. 52). Its form factor reads:

$$F_{\text{kinked vicinal}}(\mathbf{q}) = \int_{-h/2}^{h/2} e^{iq_z z}dz \int_{-k/2}^{k/2} e^{iq_x x}dx \int_{-\infty}^{0} e^{iq_y y+\mu y}dy$$
$$= \frac{-4i}{q_x q_y q_z}\sin(q_z h/2)\sin(q_x k/2).$$

To build a whole crystal and its surface, this elementary object is ordered in two main directions: along the mean step edge and perpendicular to the steps to take into account possible correlations between kinks of neighboring steps. This was done in the framework of the ideal 2D paracrystal model considering a probability law of the distance

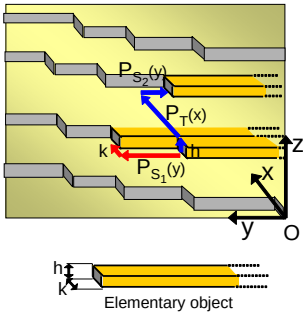

FIG. 52: Sketch of the principle of the construction of a kinked vicinal surface (fixed kink and step dimensions). Elementary object: a parallelepiped of height h, width k and semi-infinitely extended in the y direction. The surface is built similarly to the vicinal surface adding step by step elementary objects along two directions : along the step edges and perpendicular to the steps. A probability law $P_{S_1}(y)$ provides the distance distribution between the kinks at the step edges and two probability laws give the terrace width $P_T(x)$ and the relative displacement in the y direction of two neighboring kinks at adjacent step edges, $P_{S_2}(y)$. From Ref.[240].

between nearest neighbor kinks in the two main directions. This hypothesis is questionable because kinks (like steps) interact *via* long-range interactions (*e.g.* elastic interaction), which should in principle be taken into account via correlations. Such correlations were not intriduced as they would render the analysis much more complex and our purpose was to calculate the intensity scattered by a kinked vicinal surface assuming size distributions for the terrace width and the kink-kink distance. In summary, the surface is modeled thanks to an elementary object ordered along two directions; the ordering being modeled by an ideal 2D paracrystal. In the direction parallel to the mean step edge, the interference function reads:

$$S_{\parallel}(q_x, q_y) = \mathrm{Re}\left\{\frac{1 + e^{iq_x k}\widetilde{P}_{S_1}(q_y)}{1 - e^{iq_x k}\widetilde{P}_{S_1}(q_y)}\right\}, \tag{5.3}$$

where $\widetilde{P}_{S_1}(q_y)$ is the characteristic function of the kink-kink distance along the step edge. For the direction perpendicular to the step edges :

$$S_{\perp}(q_x, q_y, q_z) = \mathrm{Re}\left\{\frac{1 + e^{iq_z h}\widetilde{P}_T(q_x)\widetilde{P}_{S_2}(q_y)}{1 - e^{iq_z h}\widetilde{P}_T(q_x)\widetilde{P}_{S_2}(q_y)}\right\}, \tag{5.4}$$

where $\widetilde{P}_T(q_x)$ and $\widetilde{P}_{S_2}(q_y)$ are respectively the characteristic functions of the terrace width distribution and the characteristic function of the distribution of distances of the first neighbor kinks along a step edge (Fig. 52).

The kinked vicinal surface of Au(677) under study is a bit more complex as monoatomic kinks are packed together. This is modeled by larger kink with a size distribution $P_K(x)$. The previous result can be generalized for any kink size distribution (fixed step height):

$$\begin{aligned} I(q_x, q_y, q_z) = \left[\frac{2}{q_x q_y q_z}\right]^2 \mathrm{Re}\left\{\frac{(1 - \widetilde{P}_{S_1})(1 - \widetilde{P}_K(q_x))}{1 - \widetilde{P}_{S_1}\widetilde{P}_K(q_x)}\right\} \\ \times \mathrm{Re}\left\{\frac{(1 - e^{iq_z h})(1 - \widetilde{P}_T(q_x)\widetilde{P}_{S_2}(q_y))}{1 - e^{iq_z h}\widetilde{P}_T(q_x)\widetilde{P}_{S_2}(q_y)}\right\}. \end{aligned} \tag{5.5}$$

The total number of size distributions is four. To give explicit expressions they were modeled by Gaussian laws characterized by their first two moments (mean size and standard deviation). The kink size distribution $P_K(x)$, the kink-kink distance along the step edges $P_{S_1}(y)$, the terrace width distribution $P_T(x)$ and the distribution of the displacement of the kink position along (Oy) on a neighbor step edge, $P_{S_2}(y)$ have now to be extracted from the 3D GISAXS data.

c. Measurements and simulations Thirty cross sections have been extracted and fitted simultaneously (Fig. 53), thus strongly constraining the parameters of the above model (Eq. 5.5). Fig. 54 shows some of the fitted data. The relative amplitude of the scattering rods is well reproduced, in partcular the two orders of magnitude diffence in intensity between (10L) rod arising from steps and the (11L) cross term.

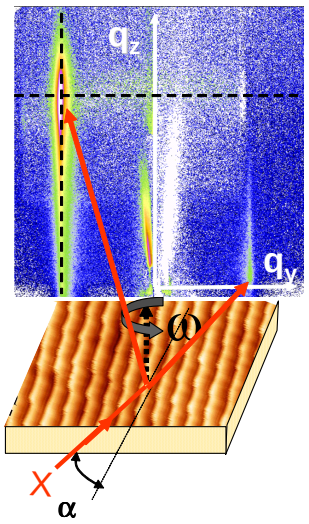

FIG. 53: Example of a GISAXS pattern. α is the incident angle perpendicular to the surface, ω is the in-plane orientation (azimuth angle) of the incident X-ray beam with respect to the average step direction. Here the X-ray beam is offset by $\omega = 6°$ with respect to the mean step edge direction. The scattering rod arising from the step network crosses the Ewald sphere at wide out-of-plane angles. Two cross sections (dotted lines) of intensity are extracted from this 2D map to fit the parameters of the model (from Ref.[240]).

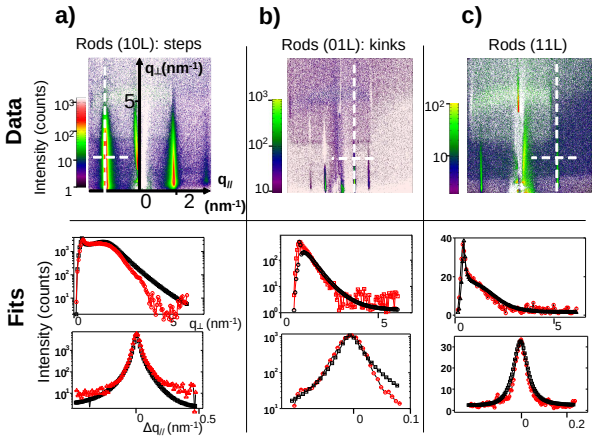

FIG. 54: Top: experimental GISAXS images of the step network a), kink network b) and cross term c). Bottom: fits (black) and data (red) of the cross sections parallel and perpendicular to the surface plane. The corresponding cross sections are shown on the GISAXS images (dotted lines). Adapted from Ref.[240].

d. Analysis of the parameters and comparison of STM and GISAXS results The model parameters are gathered in (Tab. II). The angular disorientation of the step edge with respect to the $(\bar{1}10)$ direction was found to be precisely 4.95° and the mean terrace size (3.42 nm) was found in good agreement with the STM values, while the standard deviation of the terrace width distribution was found to be twice smaller. This discrepancy arises mainly from the definitions of the terrace width distributions which are different in both cases. For the STM analysis, the terrace width distribution includes the fluctuations of the step-step distance (assuming straight lines), the fluctuations of the kink positions as well as those arising from their sizes. The quantitative analysis of the GISAXS data allows to distinguish between all these contributions, so the terrace width distribution (*i.e.* the step-step distance assuming they are straight) is much narrower in the GISAXS analysis.

The specific parameters deduced by GISAXS are the following. The kink size is about 3±1 monoatomic kinks packed together. They are found well ordered along two directions. Perpendicular to the step edge, they are at a distance of 3.42 nm (mean terrace size), with a standard deviation of a monoatomic distance *i.e.* 0.23 nm. The

Kink size			**Kink-kink distances**					
			Step P_{S_1}		**Terrace** P_T		**kink** P_{S_2}	
Width (nm)	Distribution (nm)	Height (nm)	S_1 (nm)	σ_{S_1} (nm)	T (nm)	σ_T (nm)	S_2 (nm)	σ_{S_2} (nm)
0.7	0.35	0.235	8.04	0.62	3.42	0.23	0	0.3

TABLE II: Topographic parameters of the kinked Au(677) surface deduced from the quantitative analysis of GISAXS data. The step height is fixed at 0.235 nm.

displacement along neighbor step edges is centered around zero and the fluctuations are very small (0.3 nm). This result illustrates the crucial role of the reconstruction which induces the long-range ordering of the kinks from step to step. Parallel to the step edges, the kinks are ordered according to the period of the reconstruction, 8.04 nm, and the standard deviation is 0.62 nm. The period of the reconstruction is larger than that observed on Au(111) vicinal surfaces with smaller miscut angles[251]: 6.3 nm, 7 nm, 7.2 nm, 8.0 nm respectively for the Au(111), (11,12,12), (788) and (677) surfaces. This reveals that steps, and at some points kinks, give additional possibilities to the surface to relieve the surface stress[264,265] and therefore the periodicity increases.

e. Growth of Co on the kinked Au(677) surface studied by GISAXS The GISAXS study of the Co growth has been performed in real-time. A qualitative understanding of the evolution of the intensity as a function of time gives some insight into the growth process. Initially the intensity decreases on the $(10L)$ scattering rod (step network) and increases on the $(01L)$ scattering rod (kink network). Only interference effects between the waves scattered by the surface and the Co nanostructures can explain these effects: the waves scattered by the Co nanostructures interfere destructively with that scattered by the steps and constructively with that scattered by the kinks. Therefore the Co nanostructures grow at the step edges and in between two kinks which is in agreement with STM images of the growth of Co on Au(788)[266]. To extract more information on the Co growth, the interference effects have to be interpreted more precisely. A statistical model of the surface topography and the Co dots has been developed to simulate the GISAXS patterns. However, the previous model, developed for the bare surface, cannot be applied for supported Co nanostructures in a straightforward way. The basic idea is to use another elementary object. One can use a semi-infinite parallelepiped with a Co dot on top at a given position but considering no size distribution (fixed kink size, fixed step height and fixed Co nanostructure shape and size). That way the surface is entirely built considering this elementary object and two main directions for the periodicity. The intensity reads :

$$\begin{aligned} I(q_x,q_y,q_z) &= \left|\frac{-4i}{q_xq_yq_z}\sin(q_zh/2)\sin(q_xk/2)+F_{\mathrm{Co}}(q_x,q_y,q_z)e^{i(q_xV-q_yU)}\right|^2 \\ &\times \mathrm{Re}\left\{\frac{(1+e^{iq_xk}\widetilde{P}_{S_1}(q_y))}{(1-e^{iq_xk}\widetilde{P}_{S_1}(q_y))}\right\}\mathrm{Re}\left\{\frac{1+e^{iq_zh}\widetilde{P}_T(q_x)\widetilde{P}_{S_2}(q_y)}{1-e^{iq_zh}\widetilde{P}_T(q_x)\widetilde{P}_{S_2}(q_y)}\right\} \end{aligned} \tag{5.6}$$

where F_{Co} is the shape factor of the Co dots and U and V are their relative positions from the kink site respectively along the (Oy) and (Ox) directions (Fig. 55). The Co dots are modeled as cylinders with an elliptic base and a fixed height (two monolayers) (Fig. 55). The shape factor of the Co dots is :

$$F_{\mathrm{Co}}(q_x,q_y,q_z)=2\pi DLH\frac{J_1\left(\sqrt{(q_xD/2)^2+(q_yL/2)^2}\right)}{\sqrt{(q_xD/2)^2+(q_yL/2)^2}}\frac{\sin(q_zH/2)}{q_zH/2}, \tag{5.7}$$

where J_1 is the Bessel function of first order.

The results of the fits show a good agreement between the simulated GISAXS patterns and the experimental ones (Fig. 56). The morphological parameters of the Co dots can be estimated as well as their position with respect to the kink sites (Table III).

The results are also in agreement with the STM data obtained on Co / Au(788) [251]. They show that the Co nanostructures grow first at the step edges and come into the upper terrace. They are all the more anisotropic than the amount of Co deposited on the surface is large[267].

f. Conclusion To be able to characterize by GISAXS the self-organized growth of Co dots on the kinked vicinal Au(677) surface, it is first mandatory to describe precisely the bare surface in order to take into account the interference between the waves scattered by the surface topography and by the Co dots. For that sake, a 3D model of the surface topography has been developed and a tomographic measurement of the intensity in the reciprocal space has been

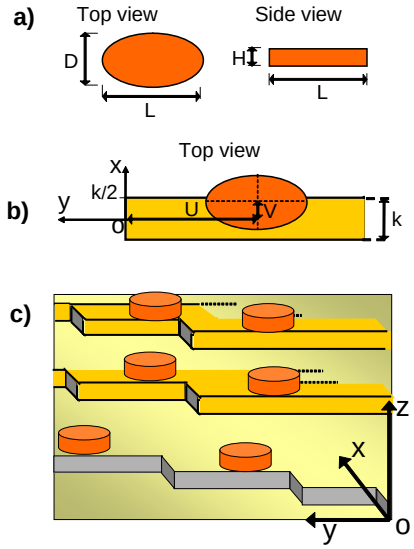

FIG. 55: a) Co nanostructures are modeled with cylinders with an elliptic base to take into account their shape anisotropy. Their height is fixed at 2 ML. b) The elementary object is built as the superposition of a semi-infinite parallelepiped and a Co dot on top which position can be adjusted. c) The spatial organization is modeled by an ideal 2D paracrystal. The main directions are the step edge and perpendicular to the steps (from Ref.[240]).

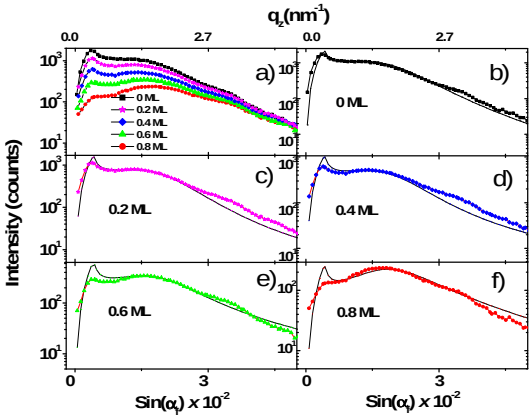

FIG. 56: Experimental data and fit of the (10ℓ) scattering rods from the steps array during the growth of Co ($\omega = 0°$). The incident beam is aligned parallel to the mean step edge direction. a) Time evolution of the scattering rods intensity integrated parallel to the surface plane. b) to f). Experimental data (○) and fit (solid line) for different amounts of Co. From Ref.[240].

Deposit (ML)	D (nm)	L (nm)	H (nm)	U (nm)	V (nm)
0.2	1.2	1.2	0.4	4.02	0.25
0.4	1.4	2	0.4	4.02	0.35
0.6	1.6	2.7	0.4	4.02	0.4
0.8	1.7	3.3	0.4	4.02	0.45

TABLE III: Morphological parameters of the Co nanostructures deduced from the fit. H has been fixed at 0.4 nm (2 ML height) and U at 4.02 nm (*i.e.* the Co nanostructures are in between the kinks).

performed. The parameters deduced from the quantitative analysis of the GISAXS images are in agreement with the STM data. The long-range order of the kinks is revealed and assigned to their interaction with the surface

reconstruction. They are trapped inside the *fcc* stacking areas of the surface, *i.e.* in between the stacking fault lines.

3. Self-organized growth of Co on a misfit dislocation network Ag/MgO(001)[1]

The self-organized growth of nanostructures on a dislocation network rely on two principles: (i) dislocation networks are well ordered: the dislocation density is fixed by the energetic gain of the plastic relaxation and the cost of their creation and interaction. As the interaction is repulsive and long-range a preferential distance separating the dislocations minimizes the interaction energy. (ii) The strain field induced by the dislocations modifies the local environment of the surface atoms[206] and favors a nucleation on specific sites. Dislocation networks have been used successfully for ordered the growth of different systems such as Co, Ni or Fe nanostructures[52,236]. Fe (resp. Ag) nanostructures have also been grown on a dislocation network made of a bilayer of Cu (resp. a monolayer of Ag) on Pt(111)[239]. However these approaches need the use of expensive single crystals of Au(111) or Pt(111) and only nanostructures of a few atomic layers high have been obtained[52].

An alternative approach[268] has been proposed, in which the strain field created by buried interfacial dislocations and propagating into a film of several nanometer of thickness results in a surface with a nanostructuration suitable for the successive growth of ordered self-assembled nanoparticles. This approach has been applied in the case of the self-organized growth of Co dots on a thin film of Ag [1]. This couple of materials has been chosen because the growth of Co on Ag is three-dimensional and no alloying is expected at RT[269]. To modulate the surface strain field the thin film of Ag is grown in cube-on-cube epitaxy on a MgO(001) single crystal[9,270]. As the lattice parameter mismatch is 3% between both materials the interface exhibits a coincidence site lattice of about 10 nm period that relaxes in a misfit dislocation network[9,13]. To succeed in the self-organized growth of nanostructures, the thickness of the film must be small enough, *i.e.* smaller than the period of the dislocation network as theoretically predicted by isotropic and linear elasticity[268]. However the thinner the film, the larger is the stored elastic energy and the dislocation network may collapse. Therefore the thickness must be intermediate between the period of the dislocation network and the critical thickness for plastic relaxation[271]. We have developed a complex *in situ* procedure to obtain well ordered dislocated films of the appropriate thickness. It consisted in growing a 100-nm thick Ag films which was first annealed to order the interfacial dislocation network, and next thinned down to 5 nm by ion bombardment at a temperature such that thinning was down by a step retraction process, while following the flatness of the film and the speed of thinning by anti-Bragg X-ray scattering, and controlling the thickness with X-ray reflectivity. When attempting to thin the film further, it was found to crack.

For this system we have used the GISAXS technique to study the growth of Co nanostructures as well as buried dislocation network at the Ag/MgO interface thanks to the electronic density contrast induced by the dislocations[77,272].

a. The misfit dislocation network of the Ag/MgO(001) interface Fig. 57-a and b show two GISAXS images measured on a thin film of Ag on MgO(001) with an incident X-ray beam respectively parallel to the $\langle 110 \rangle$ and $\langle 100 \rangle$ crystallographic directions of MgO(001). Narrow scattering rods in the $q_{\parallel}$ direction reveal a periodic nanopatterning in the surface plane. The extension of the intensity perpendicular to the surface (q_z) is a signature of the in-depth profile of the strain field perpendicular to the surface. The large terrace size deduced from the GIXD measurements at anti-Bragg conditions proves that the signal does not arise from surface roughness but from buried layers. The position of the scattering rods gives a period L of 10.95 nm. The fourfold symmetry, the orientation as well as the lattice parameter of the super-lattice is in agreement with that of a square dislocation network oriented along the $\langle 110 \rangle$ directions with a Burger vector $\mathbf{b} = \frac{1}{2}[110]$[13]. Therefore the Ag atoms are in coincidence with those of Mg (or O) every $\Lambda = 37$ atoms. The lattice parameter of Ag deduced from the position of the Bragg peaks shows that 90% of the interfacial stress is relieved by the dislocations, which highlights the stability of the Ag film at such a small thickness. The remaining 10% stress is relaxed by a homogeneous strain field. The linear increase of the FWHM of the scattering rods in $q_{\parallel}$ can be assigned to a cumulative disorder effect of the distance separating the dislocations. From the 1D-paracrystal model[79], the standard deviation σ, of the distance between two neighbor dislocations can be evaluated from the FWHM of the first order scattering rods: $\sigma = L\Delta q_{\parallel}/q_{\parallel} = 0.6$ nm. A quantitative study of the dislocation network was achieved by the analysis of its first order ($\frac{1}{\Lambda}\frac{1}{\Lambda}L$) and second order ($\frac{2}{\Lambda}0L$) scattering rods. We refer to Ref. [25] for the detailed calculation, which is summarized here only qualitatively. Due to the order quality of the network, the scattering rods are the Fourier components (modulus square) in the surface plane of the dilatation field. The linear isotropic elasticity theory predicts that the dilatation field decomposes into Fourier series in each material (layer and substrate, respectively), each $\mathbf{q}_{\parallel}-$component being exponentially damped from the interface (toward the thin film or toward the substrate, respectively), with and attenuation length $\lambda(\mathbf{q}_{\parallel})$. The elastic constants of each materials are taken into account in the Fourier coefficients. Rigorously, the strain field reflected by the surface (and not the interface)[273]) should also be considered, with an exponential decrease from the surface inside the thin film. This term has been dropped out because theoretically its amplitude is negligible for a 5 nm thick film.

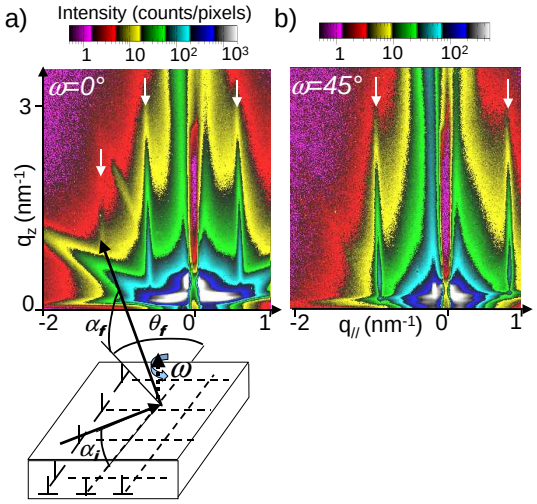

FIG. 57: a) Sketch of the experiment and GISAXS images obtained for an incident X-ray beam oriented parallel to the $\langle 110 \rangle$ direction, *i.e.* at $\omega = 0°$ (logarithmic intensity scale). $q_{\parallel}$ coordinate (resp. q_z) ranges from -1 to 2 nm^{-1} (resp. 0 to 3.26 nm^{-1}). Scattering rods of the dislocation network are indicated by arrows (1^{st} and 2^{nd} orders). Ag(111) facets give rise to a broad scattering rod at 54° with respect to the normal to the surface. b) same as a) with an incident beam parallel to the $\langle 100 \rangle$ direction of MgO(001), *i.e.* at $\omega = 45°$. Adapted from Ref.[240].

The GISAXS calculation of the intensity scattered by the dislocation network was fully treated in the framework of DWBA, the unperturbed system being an homogeneous thin film over the substrate without dislocation network. The amplitude scattered by the dislocation network was found to be the coherent sum of five terms (four arising from the film and one from the substrate). In addition to the scale factor, the only free parameter is the penetration depth $\lambda(\mathbf{q}_{\parallel})$ of each mode of the dilatation field. To extract $\lambda(\mathbf{q}_{\parallel})$, the intensity of the measured scattering rods $(\frac{1}{\Lambda}\frac{1}{\Lambda}L)$ and $(\frac{2}{\Lambda}0L)$ have been fitted. The best fit (Fig. 58) has been obtained for $\lambda = 1.05$ nm for each scattering rods, which has to be compared to the theoretical ones : $\lambda_{(\frac{1}{\Lambda}\frac{1}{\Lambda}L)} = 1.74$ nm and $\lambda_{(\frac{2}{\Lambda}0L)} = 1.23$ nm[273]. A more rigorous analysis should be done in the framework of the anisotropic elasticity theory, which would probably give a better agreement.

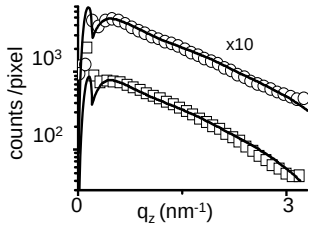

FIG. 58: Cross section in q_z of the scattering rods of the dislocation network. (□) Experimental data for the $(\frac{1}{\Lambda}\frac{1}{\Lambda}L)$ scattering rod. (○) Experimental data for the $(\frac{2}{\Lambda}0L)$ scattering rod, (×10). Fit (full lines). From Ref.[240].

b. The self-organized growth of Co nanostructures on Ag/MgO(001) The growth of Co on the Ag thin film has been studied in real-time with the X-ray beam parallel to the $\langle 110 \rangle$ crystallographic direction. From the very beginning of the growth process (0.2 ML), the subtraction of the intensity measured after and before the deposition of Co shows oscillations along the scattering rods of the dislocation network (Fig. 59). The amplitude of the oscillations increases with time, reaches a maximum for 0.95 ML of Co deposited, and then decreases (Fig. 60). The period of the oscillations gives a height of 5 nm, in agreement with the thickness of the thin film measured by X-ray Reflectivity. The main result is that these oscillations prove that the growth of the Co nanostructures is well ordered. Indeed interference effects can only occur if the phase shift between the waves scattered by the nanostructures and those scattered by the dislocations is well defined *i.e.* if the position of the Co nanostructures is correlated to the dislocations. The measured intensity is thus the sum of three terms : one comes from the dislocation network, one comes from the Co nanostructures and one comes from the interference term between both waves:

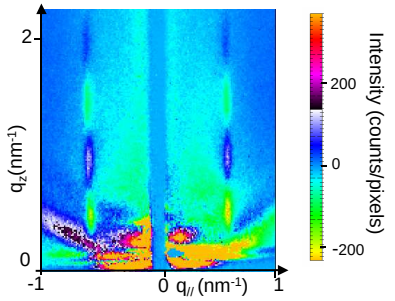

FIG. 59: Experimental image of the interference term (subtracting two GISAXS images: after (0.8 ML) and before Co deposit). The incident beam is parallel to the ⟨110⟩ direction. The intensity scale is linear. The $q_{\|}$ (resp. q_z) coordinate ranges from -1 to 1 nm^{-1} (resp. 0 to 2.24 nm^{-1}). Adapted from Ref.[240].

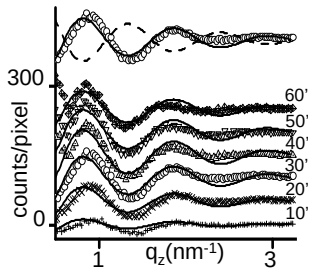

FIG. 60: Intensity of the interference term as a function of q_z for different amounts of Co deposited on the surface. The best fits have been obtained considering that the Co dots are upon the dislocation cores. A vertical translation proportional to the time has been introduced for clarity. Last curve (top) for 0.8 ML of Co. It has been added to the experimental data (○) the best fit (full line), and a simulation in case the Co dot is in between the cores of the dislocations (dotted line). The interference is in phase opposition (from Ref.[240]).

$$I = |\mathcal{F}_{DN}|^2 + |\mathcal{F}_{\mathrm{Co}}|^2 + 2\mathcal{F}_{DN}\mathcal{F}_{\mathrm{Co}}\cos(\mathbf{q}_{\|}\mathbf{d}_{\|} + q_z d_z), \tag{5.8}$$

where $\mathcal{F}_{DN}$ (resp. $\mathcal{F}_{\mathrm{Co}}$) is the form factor of the dislocations (resp. Co nanostructures); $\mathbf{d}_{\|}$ are d_z are the parallel and perpendicular coordinates of the Co nanostructures with respect to the crossing point of the dislocations. As the Co nanostructures are small ($|\mathcal{F}_{\mathrm{Co}}| \ll |\mathcal{F}_{DN}|$), the $|\mathcal{F}_{\mathrm{Co}}|^2$ term is negligible in Eq. 5.8. The interference term which contains the information on the position of the nanostructures is obtained by subtracting the GISAXS data after and before Co deposition. Two high symmetry sites are possible for the localization of the Co dots: above the crossing point of the dislocation lines or at the center of the square formed by four dislocation lines. By symmetry any other possibility gives more than one nanostructure per unit cell. This is not expected because there is one nucleation site per unit cell and the diffusion length of Co atoms is large at the chosen temperature to avoid any homogeneous nucleation.

To obtain the position of the Co nanostructures, it was necessary to describe precisely the interference effect along the scattering rods. Since the form factor of the dislocation network has been previously determined, only the form factor of the Co nanostructures and the position in the unit cell is lacking. The quantitative analysis of the interference effect has been performed again in the framework of the DWBA tacking into account the Ag thin film which modifies the reflection properties of the surface. To calculate the interference between the waves scattered by the nanostructures and the dislocations (equation 5.8) nine terms have been calculated (respectively four and five for the nanostructures and the dislocations). To give an explicit expression of the calculation, the Co dots were modeled with a cylindrical shape with an integer number of atomic planes in the height. The best fit has been obtained for Co dots localized above the dislocation crossing lines, ($\mathbf{d}_{\|} = \mathbf{0}$), *i.e.* in compressive sites and of 2 ML-height (see Fig. 60).

c. Conclusion In conclusion, the self-organized growth of Co nanostructures above a square misfit dislocation network of Ag/MgO(001) demonstrated by *in situ* GISAXS. Contrary to the most common idea, small angle scattering techniques such as GISAXS are sensitive to strain as evidenced here in the case of a buried dislocation network. A comparison between the linear and isotropic theory of elasticity and the experimental data confirms that the strain field is exponentially damped from the interface into the film and the substrate.

4. Self-organized growth of Ni clusters on a cobalt-oxide thin film induced by a buried misfit dislocation network

The idea demonstrated above of self-organized growth thanks to a buried misfit dislocation network has been transposed to order metallic nanoparticles on an oxide substrate, which is especially important in view of their potential magnetic or catalytic properties, which strongly depend on their exact size and shape. A 5 nm-thick CoO(001) think film was *in situ* grown on a Ag(001) substrate. Due to the 3.25% lattice mismatch, a square network of dislocations was formed at the CoO/Ag(001) interface. This was again fully characterized by *in situ* GISAXS, XRR and GIXD, and used to influencing the growth of a Ni overlayer developing a spatially ordered distribution of clusters.

Ni was next evaporated at room temperature on the CoO(001) surface from a Knudsen cell with a very low evaporation rate of 0.005 nm/min. The structure of the CoO film deposited on the Ag(001) surface was first investigated by GIXRD, evidencing a well ordered square misfit dislocation network into the CoO film of 23 ML thickness, of period $\Lambda = 0.2979/0.0325 = 9.2$ nm. At variance with the MgO(001)/Ag(001) interface[1,13], dislocations are of pure edge type, of 1/2110 Burger's vectors, with lines along the $\langle 110 \rangle$ directions.

The influence of a dislocation network in the CoO film on the successive growth of a nickel overlayer has been investigated by GISAXS and STM. STM showed that the surface had large flat areas uniformly covered by small round Ni clusters. *In situ* GISAXS reveals the organization of the Ni clusters, and, by analogy with the Co/Ag/Mgo(001) case, allowed determining the relationships between the locations of the interfacial dislocations and the Ni cluster nucleation centers[1]. Fig. 61-a shows a GISAXS intensity map measured with the incident X-ray beam parallel to the $\langle 110 \rangle$ crystalline axis before the Ni deposit. Fig. 61-b shows the same GISAXS image after the deposition of about

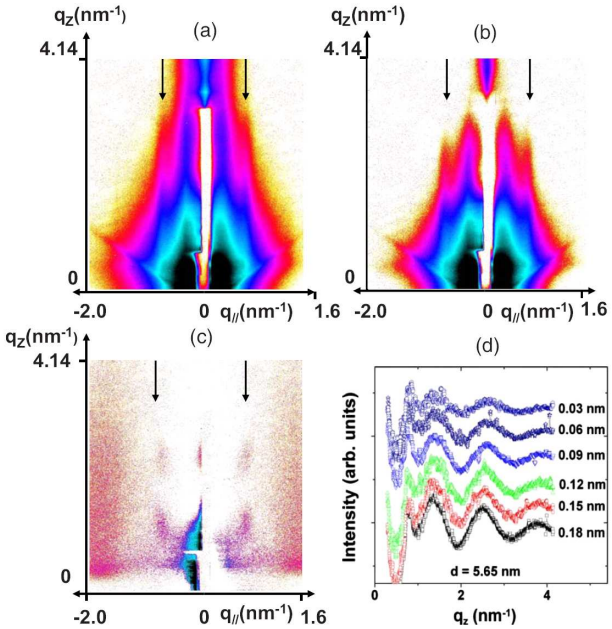

FIG. 61: GISAXS image of 25 ML CoO/Ag(001) recorded with the incident beam parallel to the [110] direction. b) Same image of panel a) after the deposition of 0.18 nm of Ni. c) Difference between panel a) and b). d) Sections of panel c) along the arrows for different Ni coverages. From Ref.[241].

0.18 nm of Ni, and Fig. 61-c shows the difference between the two above images. The intensity of the two scattering rods in the perpendicular direction clearly shows periodic oscillations, as in the abice case. These measurements thus demonstrate that the ordering of the Ni clusters is driven by the presence of the buried dislocation network at the CoO/Ag(001) interface. These findings are of a great relevance because the formation of interfacial dislocations is a common strain relief mechanism in oxide/metal interfaces[274–276]; it could thus become a useful route to realize the organized growth of metallic nanoparticles on oxide thin films.

In conclusion this study has shown that a square interfacial misfit dislocation network can be formed at the interface between a CoO film and a Ag(001) surface. The periodic displacement field of this network extends up to the CoO(001) surface, providing a network of sites for preferential nucleation and growth of metallic nanoparticles. This self-organized growth is achieved at room temperature instead of the more common low temperatures, which shows that the dislocation-induced nucleation sites are strongly energetically favorable. This however needs a

very low deposition rate for which the diffusion length of the Ni atoms on the oxide surface is of the order of the nanostructuration period. The resulting ordered Ni nanoparticles have a narrow size distribution, which is essential to keep well defined properties over an assembly of nanoparticles. The achievement of the control of the self-assembling process of metal cluster on the surface of a 5 nm thick oxide film represents a step forward in the production of real devices by self-organized growth. Moreover this experiment reveals the great potentiality of the GISAXS technique in the study of the self assembled structures being able to probe, in a non destructive way, the surface and the buried part of a thin film.

VI. CONCLUSION ON *IN SITU* GISAXS

The aim of this report was to review the state-of-the-art of the Grazing Incidence Small-Angle X-Ray Scattering (GISAXS) technique, both from the experimental and theoretical points of view. This technique is now mature and well established to characterize the morphology of all kinds of nanoscopic or mesoscopic materials, providing detailed information on the nanoparticle shapes, sizes, distributions of sizes, faceting, spatial correlations, in a statistical way, averaged over millions of particles. The probed length-scales vary between 1 nm and several μm. In addition, GISAXS is intrinsically extremely sensitive to the ordering of the nanoparticles at short-range, long-range or in between. When used *in situ* during growth, it can thus be helpful to adjust the growth conditions and find the optimal parameters for self-organization. GISAXS starts to be a widespread technique in soft-condensed and hard-condensed matter studies, to analyze nanoparticles on surfaces or buried below a surface, as well as multilayers of particles, whether they are ordered or not. This possibility to investigate buried nanoparticles in a non destructive way makes GISAXS an unique tool. One of the main drawback of the technique is that it most often requires synchrotron radiation, which means that a limited amount of time is devoted to a particular study, so that all pertinent parameters (such as for instance substrate temperature or defect density) can not be systematically varied. The understanding of the information contained in GISAXS patterns is now quite complete and analysis softwares are available. However the underlying theories are complex, not only because of the refraction effects, but also because of the difficulty to described the particle-particle correlations, especially when they depend on the particle types or sizes. In most cases, a correct quantitative analysis needs very accurate data, extending far in reciprocal space, which requires a background as low as possible, minimum distortions, and a very precise knowledge of the angles, especially the incident and emergent angles (to within better than 0.01°). Hence, although a GISAXS experiment is in principle extremely simple, great care must be taken in practice to perfectly define the incoming beam, which should have a small size perpendicular to the sample (typically a few tens of μm), and a small and well-defined divergence (typically smaller than 0.01°), to perfectly orientate the sample, and, most importantly, to cut any source of background, such as those induced by slits or windows in the beam path.

To assert the accuracy of the technique, many studies compared the morphological characteristics deduced by accurate GISAXS analysis to those obtained by other techniques such as AFM, STM or TEM, with in general a good agreement, thus demonstrating the high accuracy of a complete quantitative GISAXS analysis, which has the advantages of probing a large sample area, in a non destructive way. If only the average morphological parameters are required, with a limited accuracy, then much simpler and faster analysis of the GISAXS data can be performed, using for instance the asymptotic behaviors (classically known as Porod and Guinier analysis). If the size distribution is not too large, a rough modeling can provide the average size and separation to within $\pm$20%, as well as other average parameters, such as *e.g.* the facets size, by analyzing the width of the corresponding scattering streaks. However, accurate analysis of GISAXS patterns can become tedious when facing problems of accounting cross correlations between parameters and statistical description of the morphology. This difficulty is intrinsic to the description of diffuse scattering. In the future, it could be overcome by Reverse Monte Carlo or Maximum Entropy fitting algorithms for finding configurations which are the most compatible with the information brought by a given pattern. However, to our knowledge, these procedures have been applied only to radial distribution function obtained from scattering by amorphous materials[277] and not yet to small angle scattering from particle systems.

Although this report dealt only with the GISAXS technique, which probes the scattering only at small angles (or small momentum transfer), and thus nanometer-size objects, the technique can very easily be combined with X-ray reflectivity to characterize the order perpendicular to the surface, and with Grazing Incidence X-Ray Scattering to probe the atomic structure (lattice parameter, strain, composition...) of the nanostructures. This is an ongoing trend during synchrotron experiments. The results of the GISAXS analysis (size, shape, size distribution, particle-particle correlation, ordering....), can be useful to unfold several contributions such as strain or crystalline defects which arise at wide angles. In addition, all three techniques can gain a lot, by using anomalous scattering (when possible) to

have a chemical sensitivity in a multi-component system. This could be used for instance to discriminate between the GISAXS signal arising from the matrix (or substrate)and that arising from nanostructures, as shown in the Co/Au(111) case, or to unravel the internal morphology of multicomponent nanostructures such as *e.g.* core-shell clusters. Anomalous scattering may also be used to normalize the intensity or to subtract the substrate roughness contribution from the scattering of the sample. Hence, one important development of the technique is believed to be this coupling between GISAXS and anomalous scattering.
Note in passing that performing GISAXS on an absolute scale, *i.e.* deducing the exact amount of matter giving rise to GISAXS, is possible if the incident beam is made small enough so that all the beam hits the sample, and if the incoming flux is quantitatively measured. The GISAXS intensity can then be expressed in electron units (*i.e.* in multiple of the scattering cross section of one electron).

One of the most interesting strength of the technique (like most X-ray based techniques) is its ability to perform *in situ* experiments, with many possible sample environments (UHV chamber, liquid throats, high pressure cells, catalytic reactors, electrochemical cells, straining systems ...), thus allowing to characterize *in situ*, and sometimes in real time the effects of controlled parameters (temperature, deposition rate, pressure, applied stress, exposure to different gases, application of an electric field, magnetic field ....) on the morphology of the sample. In addition, it is possible to simultaneously measure other physical properties by other techniques, mainly involving light (Raman, UV-visible reflectivity, second-harmonic generation ...). This advantage will be certainly used in the near future to design new instruments not only optimized for GISAXS measurements, but also for complementary tools.

Two drawbacks of the approaches described in this report ought to be discussed and lead to future perspectives for the application of novel X-ray techniques that can only be exploited at current 3^{rd} generation synchrotrons and/or future free electron based X-ray sources. One drawback is that in all examples described above, real space model assumptions for the nanoparticles are needed to fit the pattern; this is due to the well know "phase problem" inherent to all X-ray scattering measurements, which does not allow for a direct reconstruction of the morphology from the measured intensity distribution in reciprocal space. The other drawback is that the information obtained is based on measurements on large nanoparticle ensembles, thus measuring their mean morphology rather than the variation of individual morphological properties. The knowledge on the variation of properties is especially important for nanoparticles grown by self-organization, where differences from one island to another are expected. Recently, two major technical improvement of third generation synchrotrons have allowed new kinds of GISAXS measurements, by offering beams with partial coherence and by focusing X-rays to submicron dimensions. The focusing of hard X-rays reached beam sizes in the 100 nm range and below. The use of (incoherent) micro-beams, allows for instance to scan an inhomogeneous sample, yielding GISAXS images characteristic of (sub)micron-size areas of the sample. The use of a small coherent X-ray beam set to image one particle yields an image from which the complete sample shape and size can in principle be deduced without assumption, thus solving the "phase problem".

The future developments of the GISAXS technique will almost certainly be driven by the increase of brilliance of the next generation synchrotron sources, and by the advent of the free electron lasers. This will provide more intense beam, more coherent, with a smaller size and a smaller divergence, allowing for the development of coherent GISAXS, as well as dynamic studies at a much smaller timescale than presently possible. The combination of both will allow also to follow the evolution of speckles with time[278,279] (X-ray Coherent Spectroscopy), thus yielding important information on the different characteristic times in a system under evolution. Last but not least, new two-dimensional detectors, for instance based on the hybrid pixel technology, are being available, with a much smaller background, much larger dynamics and faster response. This should allow, among others, to measure both the specular and diffuse scattering at once.

VII. PROJECT OF IN SITU X-RAY STUDIES OF THE GROWTH OF IV-IV SEMICONDUCTORS BY PHYSICAL AND CHEMICAL BEAM EPITAXY

A. Introduction

In the present section, devoted to perspectives, our project of coupling diverse x-ray scattering techniques (GISAXS, GIXD, GIXS, SXRD, XRR) to study *in situ* the growth of IV-IV semiconductors is briefly presented. We have already started such studies on Ge and Si islands grown by physical evaporation, and some of the results are very briefly highlighted in the second section. However, our goal is to go beyond simple islands, and to study the processes leading to the growth of semiconductor nanowires (NWs). This requires the implementation of the growth of Si and Ge by chemical beam epitaxy (CBE, also called UHV-Chemical Vapor deposition, UHV-CVD). The first section is

devoted to an introduction to the field of semiconductor nanowires, to the Vapor-Liquid-Solid growth process of NWs and to UHV-CVD. A third section briefly discusses how the growth of NWs could be investigated with X-rays.

B. An introduction to nanowires, the vapor-liquid-solid growth and UHV chemical vapor deposition

1. Introduction

Nanowires are defined as very elongated objects (up to several μm in length) having a lateral size smaller than typically 100 nm. Such low-dimensional nanostructures are not only interesting for fundamental research due to their unique structural and physical properties relative to their bulk counterparts, but also offer fascinating potential for future technological applications. Deeper understanding and sufficient control of the growth of NWs are central to the current research interest, hence the synthesis of semiconductor (SC) nanowires has been studied intensively worldwide for a wide spectrum of materials. The most widely used growth process is by far the vapor-liquid-solid process. Strategies for position-controlled and nano-patterned growth of NW arrays are also essential to control the spatial positioning and size of NWs.

2. A few words on the interest of semiconductor nanowires

Many of the new properties of NWs are the result of strong photon, phonon and electron quantum-confinement due to their small radial size. NWs might have *e.g.* unique size-dependent mechanical properties, increased luminescence efficiency, reduced threshold for laser operation, enhanced electromechanical response and enhanced thermoelectric efficiency (especially with Si NWs[280]). SC NWs are thus attractive building blocks for bottom-up nanotechnology including optoelectronics[281,282] and manipulation of isolated electron spins[283–285]. A few devices based on SC NWs have already been demonstrated[286,287].

There has been much interest paid to the optical properties of SC NWs, because of their promising prospects as building blocks for nanoscale optoelectronic detectors (with Si NWs[288]), light-emitting diodes (LEDs), lasers, optical waveguides, and non-linear optical frequency converters. In particular, the integration of light sources with complementary metal-oxide semiconductor (CMOS) devices would be a revolution in information technology. NWs have been used to develop nanolasers[289] of different wavelengths covering from UV all the way to IR according to the semiconductors used[290]. III-V SC nanowires are more and more developed to realize nano LEDs. Multicolor LEDs have been fabricated on a single substrate by contacting different n-type NWs, including GaN(UV), CdS(green) and CdSe(near-infrared) with Si NWs as a common p-type material, enabling easy interfacing with conventional silicon microelectronics.

An emerging area of great interest is the interfacing of SC nanowires with living cells, as transistors and subwavelenth optical waveguides. NWs have a size scale that overlaps with fundamental building blocks of cells, making them particularly suitable for biological and medical applications (neural network on a chip; cellular force measurements using NW arrays; hollow nanowires used as nano-needles for injection in cells; NW-based biosensors; NW-base electrodes for neural interfaces). Their high sensitivity and selectivity for detecting biological or chemical species might offer the possibility to detect the selected attachment of single molecules.

Several possibilities exist for the use of NWs in the energy sector (energy saving, harvesting and storage). In particular, SC NWs have been proposed to be fundamentally advantageous for photovoltaic applications due to some unique properties. Silicon p-i-n NW solar cells have been developed[291,292]. Nanogenerator based ZnO NWs have been developed to power battery-free wireless nanodevices by converting ambient vibrations, hydraulic energy, or mechanical movement to electricity. These devices demonstrate the capability of harvesting energy from ambient vibrations in different media[293]. Ge/Si NW can also be used to make devices; an example being the field-effect transistor (FET)[294]. Silicon NWs have also been shown recently to be good thermoelectrics.

Future possible applications of NWs are very diverse[287]. One may cite as potential emerging applications: integrated nanophotonis, NW-based single cell endoscopy or NWs for direct solar to fuel conversion. In addition, interest in NWs continues to grow because they hold the promise of monolithic integration of high- performance semiconductors with new functionalities into existing silicon technology[295], and of developing nanoelectronics from the bottom up[296].

3. Types of NW: axial, radial and substrate/NW heterostructures

Formation of heterostructures is at the core of NW technology and novel device structures. Three major categories can be identified: axial, radial, and substrate/nanowire heterostructures. Axial heterostructures can be formed by

alternating the growth precursors, resulting in a composition variation along the wires. NWs represent and ideal morphology for the growth of axial heterostructures, since mismatched materials can be grown epitaxially on each other without misfit dislocations, thanks to strain relief by coherent expansion of the lattice outwards, along the wire diameter. Nanowire heterostructures superlattices have been demonstrated for a variety of material systems, with lattice mismatch as high as 3 percent[281]. Much recent work has focused on attaining sharp heterointerfaces for various materials. Radial structures, also known as core-shell structures[297], can be grown by first growing NWs by conventional particle-assisted growth, then changing the parameters so that bulk growth is favored[298]. The unique one-dimensionality inherent to NWs has already solved some of the long-standing technical problems that have plagued the thin film community. For example; integration of optically active semiconductors (*e.g.* III-V's) onto silicon (the so-called substrate/NW heterostructures[299]) is critical for the next generation of computing tools that will merge photonics with electronics on a single platform.

4. Methods to grow NWs: the Vapor-Liquid-Solid growth process

Nanowires can be grown by a variety of methods, but the most common method by far is the particle-assisted growth ([299,300] called Vapor-Liquid-Solid (VLS). This technique, by Wagner and Ellis in 1964[301], uses metal seed particles, most often gold, which act as nucleation center [302] and direct the growth. The size, number and position of the resulting nanowires are determined by the seed particle, potentially allowing for a high degree of control over final structures. The VLS growth can be divided into two main stages: (i) the formation of a small liquid droplet, and (ii) the alloying, nucleation and growth of a NW (see Fig.62-A). First, small metal clusters are formed on a surface. Next, a gas containing the growth material is directed toward the surface. As the surface of the liquid droplet has a much larger sticking coefficient than the solid substrate, the precursor atoms prefer to deposit on the liquid surface and form an alloy. Continued incorporation of precursor atoms into the liquid droplet leads to a super-saturation of the semiconductor component. As a consequence, crystal growth occurs at the solid-liquid interface by precipitation and NW growth starts. The growth rate depends on the droplet size as well as on the super-saturation, which is influenced by the concentration of the precursor vapor and the substrate temperature. The droplet in most cases remains at the tip of the NW during growth. A direct observation of the VLS growth of Ge NWs was reported by Wu and Yang[303], who identified the various growth stages in correlation with the AuGe binary phase diagram (Fig. 62-B). Ge and Au form liquid alloys when the temperature is raised above the eutectic point (361°C). Once the liquid alloy droplet is supersaturated with Ge, NW growth will start to occur at the solid-liquid interface[304]. Similar observations of VLS growth of Si NWs by using ultra-high-vacuum transmission electron microscopy (UHV-TEM) have been reported by Ross et al.[305,306] and Sutter et al.[307]. The VLS method has become the most widely used method for generating 1D NWs from a rich variety of inorganic compounds materials that include elemental semiconductors (Si, Ge and B), III-V SC (GAn, GaAs, GaP, InP, InAs), II-VI semiconductors (ZnS, ZnSe, CdS, CdSe) and oxides (ZnO, MgO, SiO2). Gold is by far the most frequently used metal for the VLS process. However, the possible incorporation of Au in the SC[308] and the change of electrical properties due to Au contamination have led to the search for alternative catalysts, especially in view of the integration of NWs in microelectronics for which Au has to be avoided. For the growth of Si or Ge NWs, Ag, Cu, Pt, Fe, Ga, Ti and Al have been tested as alternative catalysts.

Despite many years of study, the VLS growth process remains under lively debate. In some cases, NW growth has been achieved while the catalyst was solid, well below the eutectic temperature, leading to the so-called Vapor-Solid-Solid (VSS) growth[306]. In addition, the role of the metal particle is unclear. For instance, contradictory results have been reported on the effect of particle size on NW growth rate. Also, NWs growth from a patterned array of catalysts has shown that small wire-to-wire spacing leads to materials competition and a reduction of growth rate. These uncertainties call for more detailed investigation of the state, structure, composition and morphology of the catalyst and the NW during growth, which is one of the aims of our project, as discussed in the last section.

5. Controlling position, arrangement and size of catalytic metal islands for organized nanowire growth.

Because in the VLS growth, the location and size of NWs are fully determined by the location and size of the metal catalysts, producing well ordered monodisperse arrangements of NWs, and hence NWs of well-defined properties, can be obtained thanks to a well-ordered, monodisperse assembly of catalysts, which itself can be obtained by deposition on a nanopatterned substrate, *i.e.* a substrate with a periodic arrangement of nucleation/growth sites with feature sizes and lattice constants below 100 nm. As high temperature in the range 500°C-1000°C are usually needed for the growth of SC NWs, the problem of the high mobility of the metals, which can destroy the predefined catalysts pattern, has to be solved. A number of patterning methods have been used by different groups, for the controlled

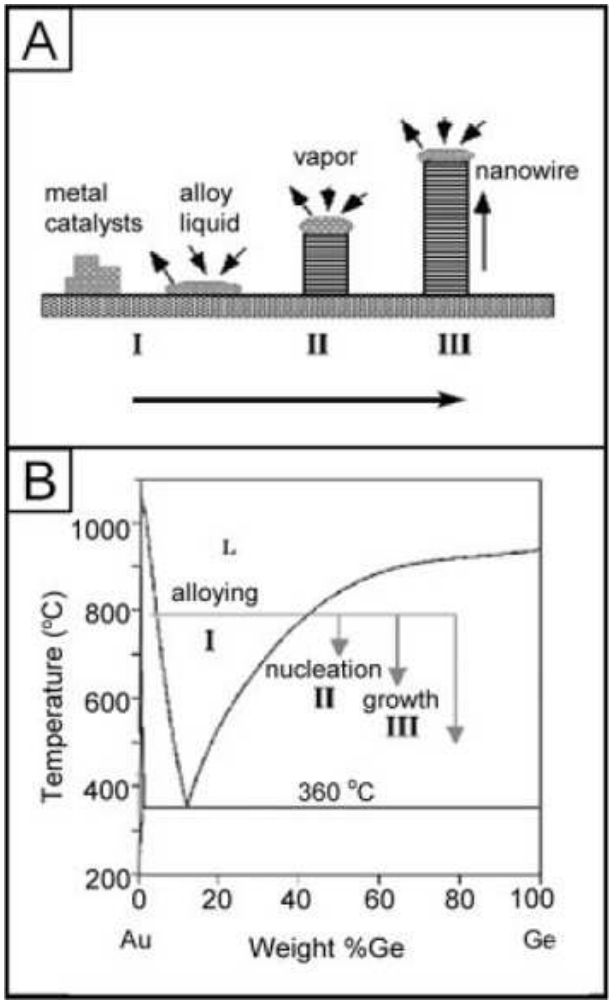

FIG. 62: A) Schematic illustration showing the growth of a nanowire via the vapor-liquid-solid mechanism. B) The binary phase diagram between Au and Ge, with an indication of the compositional zones responsible for alloying, nucleation and growth[303].

preparation of metal dots arrays on a substrate surface, including photo- or e-beam lithography[309], arrangement of Au nanocrystals from suspensions, nanosphere lithography, gold deposition masks based on porous alumina templates, nanoimprint lithography and block copolymers for nanolithography.

6. Ultra-High-Vacuum Chemical Vapor Deposition - UHV-CVD or Chemical Beam Epitaxy - CBE

The deposition methods of choice to grow nanowires is CVD or MOCVD because they provide compatibility with large area processing and are relatively low-cost compared with physical vapor deposition techniques like MBE. In addition, the selectivity of the catalyst site for the growth is much less good in MBE, for which a majority of the growth takes place on the substrate, outside the catalysts. Our objective of studying *in situ* the process of NW growth using X-rays thus naturally requires CVD. However, (MO)CVD is usually performed at quite elevated reactant pressures between mbar and a few 100 mbar, which results in very fast grow as well as incompatibility with UHV-chambers and MBE growth. We have chosen instead to implement a CVD injector on our existing MBE/UHV X-ray chamber, thus resorting to the so-called UHV-CVD or Chemical Beam Epitaxy (CBE). This low pressure (and lower temperature) growth regime has been developed by B.S. Meyerson at IBM in the 80's[310], and further implemented in a few groups in order to investigate it with different *in situ* tools in France[311], Germany[312] and again at IBM[305,313] in which it has been implemented *in situ* in an UHV-TEM. In CBE, typical gas reactant pressures lay between 10^{-9} mbar and 10^{-3} mbar.

C. *In situ* growth of semi-conductor nanostructures, from MBE and islands toward CBE and nanowires

1. Introduction

a. Growth of semiconductor nanostructures The research activities in the field of self-organized growth of nanostructures such as semiconductor quantum dots or nanowires have seen a steady growth over the last two decades. In the focus of interest are for instance new opto-electronic properties due to the carrier confinement[314–317]. We very briefly present below a few studies of nanostructures in the form of islands of different shapes grown by MBE following the Stranski-Krastanow (SK) growth mode[318]. This growth instability during hetero-epitaxial deposition of a few atomic layers leads to the formation of islands on top of an ultra thin film. The driving force of island formation is a decrease of the elastic energy. The exact influence of temperature and growth rate is still a subject of investigations, as kinetic effects are important for the island formation and are not yet understood in full detail. Indeed, the combination of growth kinetics and thermodynamics are responsible for surface instabilities as well as for size, composition and shape of self-organized nanostructures. Thus experimental methods that shed light on these dynamic processes are of crucial importance.

b. Ordered growth of nanostructures In order to exploit the unique electronic and optical properties of quantum dots or nanowires, not only an exact tuneability of the obtained size is of interest, but furthermore a narrow size distribution of ensembles is crucial. As all derived properties originating from the confinement depend sensibly on the exact size and shape, any ensemble broadening due to variations of these parameters makes a possible device useless. It is thus essential to focus on obtaining samples with narrow size distribution of nanostructures.

The possibilities of tuning the nanostructure sizes or to arrange islands in ordered patterns are limited so far. Therefore methods that can overcome these problems have attracted a lot of interest. In general, they rely on a periodic structuring of the substrate with periodicity in the nanometer range. First attempts have been published, using different methods of pre-patterning of silicon surfaces such as lithography[319,320] or twisted wafer bonding[321]. These fabrication methods represent combinations of the complementary methods often classified as top-down (*e.g.* lithographic patterning and subsequent reactive ion etching) and bottom-up (*e.g.* self-organized SK-growth of quantum dots on surfaces) approaches. The lithographic patterning of Si-surfaces followed by the MBE-growth of epitaxial heterostructures is compatible with the state-of-the-art procedures of preparing flat surfaces for epitaxial growth. It thus provides very clean conditions and the produced nanostructures show similar optical properties as the ones obtained by standard SK-growth on native Si(001) surfaces. These islands can be arranged in perfect two-dimensional periodic patterns and show a very high size and shape homogeneity[320]. The island density and, to a certain extent, also their sizes are limited by the lithographic resolution. For the pre-patterning by twisted wafer bonding, no fundamental size limit exists, but the produced surface pattern, based on an underlying dislocation network, does not resist to all thermal treatments that are generally required to clean Si-surfaces under ultra high vacuum. Thus at the moment, the preparation of these surfaces for epitaxial growth is mainly done by wet chemical processes[322].

As shown bellow, we have already applied both structuring methods and successfully prepared samples in the UHV chamber at BM32 on Si surfaces of (001) orientation. In both cases we grew ordered Ge-islands, following the morphological, structural and chemical properties during growth, and compare them to the case of growth on nominal surfaces. Naturally, as already discussed, any arrangement of metallic catalysts on these surfaces would yield an easy procedure to obtain very high density arrays of well organized, small and monodisperse nanowires. We thus intend to develop these patterning procedures for the (111) orientation of silicon, and study *in situ* the conditions to obtain an organized growth of metallic islands. The knowledge about the preparation of such patterned surfaces and in particular the recovery of a defect free Si surface will definitely present an important step for the organized growth of catalysts on such substrates.

c. The necessity of in situ techniques So far, experimental methods that follow the dynamics of the growth and extract quantitative parameters remain a challenge. For qualitative information, reflection of high-energy electron diffraction (RHEED) is standard equipment in MBE-systems. High sample temperatures do not affect its use however its quantitative information is limited. Scanning electron microscopy (SEM), using focused electron beams can also be used at high sample temperatures, but with limited time- and spatial resolution[323,324]. In the framework of the industrial research, a SEM study on various stages of the growth of Si nanowires has been published recently[308]. It describes the morphological evolution of nanowires and the Au-catalysts at different growth stages. This study prompted speculations about Au diffusion and the consumption of the catalyst during the process. For CVD growth, the gas atmosphere limits the use of electron-based techniques. The resolution of other scanning probe microscopes is hindered by high temperatures. Although RHEED and SEM remain operational qualitative tools under very low gas pressure; x-ray scattering methods are applicable under gas-atmospheres as well as under vacuum conditions. Thus x-rays are a unique tool that can probe the structural properties during the growth of nanostructures and the evolution of surfaces nondestructively, independent on the gas-pressure and the sample temperature. Together with anomalous scattering and absorption spectroscopy, detailed information about the atomic structure and the incorporation of the

catalyst in the crystal lattice of the wires will be accessible.

2. Methods: the complementarity between GIXS, SXRD, XRR and GISAXS

The combination of GIXS, GIXD, SXRD, XRR and GISAXS *in situ*, during the growth of semiconductor islands can provides quantitative information on the surface morphology on the meso-scale (from a few nm to several μm), as well as on atomic length scales (*e.g.* strain in nanostructures). In particular, it gives access to the evolution of the internal atomic structure as strain, composition, and atomic ordering[325–327]. Recent developments of the experimental techniques but also of the analytical treatments have lead to the quantification of structural parameters as elastic energy, spatial resolution of strain and composition[328–330] or atomic ordering[327]. In addition to techniques sensitive to the mesoscale and to atomic long-range order, techniques like surface extended x-ray absorption fine structure (SEXAFS)[331], which are sensitive to the short-range atomic structure can also be used. A method combining absorption spectroscopy and diffraction called diffraction anomalous fine structure (DAFS), which has been developed over the last decade mainly by scientists working in the Grenoble area[332], could also be of applied *in situ*, with some specific effort. It has the advantage, that it can be selectively applied to a certain lattice parameter chosen by the diffraction condition and thus supplies a local probe of the environment of atoms of a specific element and a specific strain. Below are some hints on recent studies performed in our group by combining these X-ray techniques *in situ*, during the growth of germanium on silicon surfaces, paving the way to future studies performed during the growth of nanowires.

3. A glance on some recent in situ studies of SC performed using the BM32/SUV apparatus at the ESRF

a. Introduction During growth of Ge on Si at usual deposition temperatures (between 500°C and 800°C), the deposited material mixes with the substrate material, leading to the formation of alloyed nanocrystals. This is a favorable process, since it leads to a reduction of misfit strain between epilayer and substrate. The mechanisms leading to intermixing and their dependence on the growth conditions have been thoroughly studied in recent years, especially for the SiGe/Si model system. Pure bulk diffusion (*i.e.* atomic motion events in regions that are far from the surface) can be considered as practically absent due to its high potential barriers. Sub-surface processes can be relevant as the strain stored during the growth of Ge on Si substrates could significantly increase the atomic mobility in this region. The general picture emerging from these studies is that surface diffusion (*i.e.* migration of Si and Ge adatoms at the surface) must be regarded as the most active process as diffusion events are faster than bulk and sub-surface processes.

b. In-depth atomic structure and composition of the 2xN reconstruction of the 1 to 3 monolayer Ge wetting layer on Si(001) by surface x-ray diffraction Despite the fact that the growth of the Ge islands on Si(001) is intimately linked to the structure and composition of the wetting layer (WL), less attention has been devoted to these later. The nucleation process of the islands on the WL cannot just be described by the capture of newly deposited Ge atoms, since it also involves a diffusive interaction with the SiGe WL. At elevated growth temperatures above 600°C, a substantial amount of material is transferred from the WL to the islands during the initial stages of their formation[326]. Thus, a quantitative determination of the WL composition profile is essential for a detailed understanding of island formation and intermixing. We very briefly present the main results of our recent *in situ* SXRD investigation of the atomic structure of the $2 \times N$ reconstruction of the Ge/Si(001) wetting layer. Fig. 63 shows radial scans along the in-plane ($hh0$) direction as a function of the number of Ge ML deposited on Si(001) at 670°C. It exhibits scattering rods revealing the $2 \times N$ reconstruction, which is composed of $N-1$ rows of dimers, separated by dimer vacancies line (DVLs). The N periodicity of the reconstruction is found to decrease from 11.5 to 8 as the Ge deposition increases from 1 to 3 monolayers (ML), in agreement with other STM investigations as well as calculations. A complete SXRD quantitative measurement of the $(2 \times N)$ scattering rods allowed determining its structure and composition both in the dimer direction and perpendicular to it, as well as over a depth of height atomic planes[333]. The dimers were found to be asymmetric, with a bond length in the range of 2.50-2.60 Å and a buckling angle in the range of 9.4-15.6° depending on the Ge coverage, in good agreement with values calculated for alternating asymmetric dimers. In addition, intermixing down to the sixth (resp. eighth) layer has been found for the 2 (resp. 3) Ge ML coverage. For a 2 Ge ML coverage, the atomic structure and the Ge occupation probability for the 2×9 reconstruction have been determined (Fig. 64), and experimental evidence for the site selectivity of Si-Ge intermixing has been provided.

c. Growth of Ge on Si(001) studied in situ by a combination of GISAXS, GIXD and GI-MAD Above about 4 ML of Ge deposited, Ge islands start to form, first with the shape of pyramids, next domes and superdomes. The use of *in situ* GISAXS allowed following the evolution of the surface morphology and the facet formation of the Ge-islands. At the same time, the epitaxial strain was investigated via GIXD and the composition by using multiple

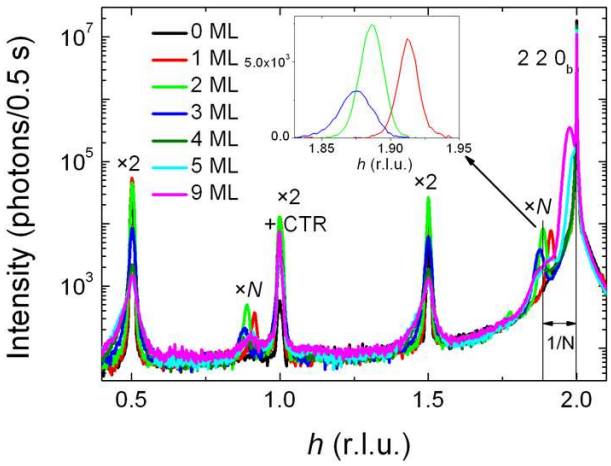

FIG. 63: Measured intensity (logarithmic units) during radial scans along the $(hh0)_b$ direction for clean Si and different deposited Ge ML indicated in the graph. The separation between the $\times N$ rod and the $((hh0)_b$ peak, for example, is equal to 1/N. Note that the $\times N$ reconstruction peaks are much wider and less intense than those of the $\times 2$ reconstruction. Inset: Background-subtracted $\times N$ rods for 1, 2, and 3 Ge ML

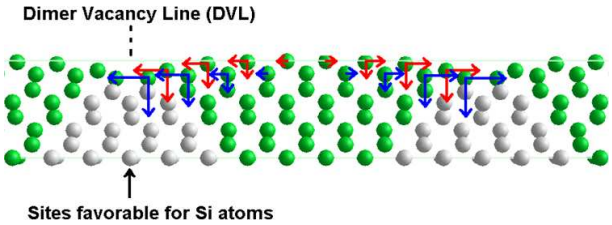

FIG. 64: Schematic representation of the atomic structure of the 2×9 reconstruction as deduced from our SXRD analysis. The red (resp. blue) arrows indicate the displacements of the atoms in the top (resp. second) layer. Lattice sites which are under tensile strain and thus richer in Ge atoms are marked with green disks. Sites under compression and thus richer in Si atoms are marked with white/gray disks.

wavelength anomalous scattering under grazing incidence (GI-MAD). The GISAXS method can monitor the facet evolution during the growth and thus determine the shape of the islands. The evaluation of the diffraction data leads to a quantitative determination of the material transport from the surface into the nanostructures. With these methods, material transport from the wetting layer during the transition from pyramidal growth (the {105} pyramid facets yielding intensity streaks along the reciprocal ⟨105⟩ direction) to dome (exposing {113} facets) growth could be tracked in this system[326]. As an example Fig. 65 presents GISAXS measurements showing the transition from pyramidal growth to dome growth for a deposition of 5 monolayers (ML) of Ge and 6 ML on Si(001) at a temperature of 600°C.

More recent studies have proven that depending on the growth rate, dislocated super domes of Ge are formed. An *in situ* GISAXS study allowed to follow the kinetic evolution of their facets as a function of time and temperature, and to discuss the growth mechanisms[334].

Grazing-incidence multiwavelength anomalous diffraction (GI-MAD) was also employed *in situ*, during growth, to quantitatively determine the average Ge composition of Ge/Si(001) islands - coherent pyramids and domes and incoherent superdomes - at different growth temperatures and for different Ge fluxes. The average Ge composition of the different islands was found to evolve during growth, suggesting that the composition is strongly correlated to surface morphology. The samples were grown at a low rate of 0.0048 ML/s. Height Ge monolayers (MLs) were deposited monolayer after monolayer. After-growth AFM analysis revealed the coexistence of pyramids (P), domes (D) and superdomes (SD) at the end of the growth.

During growth, the islands were characterized by GIXD (Fig. 66). These radial scans, which are sensitive to the strain relaxation of the islands, were recorded *in situ* for each added monolayer from the very first stages up to the nucleation of dislocated islands at T=500°C (Fig. 66-a) and T=650°C (Fig. 66-b). First, small pyramids were formed. Then, the introduction of dislocations led to a more complete relaxation: coherent islands such as domes or

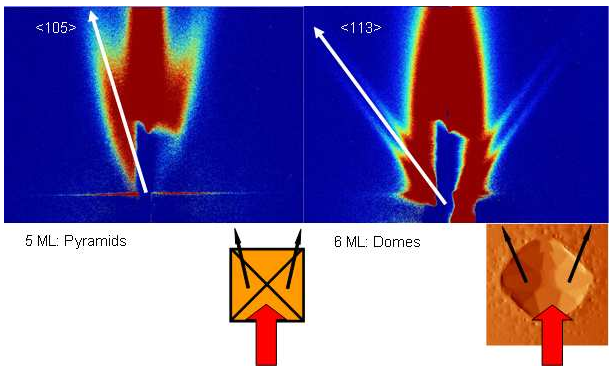

FIG. 65: GISAXS images recorded during growth for 5 and 6 ML Ge on Si(001) in the ⟨100⟩ and the ⟨110⟩ azimuth.

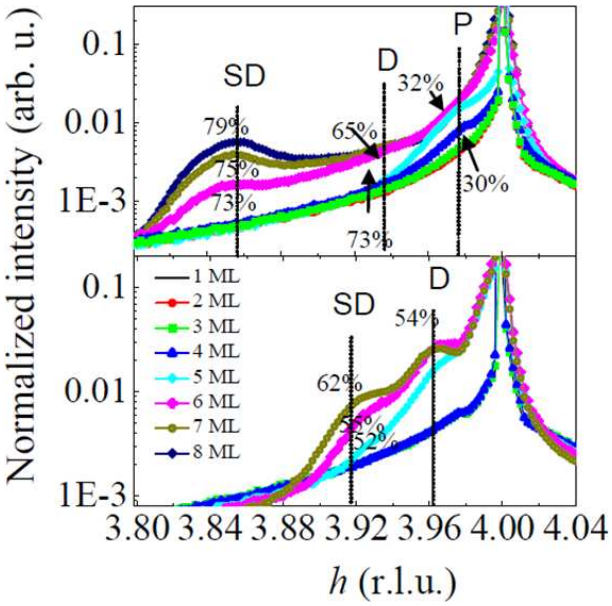

FIG. 66: Radial scans around the (400) Si Bragg reflection at an energy of 11.043 keV for samples grown with growth interruptions in-between deposited monolayers with a slow growth rate (a) at T=500°C and (b) at T=650°C. The numbers correspond to the Ge content associated to the different reciprocal space units, h.

barns are much more strained by the Si substrate. All the peaks have been indexed by the letters P, D and SD in Fig. 66. Their indexation is consistent with the AFM images at the end of the growth and also with finite element simulations. Further analysis was made possible by distinguishing the Ge and Si contributions during the growth process, using GI-MAD. This allowed to determine how the Ge composition evolves inside pyramids, domes and superdomes during their growth (Fig. 66). The average Ge composition inside pyramids may be underestimated by GI-MAD results as expanded regions of the Si substrate due to island growth can possibly contribute in the scattering regions of strained pyramids. A correlation between surface morphology and composition has been observed leading to less intermixing inside dislocated superdomes. During growth, the average Ge content of the different island shapes slightly evolves.

d. In situ x-ray investigation of Ge islands on pit patterned Si substrates The growth of ordered Ge islands on lithographically prepatterned Si(001) substrates has been intensively studied by *ex situ* techniques like AFM (see *e.g.* Ref.[335]), STM and *ex situ* x-rays. As these techniques do not allow to determine the chemical composition and the variation of relaxation prior to and during island formation, *in situ* x-ray scattering during growth appears to be very well adapted and capital to understand and investigate the whole dynamic growth process. To answer these questions, GISAXS and GIXD were combined to follow the *in situ* growth of ordered Ge islands on a Si(001) prepatterned substrate. The pit patterns of the substrate were two dimensionally ordered with a periodicity of

400nm. After an *ex situ* chemical cleaning process, including a final HF dip, and an *in situ* thermal treatment at 725°C under UHV conditions, a 60-nm-thick Si buffer layer was grown on the Si substrate while ramping the substrate temperature from 420°C to 650°C. This growth procedure eliminates the surface roughness. The surface quality was characterized with GIXD and RHEED, showing a Si-(2×1) reconstructed surface. Then, 7 monolayers (ML) of Ge were deposited at 650°C by molecular beam epitaxy. Figure 67 summarizes the growth process. During the very first stages of Ge growth (≤4ML: growth of the pseudomorphic wetting layer), the preliminary facets of the Si substrate are energetically unfavorable, and the pit facets break up into a rather complex pattern of $\{10n\}$ and $\{11m\}$ facets with n≥7 and m≥11. With increasing deposit, the angles of the faceted pits relative to the (001) plane decrease. The variation of the sidewalls inclination shows that Ge atoms preferentially fill the etched pits. Between 4 and 5 deposited ML, diffuse scattering appears around the Si(220) Bragg peak revealing the nucleation of 3D islands. At 5 ML, rods of scattering by {105}-type facets appear in the GISAXS image revealing the formation of pyramids. After 5ML, intense periodic rods arising from the ordered Ge domes are evidenced by GISAXS and an increase of the relaxation state is observed by GIXD. Then, after a deposit of 6ML, {113} and {15 3 23} facets are found, together with an increase of the diffuse scattering around $h = 2$. This is characteristic of the formation of large domes of mixed composition, Ge_xSi_{1-x}, which strongly distort the Si substrate below them, leading to the Si substrate deformation signal. At this pyramid to dome transition, an increase of the Ge content (from 40 to 50 percent) inside the islands is observed by anomalous GIXD. At the end of the growth (*i.e.* after a deposit of 7 ML of Ge), no superdomes are formed.

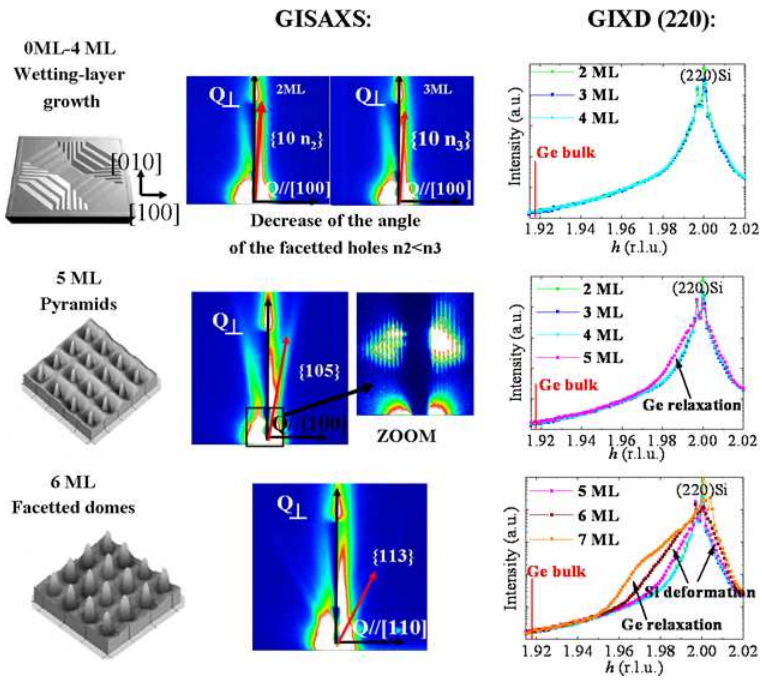

FIG. 67: Summary of the growth. The left part of the figure shows drawings of the sample. In the middle, GISAXS images can be observed along the ⟨100⟩ and ⟨110⟩ azimuths. The right part of the figure shows GIXD scans recorded during the growth.

A possible explanation of the localization of islands at the pit bottom is the asymmetrical migration of adatoms over steps of the sidewalls of patterned pits. Provided that the sidewalls of patterned structures are composed of steps and the activation barrier for adatoms migrating downwards over step is smaller than upwards, a net flux of adatoms at the sidewalls can be formed[320]. In conclusion, the combination of GISAXS and GIXD provides detailed results on the evolution of the shape, the strain and the degree of atomic ordering of Ge islands during the whole growth process. It is demonstrated to be a useful, destruction-free tool to understand and control the self-organized growth of semiconductor nanostructures.

We have also compared the strain state and the composition of Ge domes grown under the very same conditions on nominal and patterned Si(001) surfaces, by performing anomalous reciprocal space maps around different diffraction peaks (see Fig. 68). Domes grown on nominal and patterned Si(001) surfaces were found to have very similar composition, but largely different relaxation; the former being more strained. A combination with simulations allowed determining the complete 3D strain and composition fields inside both kinds of islands[26].

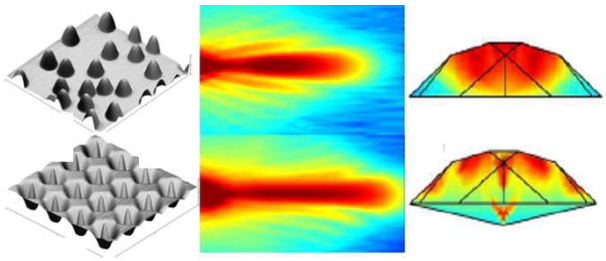

FIG. 68: Left: AFM of Ge domes grown under identical condition on nominal (top) and patterned (bottom) Si(001) surfaces. Middle: Map of the reciprocal space around their (400) Bragg peak. Right: Cross section of the composition profile as deduced by a combined experiment-simulation procedure.

e. Organized growth of Ge quantum dots on a nano-patterned Si(001) surface obtained by direct wafer bounding followed by chemical etching: An in situ X-ray study Si(001) substrates with a very small (20 to 50 nm) periodic nanometer scale patterning have been developed at the CEA-LETI laboratory by using wafer bounding and preferential chemical etching techniques. GISAXS, GIXD and GI-MAD were combined *in situ*, during growth, to investigated the preparation of these surfaces and the organized growth of Ge Qds on them, while characterizating their shape and organization as well as their strain and composition.

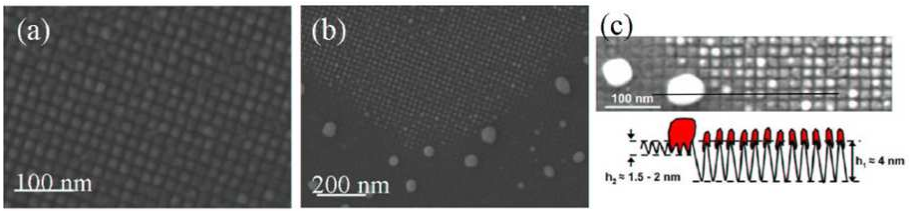

FIG. 69: (a)-(b)-(c) SEM images obtained after the growth of 6 ML of Ge at 500°C on the 20 nm twisted substrate and schematic drawing of the surface

The Si templates were obtained by combining the Smart Cut technology, wafer bounding and chemical etching of the surface. As the dislocation network is at the interface of the two bonded wafers it is necessary to perform a preferential etching to transfer the dislocation network symmetry (and period) to the surface[322]. The samples studied presented a square 20nm surface-patterning of periodic mesa separated by 3 to 4 nm deep trenches. After a chemical cleaning process, including a final HF dip, and thermal treatment in UHV at 650°C, a 2.5-nm-thick Si buffer layer was first grown on the surface at 650°C. The surface quality was characterized with GIXD and reflection of high energy electron diffraction (RHEED). GIXD allowed determining whether the Si bonded layer is removed by the chemical etching. For an increase of the etching time (depth), the disappearance of Bragg peak of the bounded layer and of the diffraction satellites by the dislocation network proves that the bonded layer is completely removed. This leaves a perfectly patterned Si(001) surface, which, however, is still periodically strain modulated. Six monolayers (ML) of Ge were then deposited at 500°C by molecular beam epitaxy. The deposition was followed *in situ* by X-rays, monolayer by monolayer. GISAXS measurements provided the detailed evolution of the morphology such as the faceted pits and shape of the grown Ge dots and allowed characterizing the degree of ordering between islands. GIXD added information on the island nucleation after the beginning of lattice relaxation and the evolution of the in-plane size, epitaxial orientation and strain of the Ge islands during growth. In addition, for each added ML, the Ge content inside the islands was determined using GI-MAD[336].

The 20 nm surface-patterning was not homogeneous over the whole surface. Scanning Electron Microscopy and Atomic Force Microscopy showed that the patterned areas are localized on stripes with a width of typically 300nm (see Fig. 69). Two contributions are then found by X-rays: one induced by the organized growth of Ge nanoparticles on the stripes and one corresponding to growth on a standard, non-patterned Si(001) surface. Nevertheless, the organization of Ge dots on the well-etched parts of the surface is confirmed by GISAXS, as intense periodic rods arising from the ordered Ge islands are evidenced by (anomalous) GISAXS (see Fig. 70). The shape factor of the mesa (trench depth, residual roughness, facet) is found to have a strong influence on the quantum dots shape and position, and especially to define the dots registry with the underlying substrate. In these samples, it appears that the trenches depth acts as an effective diffusion barrier to prevent large islands coalescence and intermixing between the dots and the substrate.

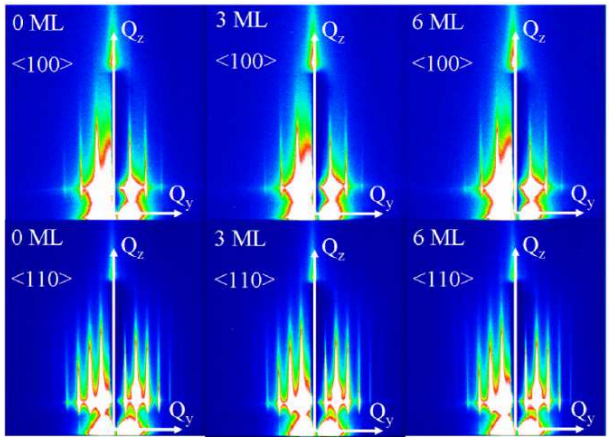

FIG. 70: GISAXS intensity maps along the ⟨100⟩ and ⟨110⟩ azimuths obtained at a growth temperature of 773 K for the 50 nm patterned template. The numbers denote the Ge thickness in ML.

This study gives a clear indication of the potential of this new substrate for the self-organization of nanostructures. It demonstrates that Ge islands are organized on well etched surfaces and that GIXS is a useful, destruction-free tool to understand and control the organized growth of nanostructures on substrates that are patterned at the nanometer scale.

4. A first step toward NW growth: the AuSi eutectic

The first step of Si NW growth via the VLS process using gold catalyst islands is the formation of liquid droplets of the eutectic composition, $Au_{81}Si_{19}$. As a preliminary step toward studying the growth of Si NW, we have performed systematic investigations with *in situ* x-ray scattering of the state of such AuSi islands, and found that in general they display a certain amount of supercooling, which can be enhanced when the interface with the Si(111) substrate has a specific reconstruction. Supercooling in metals *i.e.* the preservation of a disordered, fluid phase in a metastable state well below the melting point has led to speculations that local atomic structure configurations of dense, symmetric, but non-periodic packing act as the main barrier for crystal nucleation. For liquids in contact with solids, crystalline surfaces induce layering of the adjacent atoms in the liquid and often prevent or lower supercooling. This seed effect is supposed to depend on the local lateral order adopted in the last atomic layers of the liquid in contact with the crystal. Although it has been suggested that there might be a direct coupling between surface induced lateral order and supercooling, no experimental observation of such lateral ordering at interfaces is available. We found evidence for surface and interface induced supercooling of nanometric gold-silicon (AuSi) eutectic droplets laying on a silicon substrate, which stay liquid far below the bulk eutectic solidification temperature (T_e=363°C). Seven atomic layers of gold were deposited at room temperature (RT) on an Si(111) substrate (Fig. 71).

At RT, the Au film crystalline quality was found to be low but showed a clear preferential epitaxy with identical directions of the two cubic lattices: [110]Au(111)//[110]Si(111). When heating up to 350°C (*i.e.* below T_e) the Au film de-wets to form crystalline islands with a preferential in-plane epitaxy rotated by 19.2° with respect to the aligned epitaxy (*i.e.* [110]Au(111)//[231]Si(111)). This epitaxial change comes from a difference in thermal expansion between the two materials, which changes the mismatch values between Au and Si, changing the best coincidence epitaxial relationship. The islands are observed to melt exactly when the temperature is increased to T_e.

From this point we have paid particular attention on the solidification behavior of these AuSi droplets. *In situ* x-ray scattering measurements show that the silicon surface orientation and structure strongly influences the degree of supercooling (Fig. 72). Its minimum is observed on a Si(001) substrate. Depending on thermals treatments, Si(111) substrates present either Si(111)-($\sqrt{(3)} \times \sqrt{(3)}$ or Si(111)-(6×6) gold-induced reconstructions. The maximum degree of supercooling is observed on the Si(111)-(6x6) reconstruction, with a solidification at 230°C! We have determined the atomic structure of this reconstruction by a quantitative SXRD study, which yielded a structure based on pentagonal arrangements of gold atoms. *Ab initio* molecular dynamics simulations confirm the possibility of supercooling in a confined $Au_{81}Si_{19}$ alloy, revealing in addition a large proportion of local icosahedral order with a five-fold local ordering similar to that of the reconstructed surface. This reveals that pentagonal atomic arrangements of Au atoms at this interface favor a lateral-ordering stabilization process of the liquid phase (Fig. 73).

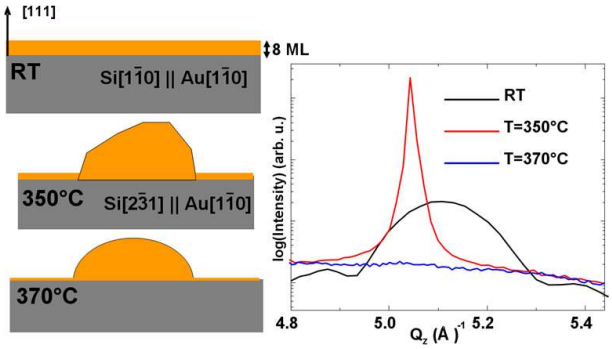

FIG. 71: Growth of Au-Si eutectic catalysts, the black curve on and out-off plane Au Bragg peak shows size oscillations corresponding to its thickness. Annealing at 350°C leads to islands (red curve. At 370°C, Au Bragg peaks disappear: the island transforms into a $Au_{81}Si_{19}$ liquid droplet.

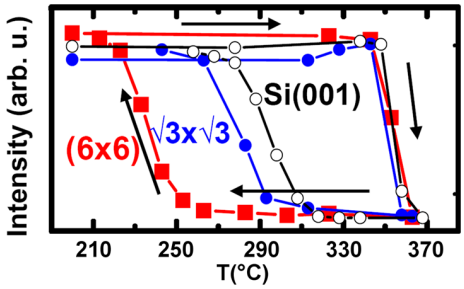

FIG. 72: Hysteresis loops of the integrated intensity of the Au(220) Bragg peak during the solid-liquid-solid transition on Si(001) (black open circles), on a Si(111)-($\sqrt{(3)} = \times\sqrt{(3)}$)R30° reconstruction (blue disks) and on a Si(111)-(6 × 6) reconstruction (red squares).

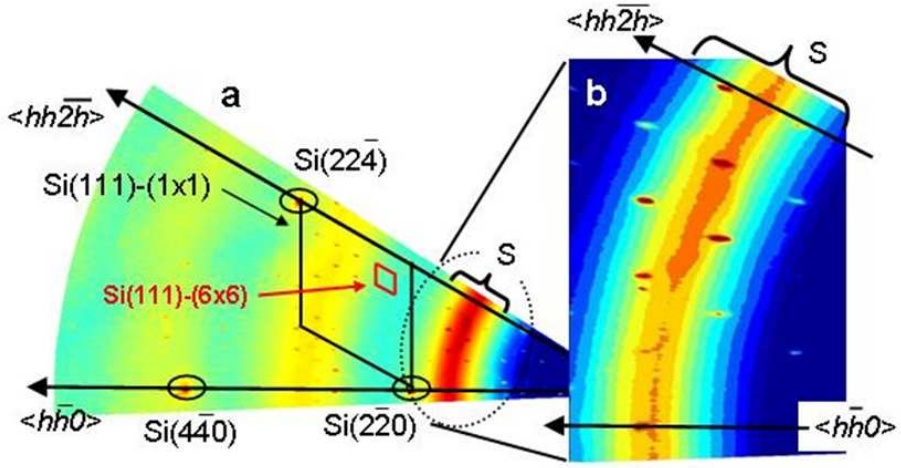

FIG. 73: Reciprocal space mapping (RSM) of liquid AuSi islands on (6 × 6) reconstructed Si(111). a) RSM of the liquid in its supercooled state on a (6 × 6) reconstructed Si(111) surface. Blue color corresponds to low intensity, and red to high intensities, the yellow one being intermediate. Three bulk Bragg peaks are visible, together with a mesh of smaller peaks arising from the (6 × 6) surface/interface periodic superstructure. The three diffuse rings correspond to liquid-like scattering. b) Anisotropy of the first order maximum of the liquid structure factor: In the vicinity of strong (6 × 6) reconstruction peaks the signal from the liquid is enhanced, underlining morphological similarities between the crystalline surface and the adjacent liquid layers.

This interface-enhanced stabilization of the liquid state proves the importance of solid-liquid interaction on the structure of the adjacent liquid layers as well as for the stability of liquids under confined conditions[27].

D. Project of *in situ* X-ray studies of IV-IV semiconductor nanowire growth by Chemical Beam Epitaxy

a. Scientific and technical impact As shown above, the SUV/BM32 instrument at the ESRF has been evolving over the last years to allow for the *in situ* growth of some SC, mostly Si and Ge, but the growth of GaAlN has also been performed[337,338]. Recently first tests of the VLS growth in the MBE chamber at BM32 have proven to result in the growth of Si wires. However, replacing the MBE deposition by the use of a gas source process offers the great advantage of the selectivity of the deposition: the mobility of the element (here Si) is supplied by the Gas phase (SiH_4) and is thus independent on the temperature. The use of catalysts that crack the molecules and form a eutectic solution with Si allows choosing the nucleation site. As a consequence no material is deposited on the bare substrate and a pure growth of rods is obtained by this process. In MBE growth, the catalysts lead to a local increase of the growth rate, but growth is always present between the wires.
Thus, our project is to extend the current instrument to include *in situ* gas source deposition of Si, Ge, but also C in the near future, since it is better adapted to growth GeSi NWs and graphene sheets. The instrument and tools combining *in situ* MBE and CVD under X-rays will allow quantifying parameters of the growth dynamic and evolution that are difficult to access with other methods. Studies of different material systems and different catalysts require a high flexibility concerning the growth installation, which will be obtained by combining a variety of metal deposition sources as well as group IV semiconductors growth. The flexibility of the proposed growth system will allow to work under UHV conditions at base pressures of a few 10^{-11} mbar to perform ultraclean surface preparations and MBE growth as well as a quick change to UHV-CVD conditions in a pressure range of up to 10^{-3} mbar. CBE growth of wire structures finally combines the cleanliness of UHV and MBE preparation of surfaces with a highly mobile deposition method using gas-molecules instead of solid elements. This method allows thus an almost defect free epitaxy of semiconductors even with high lattice mismatch and opens the way to new heterostructures mixing group IV and III-V elements and combining their advantages[281,339]. In the future, after the method has been well established on IV-IV semiconductors, we could think of extending the complexity of the investigated wire systems: heterostructures of group IV semiconductors and, in a later stage of the project, semiconductors of III-V type could come in the focus of interest. This would require a further extension of the gas supplies in order to permit a sufficient flexibility between III-V and group IV systems.

b. Deposition, epitaxy and ordering of catalysts for semiconductor wire growth The first studies will concern the growth using CBE of Si NWs according to the VLS process using the common Au catalyst, as well as alternative catalysts such as Ga and Al[312] for which the growth mode is less-well understood. One of the first fundamental questions to be answered in the framework of this project will be the behavior of the different catalysts under Si-flux (MBE) and under SiH_4 flux (CBE). We intend to combine these processes with our knowledge on the preparation of Si-surfaces (especially patterned ones), Ge-growth and metallic nanoparticles. Any structural change of the surface or the catalyst can be monitored *in situ* by x-ray diffraction. Furthermore, other x-ray methods as Extended X-ray Absorption Fine Structure (EXAFS) and Diffraction Anomalous Fine Structure (DAFS) can be applied in the SUV/BM32 apparatus to probe the dilution of the catalyst in the bulk Si or in the growing Si-wire. The surface preparation methods will be developed as described above under MBE conditions. The metal catalyst deposition can be controlled with sub-monolayer precision. For the growth of the Si nanowires we will employ MBE processes as well as CBE processes and a combination of both. The next step will be to investigate the growth of the NWs themselves.

Figure 74 schematically shows the different steps of the wire fabrication and the various parameters accessible by *in situ* x-ray scattering during the growth for the example of SiGe-wires based on MBE-grown Au-catalysts and silane/germane as process gases. Here, x-ray diffraction definitely offers a tool yielding unequaled information about details and kinetics of this process. These range from extreme sensitivity to the solid-liquid transition up to stages of solidification and epitaxial relationship. Diffraction yields the possibility to follow in detail the formation of eutectics, and thus our instrument will be well suited for the search for alternative catalysts for the VLS process. In parallel, we will concentrate on the growth of Si nanowires with an *in situ* follow up of crucial parameters as mosaicity (so far one drawback is that these systems can only be grown as highly mosaic ensembles) in early nucleation stages and its evolution and dependence on growth parameters, as temperature and gas pressure. Next, SiGe wire heterostructures, axial or radial, and their structural properties will be in the focus of our interest. As in these complex structures, the strain will play a crucial role for the bandstructure and hence the luminescence energy, a lattice parameter sensitive tool as x-rays, will allow following the structural parameters during the formation of such heterostructures. Furthermore, the study of the conditions of Silicide formation and ordering for different catalytic metals will be studied using *in situ* x-ray diffraction. With the installation of the UHV-CVD equipment, the CBE-Vapor Liquid Solid (VLS) transition will be investigated in detail.

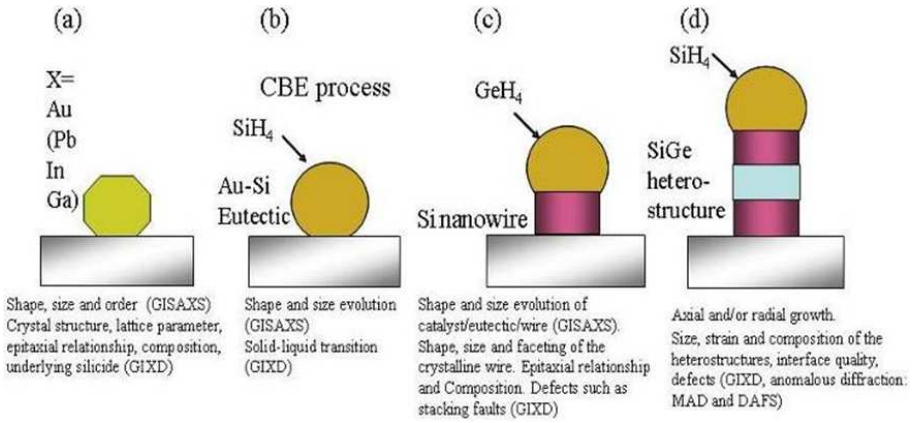

FIG. 74: Overview of the accessible parameters via *in situ* x-ray scattering during different stages of the catalytic growth of SiGe nanowires on Si(111). (a): deposition of the metallic catalyst. (b) Exposure to Silane (SiH_4), causes to the catalyst to crack the molecules, release the hydrogen and form a liquid phase eutectic. (c): After saturation of the eutectic, Si nucleates on the Si-surface and forms a Si-wire. (d) Alternative exposure to SiH_4 and GeH_4 causes the growth of a heterostructure inside the wire.

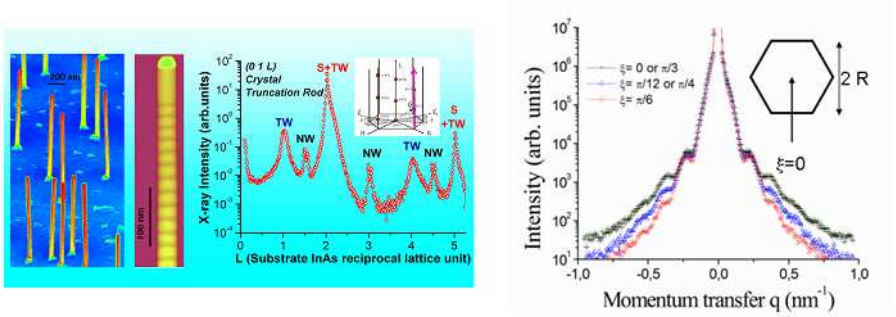

FIG. 75: GIXD (left) and GISAXS(right) Intensity distribution of a homogeneous ensemble of InAs nanowires containing InAs/InP heterostructures. In diffraction, the different lattice parameter contributions can be clearly distinguished. The GISAXS intensity distribution to the right shows size oscillations that allow to determine the lateral size as well as its distribution.

After the nucleation, the growing nanowires and their evolution concerning parameters like shape, size, lattice relaxation and mosaicity in heterostructures can be followed *in situ*. Figure 75 shows an example of recently published results for studies performed *ex situ* on InAs nanowires containing InP heterostructures[340]. The size of the wires is in this case easily detected by the size oscillations in the GISAXS pattern shown to the right. Diffraction from the nanowires InAs/InP superlattice is shown in the left part. Such a scan allows determining the strain distribution in the heterostructures, but also the nature of the crystalisation, Zinckblende or Wurtzite structure in this case. The experiments we propose would allow for a real time detection of these parameters during growth, detecting possible structural transitions during growth. In addition, together with anomalous scattering and absorption spectroscopy, detailed information about the atomic structure and the incorporation of the catalyst in the crystal lattice of the wires will be accessible. GISAXS will also allow to detect the presence of different facets along the edges of the NWs, such as those evidenced by *in situ* TEM on growing Si NWs[305].

E. Conclusions

The implementation of Chemical Beam Epitaxy on the UHV surface diffractometer of the BM32 ESRF beamline will open the way to many new studies, some of which have been briefly discussed above regarding the first steps of the growth of SC NWs. Obviously, the very first studies will deal with X-ray scattering investigations of the homoepitaxial growth of Si on Si and Ge on Ge, in both orientations, (001) which is the most studied in view

of its importance in microelectronics, and (111), being the natural orientation of the substrate to grow SC NWs perpendicular to it. These measurements will consist of GIXD using a 2D detector at anti-Bragg reflections to look at the oscillating intensities, both coherent and diffuse, yielding information on growth modes (layer-by-layer vs step flow and random deposition) and on the size of sub-monolayer islands, from which activation energies will be deduced[341]. Possible different reconstructions under gas as compared to UHV will also be studied by GIXD. The UHV-CVD heteroepitaxial growth of Ge on Si (in both (001) and (111) orientations) will also certainly be addressed, in order to determine the wetting layer structure, the 2D/3D transition and the kinds of islands that develop. The cases of UHV-CVD growth will be compared to the cases of MBE growth which we have already studied. The phase diagram of binary alloys that catalyzes the growth of NWs will also be studied under gas atmosphere, as well as possibly differing supercooling behaviors. These preliminary studies will likely be performed before or in parallel with the first studies of growing NWs. In order to grow state of the art NWs, the addition of complementary gases such as H_2, Si_2H_6 or HCl might also rapidly become necessary. The CBE of ethane, C_2H_4, will also be quickly implemented since it is the best way to grow well-defined graphene sheets on different substrates. We are especially interested in graphene on metallic substrates like Ir(111), which is of exceptional quality, and displays a 2D periodic corrugation which can be used as a template for the organized growth of nanoparticles, especially magnetic ones such as Co dots, but also possibly organic molecules. One of our project is to fully unravel the structure and morphology of the graphene sheets, and study the organized growth of nanoparticles on them. Growth of carbon by CBE might also in the future allow studying the grow the diamond crystals. Certainly, in the future, the very diverse combinations of physical and chemical deposition offered by the system will open the way to investigate the growth/structure/morphology of very diverse systems.

---

[1] F. Leroy, G. Renaud, A. Létoublon, R. Lazzari, C. Mottet, and J. Goniakowski, Phys. Rev. Lett. **95**, 185501 (2005).
[2] G. Renaud, N. Motta, F. Lancon, and M. belakhovsky, Phys. Rev. B **38**, 5944 (1988).
[3] G. Renaud, P. Fuoss, A. Ourmazd, J. Bevk, B. Freer, and P. Hahn, Appl. Phys. Lett. **58**, 1044 (1991).
[4] G. Renaud, P. Fuoss, J. Bevk, and B. Freer, Phys. Rev. B **45**, 9192 (1992).
[5] P. H. Fuoss, D. Kisker, G. Renaud, K. Tokuda, S. Brennan, and J. Kahn, Phys. Rev. Lett. **63**, 2389 (1989).
[6] G. Renaud, B. Vilette, and P. Guénard, Nucl. Inst. and Meth. **95**, 422 (1995).
[7] G. Renaud, B. Villete, I. Vilfan, and A. Bourret, Phys. Rev. Lett. **73**, 1825 (1994).
[8] P. Guenard, A. Renaud, Barbier, and M. Gautier-Soyer, Surf. Rev. Lett. **5**, 321 (1997).
[9] P. Guénard, G. Renaud, and B. Villette, Physica B **221**, 205 (1996).
[10] R. Baudoing-Savois, M. De Santis, M. C. Saint-Lager, P. Dolle, O. Geaymond, P. Taunier, P. Jeantet, J. P. Roux, G. Renaud, A. Barbier, et al., Nucl. Instr. Meth. Phys. Res. B **149**, 213 (1999).
[11] A. Barbier, C. Mocuta, K. A., K. Peters, B. Richter, and G. Renaud, Phys. Rev. Lett. **84**, 2897 (2000).
[12] O. Robach, G. Renaud, and A. Barbier, Surf. Sci. **401**, 227 (1998).
[13] G. Renaud, Surf. Sci. Rep. **32**, 1 (1998).
[14] C. Mocuta, A. Barbier, G. Renaud, and B. Dieny, Thin Sol. Films **336**, 160 (1998).
[15] G. Renaud, A. Barbier, and O. Robach, Phys. Rev. B **60**, 5872 (1999).
[16] G. Renaud, R. Lazzari, C. Revenant, A. Barbier, M. Noblet, O. Ulrich, F. Leroy, J. Jupille, Y. Borensztein, C. R. Henry, et al., Science **300**, 1416 (2003).
[17] G. Renaud, M. Ducruet, O. Ulrich, and R. Lazzari, Nucl. Inst. Meth. B **222**, 667 (2004).
[18] C. Revenant, F. Leroy, R. Lazzari, G. Renaud, and C. R. Henry, Phys. Rev. B **69**, 035411 (2004).
[19] F. Leroy, R. Lazzari, and G. Renaud, Surf. Sci. **601**, 1915 (2007).
[20] J. Olander, R. Lazzari, B. Mangili, J. Goniakowski, G. Renaud, and J. Jupille, Phys. Rev. B **76**, 075409 (2007).
[21] R. Lazzari, F. Leroy, and G. Renaud, Phys. Rev. B **76**, 125411 (2007).
[22] F. Leroy, G. Renaud, A. Létoublon, and R. Lazzari, Phys. Rev. B **77**, 235429 (2008).
[23] R. Lazzari, G. Renaud, C. Revenant, J. Jupille, and Y. Borensztein, Phys. Rev. B **79**, 125428 (2009).
[24] R. Lazzari, J. Appl. Cryst. **35**, 406 (2002).
[25] G. Renaud, R. Lazzari, and F. Leroy, Surf. Sci. Rep. **64**, 255 (2009).
[26] M.-I. Richard, V. Favre-Nicolin, G. Renaud, T. Schulli, C. Priester, A. Zhong, and T.-H. Metzger, Phys. Rev. Lett. **102**, 025502 (2009).
[27] T. Schulli, R. Daudin, G. Renaud, A. Vaysset, O. Geaymond, and A. Pasturel, Nature **464**, 1174 (2010).
[28] C. Teichert, Surf. Sci. Rep. **365**, 335 (2002).
[29] C. Henry, Surf. Sci. Rep. **31**, 231 (1998).
[30] R. Meyer, C. Lemire, S. K. Shaikhutdinov, and H. J. Freund, Gold Bull. **37**, 72 (2004).
[31] S. H. Sun, C. B. Murray, D. Weller, L. Folks, and A. Moser, Science **287**, 1989 (2000).
[32] J. Bansmann, S. H. Baker, C. Binns, J. A. Blackman, J.-P. Bucher, J. Dorantes-Davila, V. Dupuis, L. Favre, D. Kechrakos, A. Kleibert, et al., Surf. Sci. Rep. **56**, 189 (2005).
[33] C. Lamberti, *Characterization of Semiconductor Heterostructures and Nanostructures* (Elsevier, 2008).

[34] E. Borovitskaya and M. Shur, *Quantum dots* (World Scientific, New Jersey, London, Singapore, Hong Kong, 2002).
[35] M. Zinke-Allmang, L. C. Feldman, and M. H. Grabow, Surf. Sci. Rep. **16**, 377 (1992).
[36] W. C. Marra, P. Eisenberger, and A. Y. Cho, J. Appl. Phys. **50**, 6927 (1979).
[37] P. Eisenberger and W. C. Marra, Phys. Rev. Lett. **46**, 1081 (1981).
[38] R. Feidenhans'l, Surf. Sci. Rep. **10**, 105 (1989).
[39] I. K. Robinson and D. J. Tweet, Rep. Prog. Phys. **55**, 599 (1992).
[40] J. Daillant and A. Gibaud, *X-ray and neutron reflectivity : principle and applications*, Lectures notes in physics (Springer, 1999).
[41] V. Holý, U. Pietsch, and T. Baumbach, *High-resolution X-ray scattering from thin films and multilayers*, vol. 149 of *Springer Tracts in Modern Physics* (Spinger, 1998).
[42] J. R. Levine, J. B. Cohen, Y. W. Chung, and P. Georgopoulos, J. Appl. Cryst. **22**, 528 (1989).
[43] J. R. Levine, J. B. Cohen, and Y. W. Chung, Surf. Sci. **248**, 215 (1991).
[44] A. Naudon and D. Thiaudière, J. Appl. Cryst. **30**, 822 (1997).
[45] D. Thiaudière, O. Proux, J.-S. Micha, C. Revenant, J.-R. Regnard, and S. Lequien, Physica B **283**, 114 (2000).
[46] F. Gonella, E. Cattaruzza, G. Battaglin, F. d'Acapito, C. Sada, P. Mazzoldi, C. Maurizio, G. Mattei, A. Martorama, A. Longo, et al., J. Non-Cryst. Solids **280** (2001).
[47] T. Rochand, V. Holý, A. Daniel, E. Höflinger, M. Meduna, T. H. Metzger, G. Bauer, J. Zhu, K. Brunner, and G. Abstreiter, J. Phys. D: Appl. Phys. **34** (2001).
[48] J. Stangl, V. Holý, P. Mikulik, G. Bauer, I. Kegel, T. H. Metzger, O. G. Schmidt, C. Lange, and K. Eberl, Appl. Phys. Lett. **74**, 3785 (1999).
[49] M. Schmidbauer, T. Wiebach, H. Raidt, M. Hanke, R. Köhler, and H. Wawra, Phys. Rev. B **58**, 10523 (1998).
[50] M. Schmidbauer, T. Wiebach, H. Raidt, M. Hanke, R. Köhler, and H. Wawra, J. Phys. D: Appl. Phys. **32** (1999).
[51] R. Lazzari, IsGISAXS web site : : http://www.insp.jussieu.fr/axe2/Oxydes/IsGISAXS/isgisaxs.htm (2002).
[52] B. Voigtländer, G. Meyer, and N. M. Amer, Phys. Rev. B **44**, 10354 (1991).
[53] O. Fruchart, G. Renaud, J.-P. Deville, A. Barbier, F. Scheurer, M. Klaua, J. Barthel, M. Noblet, O. Ulrich, J. Mane-Mane, et al., J. Cryst. Growth. **237-239**, 2035 (2002).
[54] M. C. Saint-Lager, A. Bailly, P. Dolle, R. Baudoing-Savois, P. Taunier, S. Garaudée, S. Cuccaro, S. Douillet, O. Geaymond, G. Perroux, et al., Rev. Sci. Inst. **78**, 083902 (2007).
[55] M. C. Saint-Lager, A. Bailly, M. Mantilla, S. Garaudée, R. Lazzari, P. Dolle, O. Robach, J. Jupille, I. Laoufi, and P. Taunier, Gold. Bull. **42**, 159 (2008).
[56] S. K. Sinha, E. B. Sirota, S. Garoff, and H. B. Stanley, Phys. Rev. B **38**, 2297 (1988).
[57] M. Rauscher, T. Salditt, and H. Spohn, Phys. Rev. B **52**, 16855 (1995).
[58] M. Rauscher, R. Paniago, T. H. Metzger, Z. Kovats, J. Domke, H. D. Pfannes, J. Schulze, and I. Eisele, J. Appl. Phys. **86**, 6763 (1999).
[59] J. Als-Nielsen and D. McMorrow, *Elements of modern X-ray physics* (John Wiley & Sons, New York, 2001).
[60] J. R. Levine, P. Georgopoulos, Y. W. Chung, and J. B. Cohen, J. Phys. IV **C8**, 411 (1993).
[61] A. Naudon, T. Slimani, and P. Goudeau, J. Appl. Cryst. **24**, 501 (1991).
[62] A. Naudon, D. Babonneau, D. Thiaudière, and S. Lequien, Physica B **283**, 69 (2000).
[63] D. Thiaudière and A. Naudon, J Phys IV **6**, 553 (1996).
[64] D. Babonneau, F. Petroff, J. L. Maurice, F. Fettar, A. Vaurès, and A. Naudon, Appl. Phys. Lett. **76**, 2892 (2000).
[65] D. Babonneau, I. R. Videnović, M. G. Garnier, and P. Oelhafen, Phys. Rev. B **63**, 195401 (2001).
[66] B. M. Lairson, A. P. Payne, S. Brennan, N. M. Rensing, B. J. Daniels, and B. M. Clemens, J. Appl. Phys. **78**, 4449 (1995).
[67] V. Holý, J. Kubuena, I. Ohlídal, K. Lischka, and W. Plotz, Phys. Rev. B **47**, 15896 (1993).
[68] V. Holý and T. Baumbach, Phys. Rev. B **49**, 10668 (1994).
[69] T. H. Metzger, I. Kegel, R. Paniago, A. Lorke, J. Peisl, J. Schulze, I. Eisele, P. Schittenhelm, and G. Abstreiter, Thin Solid Films **336**, 1 (1998).
[70] T. H. Metzger, I. Kegel, R. Paniago, and J. Peisl, J. Phys. D: Appl. Phys. **32**, A202 (1999).
[71] J. Stangl, V. Holý, T. Roch, A. Daniel, G. Bauer, J. Zhu, K. Brunner, and G. Abstreiter, Phys. Rev. B **62**, 7229 (2000).
[72] K. Zhang, C. Heyn, W. Hansen, T. Schmidt, and J. Falta, Appl. Surf. Sci. **175-176**, 606 (2001).
[73] V. Holý, T. Roch, J. Stangl, A. Daniel, G. Bauer, T. H. Metzger, Y. H. Zhu, K. Brunner, and G. Abstreiter, Phys. Rev. B **63**, 205318 (2001).
[74] V. Holý, J. Stangl, G. Springholz, M. Pinceolits, and G. Bauer, J. Phys. D: Appl. Phys. **34**, A1 (2001).
[75] Y. Yoneda, Phys. Rev. **131**, 2010 (1963).
[76] L. B. N. Laboratory, *Center for x-ray optics*, http://www-cxro.lbl.gov/.
[77] A. Guinier, *X-ray diffraction in crystals, imperfect crystals and amorphous bodies* (Dover Publications, Inc, New York, 1963).
[78] B. E. Warren, *X-ray diffraction* (Dover Publication , Inc, New York, 1969).
[79] R. Hosemann and S. N. Bagchi, *Direct analysis of diffraction by matter* (North-Holland Publishing Company, Amsterdam, 1962).
[80] H. Dosch, *Critical phenomena at surfaces and interfaces: Evanescent X-ray and neutron scattering* (Springer-Verlag, Berlin, 1992).
[81] S. Dietrich and A. Haase, Phys. Rep. **260**, 1 (1995).
[82] E. Vlieg, J. Appl. Cryst. **30**, 532 (1997).
[83] O. Robach, Y. Garreau, K. Aïd, and M. Véron-Jolliot, J. Appl. Cryst. **33**, 1006 (2000).

[84] BM32 web site : http://www.esrf.fr/exp_facilities/BM32/index.htm (2004).
[85] J. M. Bloch, J. Appl. Cryst. **18**, 33 (1985).
[86] J. Als-Nielsen, D. Jacquemain, K. Kjaer, F. Leveiller, and M. Lahav, Phys. Rep. **246**, 251 (1994).
[87] X. L. Zhou and S. H. Chen, Phys. Rep. **257**, 223 (1995).
[88] J. K. Basu and M. K. Sanyal, Phys. Rep. **363**, 1 (2002).
[89] S. K. Sinha, J. Phys. III France **4**, 1543 (1994).
[90] K. Omote, Y. Ito, and S. Kawamura, Appl. Phys. Lett. **82**, 544 (2003).
[91] B. Lee, J. Yoon, W. Oh, Y. Hwang, K. Heo, K. S. Jin, J. Kim, K. W. Kim, and M. Ree, Macromolecules **38**, 3395 (2005).
[92] B. Lee, I. Park, J. Yoon, S. Park, J. Kim, C. T. Kim, K.-W, and M. Ree, Macromolecules **38**, 4311 (2005).
[93] M. Tate, V. N. Urade, J. D. Kowalski, T. Wei, B. D. Hamilton, B. W. Eggiman, and H. W. Hillhouse, J. Phys. Chem. B **110**, 9882 (2006).
[94] N. Jedrecy, G. Renaud, R. Lazzari, and et al., Phys. Rev. B **72**, 45430 (2005).
[95] B. Lee, C. T. Lo, P. Thiyagarajan, D. R. Lee, Z. Niu, and Q. Wang, J. Appl. Cryst. **41**, 134 (2008).
[96] M. von Laue, Ann. Phys. (Leipzig) **26**, 55 (1936).
[97] R. W. James, *The optical principles of the diffraction of X-rays* (Cornell University Press, New York, 1965).
[98] I. A. Vartanyants, A. V. Zozulya, K. Mundboth, O. Yefanov, M. I. Richard, E. Wintersberger, J. Stangl, A. Diaz, C. Mocuta, T. H. Metzger, et al., Phys. Rev. B **77**, 115317 (2008).
[99] C. Revenant, G. Renaud, R. Lazzari, and J. Jupille, Phys. Rev. B **79**, 1 (2009).
[100] A. Guinier and G. Fournet, *Small-angle scattering of X-rays* (Jonh Wiley & Sons, New York, 1955).
[101] G. Glatter and O. Kratky, *Small angle X-ray scattering* (Academic Press, 1982).
[102] S. K. Sinha, M. Tolan, and A. Gibaud, Phys. Rev. B **57**, 2740 (1998).
[103] M. Tolan and S. K. Sinha, Physica B **248**, 399 (1998).
[104] I. A. Vartanyants and I. K. Robinson, J. Phys.: Condens. Matter **13**, 10593 (2001).
[105] I. A. Vartanyants and I. K. Robinson, Optics Communications **222**, 29 (2003).
[106] A. P. Payne and B. M. Clemens, Phys. Rev. B **47**, 2289 (1993).
[107] Y. Waseda, *The structure of non-crystalline materials* (Mc. Graw-Hill, New-York, 1980).
[108] T. E. Faber and J. M. Ziman, Phil. Mag. **11**, 153 (1965).
[109] A. Vrij, J. Chem. Phys. **69**, 1742 (1978).
[110] A. Vrij, J. Chem. Phys. **71**, 3267 (1979).
[111] P. Van Beurten and A. Vrij, J. Chem. Phys. **74**, 2744 (1981).
[112] M. Zinke-Allmang, Thin Solid Films **346**, 1 (1999).
[113] J. Venables, *Introduction to surface and thin film processes* (Cambridge University Press, Cambridge, United Kingdom, 2000).
[114] D. Gazzillo, A. Giacometti, R. Guido Della Valle, E. Venutti, and F. Carsughi, J. Chem. Phys. **111**, 7636 (1999).
[115] M. Kotlarchyk and S.-H. Chen, J. Chem. Phys. **79**, 2461 (1983).
[116] J. S. Pedersen, J. Appl. Cryst. **27**, 595 (1994).
[117] J. S. Pedersen, P. Vysckocil, B. Schönfeld, and G. Kostorz, J. Appl. Cryst. **30**, 975 (1997).
[118] W. K. Bertram, J. Appl. Cryst. **31**, 489 (1998).
[119] J. S. Pedersen, J. Appl. Cryst. **31**, 488 (1998).
[120] F. Leroy, R. Lazzari, and G. Renaud, Acta. Cryst. A **60**, 565 (2004).
[121] W. K. Bertram, J. Appl. Cryst. **29**, 682 (1996).
[122] R. Balescu, *Equilibrium and nonequilibrium statistical mechanics* (Jonh Wiley & Sons, New York London Sidney Toronto, 1975).
[123] M. Baus and J. L. Colot, Phys. Rev. A **36**, 3912 (1987).
[124] R. Hosemann, Acta. Cryst. **4**, 520 (1951).
[125] T. R. Welberry, G. H. Miller, and C. E. Carroll, Acta. Cryst. A **36**, 921 (1980).
[126] R. Hosemann and A. Hindeleh, J. Macromol. Sci. Phys. **B34**, 327 (1995).
[127] H. Matsuoka, H. Tanaka, T. Hashimoto, and N. Ise, Phys. Rev. B **36**, 1754 (1987).
[128] H. Matsuoka, H. Tanaka, T. Hashimoto, and N. Ise, Phys. Rev. B **41**, 3854 (1990).
[129] X.-Q. Mu, Acta. Cryst. A **54**, 606 (1998).
[130] R. P. Millane and J. L. Eads, Acta. Cryst. **A56**, 497 (2000).
[131] W. Wilke, Acta. Cryst. A **39**, 864 (1983).
[132] J. L. Eads and R. P. Millane, Acta. Cryst. A **57**, 507 (2001).
[133] B. Busson and J. Doucet, Acta. Cryst. A **56**, 68 (2000).
[134] A. Gibaud, A. Baptiste, D. A. Doshi, C. J. Brinker, L. Yang, and B. Ocko, Europhys. Lett. **63**, 833 (2003).
[135] R. Lazzari, F. Leroy, G. Renaud, and J. Jupille, Phys. Rev B. **76**, 125412 (2007).
[136] C. Revenant, F. Leroy, G. Renaud, R. Lazzari, A. Létoublon, and T. E. Madey, Surf. Sci. **601**, 3431 (2007).
[137] O. Robach, Ph.D. thesis, Université Joseph Fourier Grenoble I, France (1997).
[138] P. W. Zhu and J. W. White, J. Chem. Phys. **22**, 9169 (1996).
[139] J. A. Venables, Phil. Mag. **27**, 697 (1973).
[140] C. Revenant, G. Renaud, R. Lazzari, and al., Nucl. Inst. Meth. B **246**, 112 (2006).
[141] R. Lazzari, G. Renaud, C. Revenant, J. Jupille, and Y. Borensztein, Phys. Rev B. **79**, 125428 (2009).
[142] P. Fratzl, J. L. Lebowitz, O. Penrose, and J. Amar, Phys. Rev. B **44**, 4794 (1991).
[143] D. Gazzillo, A. Giacometti, and F. Carsughi, Phys. Rev. E **60**, 6722 (1999).

[144] J. S. Pedersen, Advances in Colloid and Interface Science **70**, 171 (1997).
[145] B. Lee, S. Seifert, S. J. Riley, G. Tikhonov, N. A. Tomczyk, S. Vajda, and R. E. Winans, J. Chem. Phys. **123**, 074701 (2005).
[146] W. H. Press, S. A. Teukolsky, W. T. Vetterling, and B. P. Flannery, *Numerical Recipes in Fortran* (Cambridge University Press, 1992).
[147] H. J. Freund, Surf. Sci. **500**, 271 (2002).
[148] J. Jupille, Surf. Rev. Lett. **8**, 69 (2001).
[149] J. L. Menéndez, P. Caro, and A. Cebollada, J. Cryst. Growth **192**, 164 (1998).
[150] M. Valden, X. Lai, and D. W. Goodman, Science **281**, 1647 (1998).
[151] C. T. Campbell, Surf. Sci. Rep. **27**, 1 (1997).
[152] C. T. Campbell, S. C. Parker, and D. E. Starr, Science **298**, 811 (2002).
[153] P. Deltour, J. L. Barrat, and P. Jensen, Phys. Rev. Lett. **78**, 4597 (1997).
[154] C. Revenant, G. Renaud, R. Lazzari, and J. Jupille, Phys. Rev. B **79**, 235424 (2009).
[155] C. Mocuta, A. Barbier, G. Renaud, Panabière, and P. Bayle-Guillemaud, J. Appl. Phys. **95**, 2151 (2004).
[156] N. Jedrecy, G. Renaud, R. Lazzari, and et al., Phys. Rev. B **72**, 195404 (2005).
[157] C. Noguera, *Physics and Chemistry at Oxide Surfaces* (Cambridge University Press, Cambridge, 1995).
[158] A. Miyamoto, T. Hattori, and T. Inui, Appl. Surf. Sci. **60-61**, 660 (1992).
[159] A. M. Flank, R. Delaunay, P. Lagarde, M. Pompa, and J. Jupille, Phys. Rev.B **53**, R1737 (1996).
[160] O. Robach, G. Renaud, and A. Barbier, Phys. Rev. B **60**, 5858 (1999).
[161] A. Barbier, G. Renaud, and A. Stierle, Surf. Sci. **402-404**, 757 (1998).
[162] A. M. Ferrari and G. Pacchioni, J. Phys. Chem. **100**, 9032 (1996).
[163] I. Yudanov, G. Pacchioni, K. Neyman, and N. Rösh, J. Phys. Chem. B **101**, 2786 (1997).
[164] J. Goniakowski, Phys. Rev. B **57**, 1935 (1998).
[165] W. Hirschwald, *Zinc Oxide: Properties and Behaviour of the Bulk, the Solid/Vacuumand Solid/Gas Interface*, vol. 7 of *Material Science* (E. Kaldis North Holland Publishing, 1981).
[166] R. Zhang, A. Ludviksson, and C. T. Campbell, Surf. Sci. **289**, 1 (1993).
[167] E. Valkonen, B. Karlsson, and C. G. Rissing, Solar Energy **32**, 2121 (1984).
[168] http://www-cenerg.ensmp.fr/ease/advanced_glazing.
[169] S. Roberts and R. J. Gorte, J. Chem. Phys. **93**, 5337 (1990).
[170] W. T. Petrie and J. M. Vohs, J. Chem. Phys. **101**, 8098 (1994).
[171] P. V. Radulovic, C. S. Feigerle, and S. H. Overbury, J. Phys. Chem. **104**, 3028 (2000).
[172] Y. Yoshihara, S. C. Parker, and C. T. Campbell, Surf. Sci. **439**, 153 (1999).
[173] N. Jedrecy, S. Gallini, M. Sauvage-Simkin, and R. Pinchaux, Phys. Rev. B **64**, 085424 (2001).
[174] B. Meyer and D. Marx, Phys. Rev. B **69**, 235420 (2004).
[175] M. Haruta and M. Daté, Appl. Catal. A **222**, 427 (2001).
[176] T. V. Choudhary and D. W. Goodman, Appl. Catal. A **291**, 32 (2005).
[177] U. Diebold, Surf. Sci. Rep. **48**, 53 (2003).
[178] F. Cosandey and T. E. Madey, Surf. Rev. Lett. **8**, 73 (2001).
[179] X. Lai, T. P. St Clair, M. Valden, and D. W. Goodman, Prog. Surf. Sci. **59**, 25 (1998).
[180] X. Lai and D. W. Goodman, J. Mol. Cat. A: Chem **162**, 33 (2000).
[181] A. Kolmakov and D. W. Goodman, Surf. Sci. **490**, L597 (2001).
[182] N. Spiridis, J. Haber, and J. Korecki, Vacuum **63**, 99 (2001).
[183] C. E. J. Mitchell, A. Howard, M. Carney, and R. G. Edgell, Surf. Sci. **490**, 196 (2001).
[184] E. Wahlström, N. Lopez, R. Schaub, P. Thostrup, A. Rønnau, C. Africh, E. Lægsgaard, J. K. Nørskov, and R. Besenbacher, Phys. Rev. Lett. **90**, 026101 (2003).
[185] A. K. Santra, F. Yang, and D. W. Goodman, Surf. Sci. **548**, 324 (2004).
[186] Y. Maeda, T. Fujitani, S. Tsubota, and M. Haruta, Surf. Sci. **562**, 1 (2004).
[187] T. Minato, T. Susaki, S. Shiraki, H. S. Kato, M. Kawai, and K. Aika, Surf. Sci. **566-568**, 1012 (2004).
[188] W. T. Wallace, B. K. Min, and D. W. Goodman, J. Mol. Cat. A: Chem. **228**, 3 (2005).
[189] L. Zhang, F. Cosandey, R. Persaud, and T. E. Madey, Surf. Sci. **439**, 73 (1999).
[190] F. Cosandey, L. Zhang, and T. E. Madey, Surf. Sci. **474**, 1 (2001).
[191] L. Zhang, R. Persaud, and T. Madey, Phys. Rev. B **73**, 73 (1999).
[192] C. R. Henry, C. Chapon, C. Duriez, and S. Giorgio, Surf. Sci. **253**, 177 (1991).
[193] A. Trampert, F. Ernst, C. P. Flynn, H. F. Fischmeister, and M. Ruhle, Acta Met. Mat. **40**, S227 (1992).
[194] C. G. Vonk, J. Appl. Cryst. **9**, 433 (1976).
[195] G. Wulff, Z. Kristallogr. **34**, 449 (1901).
[196] Kaischew, Bull. Acad. Sci. Ser. Phys. **2**, 191 (1951).
[197] J. L. Viovy, D. Beysens, and C. M. Knobler, Phys. Rev. A **37**, 4965 (1988).
[198] B. J. Briscoe and K. P. Galvin, Phys. Rev. A **43**, 1906 (1991).
[199] P. Meakin, Rep. Prog. Phys. **55**, 157 (1992).
[200] F. Family and P. Meakin, Phys. Rev. Lett. **61**, 428 (1988).
[201] F. Family and P. Meakin, Phys. Rev. A **40**, 3836 (1989).
[202] A. Steyer, P. Guenoun, and D. Beysens, Phys. Rev. A **44**, 8271 (1991).
[203] G. Ehrlich and F. G. Hudda, J. Chem. Phys. **44**, 1030 (1966).

[204] R. L. Schwoebel and E. J. Shipsey, J. Appl. Phys. **37**, 3682 (1966).
[205] B. K. Chakraverty, J. Phys. Chem. Sol. **28**, 2413 (1967).
[206] H. Brune, Surf. Sci. Rep. **31**, 121 (1998).
[207] N. C. Bartelt, T. L. Einstein, and E. D. Williams, Surf. Sci. **298**, 421 (1993).
[208] S. V. Khare and T. L. Einstein, Phys. Rev. B **54**, 11752 (1996).
[209] J. Carrey, J. L. Maurice, F. Petroff, and Vaurès, Phys. Rev. Lett. **86**, 4600 (2001).
[210] G. Barcaro, A. Fortunelli, F. Nita, and R. Ferrando, Phys. Rev. Lett. **95**, 246103 (2005).
[211] L. Vitos, A. Ruban, H. Skriver, and J. Kollár, Surf. Sci. **411**, 186 (1998).
[212] P. Jensen and N. Combe, Comp. Mat. Sci. **24**, 78 (2002).
[213] N. Combe, P. Jensen, and A. Pimpinelli, Phys. Rev. Lett. **85**, 110 (2000).
[214] J. Sinfelt, *Bimetallic Catalysts* (Wiley, New-York, 1983).
[215] B. N. Kuznetsov, Y. I. Yermakov, M. Boudart, and J. P. Collman, J. Mol. Catal. **4**, 49 (1978).
[216] Y. I. Yermakov, B. N. Kuznetsov, and Y. A. Ryndin, J. Catal. **42**, 73 (1976).
[217] G. Leclercq, I. Romero, S. Pietrzyk, J. Grimblot, and L. Leclercq, J. Mol. Catal. **25**, 67 (1984).
[218] A. Trunschke, H. Ewald, D. Gutschick, H. Miessner, M. Skupin, B. Walther, and H.-C. Bottcher, J. Mol. Catal. **56**, 95 (1989).
[219] T. E. Madey, J. Guan, C.-H. Nien, C.-Z. Dong, H.-S. Tao, and R. A. Campbell, Surf. Rev. Lett. **3**, 1315 (1996).
[220] T. E. Madey, C.-H. Nien, K. Pelhos, J.-J. Kolodziej, I. M. Abdelrehim, and H.-S. Tao, Surf. Sci. **438**, 191 (1999).
[221] T. E. Madey, K. Pelhos, Q. Wu, R. Barnes, I. Ermanoski, W. Chen, J.-J. Kolodziej, and J. E. Rowe, PNAS **99**, 6503 (2002).
[222] K.-J. Song, R. A. Demmin, C. Dong, E. Garfunkel, and T. E. Madey, Surf. Sci. **227**, L79 (1990).
[223] T. E. Madey, K.-J. Song, C.-Z. Dong, and R. A. Demmin, Surf. Sci. **247**, 175 (1991).
[224] C. Herring, Phys. Rev. **82**, 87 (1951).
[225] J. G. Che, C. T. Chan, C. H. Kuo, and T. C. Leung, Phys. Rev. Lett. **79**, 4230 (1997).
[226] K. Pelhos, J. B. Hannon, G. L. Kellogg, and T. E. Madey, Surf. Sci. **432**, 115 (1999).
[227] K. Pelhos, T. E. Madey, J. B. Hannon, and G. L. Kellogg, Surf. Rev. Lett. **5**, 767 (1999).
[228] J. J. Kolodziej, T. E. Madey, J. W. Keister, and J. E. Rowe, Phys. Rev. B **65**, 075413 (2002).
[229] C.-H. Nien, T. E. Madey, Y. W. Tai, T. C. Leung, J. G. Che, and C. T. Chan, Phys. Rev. B **59**, 10335 (1999).
[230] D. K. G. de Boer, Phys. Rev. B **49**, 5817 (1994).
[231] M. De Santis, R. Baudoing-Savois, P. Dolle, and M. C. Saint-Lager, Phys. Rev. B **66**, 085412 (2002).
[232] A. V. Ruban, H. L. Skriver, and J. K. Nørskov, Phys. Rev. B **59**, 15990 (1999).
[233] P. Gambardella, A. Dallmeyer, K. Maiti, M. C. Malagoli, W. Eberhardt, K. Kern, and C. Carbone, Nature **416**, 301 (2001).
[234] G. Springholz, V. Holý, M. Pinczolits, and G. Bauer, Science **282**, 734 (1998).
[235] H. Ellmer, V. Repain, M. Sotto, and S. Rousset, Surf. Sci. **511**, 183 (2002).
[236] D. D. Chambliss, R. J. Wilson, and S. Chiang, Phys. Rev. Lett. **66**, 1721 (1991).
[237] P. Gambardella, M. Blanc, H. Brune, K. Kuhnke, and K. Kern, Phys. Rev. B **61**, 2254 (2000).
[238] A. Ohtake and N. Koguchi, Appl. Phys. Lett. **89**, 083108 (2006).
[239] H. Brune, M. Giovannini, K. Bromann, and K. Kern, Nature **394**, 451 (1998).
[240] F. Leroy, G. Renaud, A. Létoublon, S. Rohart, Y. Girard, V. Repain, S. Rousset, A. Coati, and Y. Garreau, Phys. Rev. B **77**, 045430 (2008).
[241] P. Torelli, E. A. Soares, G. Renaud, L. Gragnaniello, S. Valeri, X. X. Guo, and P. Luches, Phys. Rev. B **77**, 081409(R) (2008).
[242] S. Padovani, *PhD-thesis of Louis Pasteur University (Strasbourg, France)* (1999).
[243] A. R. Sandy, S. G. J. Mochrie, D. M. Zehner, K. G. Huang, and D. Gibbs, Phys. Rev. B **43**, 4667 (1991).
[244] J. V. Barth, H. Brune, G. Ertl, and R. J. Behm, Phys. Rev. B **42**, 9307 (1990).
[245] U. Harten, A. M. Lahee, J. P. Toennies, and C. Wöll, Phys. Rev. Lett. **54**, 2619 (1985).
[246] V. Repain, G. Baudot, H. Ellmer, and S. Rousset, EuroPhys. Lett. **58**, 730 (2002).
[247] O. Fruchart, M. Klaua, J. Barthel, and J. Kirschner, Phys. rev. Lett. **83**, 2769 (1999).
[248] O. Fruchart, G. Renaud, A. Barbier, M. Noblet, O. Ulrich, J.-P. Deville, F. Scheurer, J. Mane-Mane, V. Repain, G. Baudot, et al., Europhys. Lett. **63**, 275 (2003).
[249] S. Padovani, I. Chado, F. Scheurer, and J.-P. Bucher, Phys. Rev. B **59**, 11887 (1999).
[250] Q. Xie, A. Madhukar, P. Chen, and N. P. Kobayashi, Phys. Rev. Lett. **75**, 2542 (1995).
[251] S. Rousset, V. Repain, G. Baudot, Y. Garreau, and J. Lecoeur, J. Phys. : Cond. Mat. **15**, S3363 (2003).
[252] S. Rohart, G. Baudot, V. Repain, Y. Girard, S. Rousset, H. Bulou, C. Goyhenex, and L. Proville, Surf. Sci. **559**, 47 (2004).
[253] V. Repain, J. M. Berroir, S. Rousset, and J. Lecoeur, EuroPhys. Lett. **47**, 435 (1999).
[254] C. S. Lent and P. I. Cohen, Surf. Sci. **139**, 121 (1984).
[255] P. R. Pukite, C. S. Lent, and P. I. Cohen, Surf. Sci. **161**, 39 (1985).
[256] B. Croset and C. de Beauvais, Surf. Sci. **409**, 403 (1998).
[257] G. Uimin and P.-A. Lindgård, Acta Cryst. A **53**, 15 (1997).
[258] J. Tegenkamp, J. Wollschläger, H. Pfnür, F.-J. Meyer zu Heringdorf, and M. Horn-von Hoegen, Phys. Rev. B **65**, 235316 (2002).
[259] M. Sotto and B. Croset, Surf. Sci. **461**, 78 (2000).
[260] D. Farias and K.-H. Rieder, Rep. Prog. Phys. **61**, 1575 (1998).
[261] A. Crottini, D. Cvetko, L. Floreano, R. Gotter, A. Morgante, and F. Tommasini, Phys. Rev. Lett. **79**, 1527 (1997).
[262] H.-J. Ernst, F. Fabre, and J. Lapujoulade, Phys. Rev. B **46**, 1929 (1992).

[263] F. Dulot, B. Kierren, and D. Malterre, Thin Solid Films **428**, 72 (2003).
[264] B. Salanon and P. Hecquet, Surf. Sci. **412-413**, 639 (1998).
[265] P. Müller and A. Saùl, Surf. Sci. Rep. **54**, 157 (2004).
[266] V. Repain, G. Baudot, H. Ellmer, and S. Rousset, Materials Science and Engineering B **96**, 178 (2002).
[267] N. Witkowski, Y. Borensztein, G. Baudot, V. Repain, Y. Girard, and S. Rousset, Phys. Rev. B **70**, 85408 (2004).
[268] A. Bourret, Surf. Sci. **432**, 37 (1999).
[269] B. Degroote, J. Dekoster, and G. Langouche, Surf. Sci. **452**, 172 (2000).
[270] P. W. Palmberg, T. N. Rhodin, and C. J. Todd, Appl. Phys. Lett. **11**, 33 (1967).
[271] A. Rockett and C. J. Kiely, Phys. Rev. B **44**, 1154 (1991).
[272] A. K. Seeger, J. Appl. Phys. **30**, 629 (1959).
[273] R. Bonnet and J.-L. Verger-Gaugry, Phil. Mag. A **66**, 849 (1992).
[274] J. Wollschlager, D. Erdos, H. Goldbach, R. Hopken, and K. M. Schroder, Thin Solid Films **400**, 1 (2001).
[275] M. Dynna, J. L. Vassent, A. Marty, and B. Gilles, J. Appl. Phys. **80**, 2650 (1996).
[276] S. Benedetti, H. Benia, N. Nilius, S. Valeri, and H. Freund, Chem. Phys. Lett. **430**, 330 (2006).
[277] R. L. McGreevy, J. Phys. Cond. Mat. **13**, R877 (2001).
[278] S. Narayanan, D. R. Lee, A. Hagman, X. Li, and J. Wang, Phys. Rev. Lett. **98**, 185506 (2007).
[279] S. Streit, C. Guut, V. Chamard, A. Robert, M. Sprung, H. Sternemann, and M. Tolan, Phys. Rev. Lett. **98**, 047801 (2007).
[280] A. Boukai, Y. Bunimovich, J. Tahir-Kheli, J. K. Yu, W. A. Goddard III, and J. R. Heath, Nature **451**, 168 (2007).
[281] M. S. Gudiksen, L. Lauhon, J. Wang, D. Smith, and C. Lieber, Nature **415**, 617 (2002).
[282] E. Minot, F. Kelkensberg, M. van Kouwen, J. van Dam, L. Kouwenhoven, V. Zwiller, M. Borgstrom, O. Wunnicke, M. Verheijen, and E. Bakkers, Appl. Phys. Lett. **7**, 367 (2007).
[283] M. Bjork, A. Fuhrer, A. Hansen, M. Larsson, L. Froberg, and L. Samuelson, Phys. Rev. B **72**, 201307 (2005).
[284] A. Pfund, I. Shorubalko, K. Ensslin, and R. Leturcq, Phys. Rev. Lett. **99**, 036801 (2007).
[285] F. Zwanenburg, C. van Rijmenam, Y. Fang, C. Lieber, and C. Kouwenhoven, Nano Lett. **4**, 1621 (2004).
[286] Y. Xia, P. Yang, Y. Sun, Y. Wu, B. Mayers, B. Gates, Y. Yin, F. Kim, and H. Yan, Adv. Mater **15**, 353 (2003).
[287] P. Yang, R. Yan, and M. Fardy, Nano Lett. **10**, 1529 (2010).
[288] A. Zhang, H. Kim, J. Cheng, and Y. H. Lo, Nano Lett. **10**, 2117 (2010).
[289] M. H. Huang, S. Mao, H. Feick, H. Q. Yan, Y. Y. Wu, H. Kind, E. Weber, R. Russo, and P. D. Yang, Science **292**, 1897 (2001).
[290] X. F. Duan, Y. Huang, R. Agarwal, and C. M. Lieber, Nature **421**, 241 (2003).
[291] B. Tian, X. Zheng, T. Kmpa, Y. Fang, N. F. Yu, G. Yu, J. Huang, and C. Lieber, Nature **449**, 885 (2007).
[292] E. Garnett and P. Yang, Nano Lett. **10**, 1082 (2010).
[293] Y. Quin, X. Wang, and Z. L. Wang, Nature **451**, 809 (2008).
[294] J. Xiang, W. Lu, Y. Hu, y. Wu, H. Yan, and C. M. Lieber, Nature **441**, 489 (2006).
[295] M. T. Borgström, G. Immink, B. Ketelaars, R. Algra, and E. P. A. M. Bakkers, Nature nanotechnology **2**, 541 (2007).
[296] W. Lu and C. M. Lieber, Nature materials **6**, 841 (2007).
[297] L. J. Lauhon, M. S. Gudiksen, D. Wang, and C. M. Lieber, Nature **420**, 57 (2002).
[298] Y. Li, F. Qian, J. Xiang, and C. Lieber, Mater Today **9**, 18 (2006).
[299] K. Dick, K. Deppert, L. Samuelson, L. Wallenberg, and F. Ross, Nano Lett. **8**, 4087 (2008).
[300] K. Kolasinski, Curr. Opin. Solid Stat Mater. Sci. **10**, 182 (2006).
[301] R. Wagner and W. Ellis, Appl. Phys. Lett. **4**, 89 (1964).
[302] B. Wacaser, K. Dick, J. Johansson, M. Borgstroem, K. Deppert, and L. Samuelson, Adv. Mater. **21**, 153 (2009).
[303] Y. Wu and P. Yang, J. Am. Chem. Soc. **123**, 3165 (2001).
[304] T. Kamins, X. Li, and R. Stanley Williams, Nano Letters **4**, 503 (2004).
[305] F. Ross, J. Tersoff, and M. Reuter, Phys. Rev. Lett. **95**, 146104 (2005).
[306] S. Kodambaka, J. Tersoff, M. Reuter, and F. Ross, Science **316**, 729 (2007).
[307] E. Sutter and P. Sutter, Nano Letters **8**, 411 (2008).
[308] J. B. Hannon, S. Kodambaka, F. M. Ross, and R. M. Tromp, Nature **440**, 69 (2006).
[309] H. Fan, P. Werner, and M. Zacharias, Small **6**, 700 (2006).
[310] B. S. Meyerson, Proc. IEEE **80**, 1592 (1992).
[311] S. Bozzo, J.-L. Lazzari, C. Coudreau, A. Ronda, F. Arnaud d'Avitaya, J. Derrien, S. Mesters, B. Hollaender, P. Gergaud, and O. Thomas, J. Cryst. Growth **216**, 171 (2000).
[312] Y. W. Wang, V. Schmidt, S. Senz, and U. Gosele, Nature Nanotech. **1**, 186 (2006).
[313] M. Hammar, F. LeGoues, J. Tersoff, M. Reuter, and R. Tromp, Surf. Sci. **349**, 129 (1996).
[314] L. Goldstein, J. Y. F. Glas, M. N. Marczin, Charasse, and G. LeRoux, Appl. Phys. Lett. **47**, 1099 (1985).
[315] Y.-M. Mo, D. E. Savage, B. S. Swartzentruber, and M. G. Lagally, Phys. Rev. Lett. **65**, 1020 (1990).
[316] D. J. Eaglesham and M. Cerullo, Phys. Rev. Lett. **64**, 1943 (1990).
[317] G. Medeiros-Ribeiro, A. M. Bratkowski, and T. I. Kamins, Science **279**, 353 (1998).
[318] I. N. Stranski and L. Krastanow, Sitzungsber. Akad. Wiss. Wien, Math.-Naturwiss. Kl., Abt. 2B **146**, 797 (1938).
[319] M. M. e. a. Z. Zhong, A. Halilovic, Appl. Phys. Lett. **82**, 4779 (2003).
[320] Z. Zhong and G. Bauer, Appl. Phys. Lett. **84**, 1992 (2004).
[321] F. Fournel, H. Moriceau, B. Aspar, K. Rousseau, J. Eymery, J. L. Rouviere, and N. Magnea, Appl. Phys. Lett. **80**, 793 (2002).
[322] F. Leroy, J. Eymery, and F. Gentile, P. anf Fournel, Surf. Sci. **545**, 211 (2003).

[323] F. M. Ross, J. T. ersoff, and R. M. Tromp, Phys. Rev. Lett. **80**, 984 (1998).
[324] P. Sutter and M. Lagally, Phys. Rev. Lett. **81**, 3471 (1998).
[325] M.-I. Richard, T. U. Schulli, E. Wintersberger, G. Renaud, and G. Bauer, Thin Solid Films **508**, 213 (2006).
[326] T. Schulli, M. Richard, and G. e. a. Renaud, Appl. Phys. lett. **89**, 143114 (2006).
[327] A. Malachias, T. U. Schulli, G. Medeiros-Ribeiro, L. G. Cancado, M. Stoffel, O. G. Schmidt, T. H. Metzger, and R. Magalhaes-Paniago, Phys. Rev. B **72**, 165315 (2005).
[328] I. Kegel, T. H. Metzger, A. Lorke, J. Peisl, J. Stangl, G. Bauer, J. M. Garcia, and P. M. Petroff, Phys. Rev. Lett. **85**, 1694 (2000).
[329] T. U. Schulli, J. Stangl, Z. Zhong, R. T. Lechner, M. Sztucki, T. H. Metzger, and G. Bauer, Phys. Rev. Lett. **90**, 066105 (2003).
[330] A. Malachias, S. Kycia, G. Medeiros-Ribeiro, R. Magalhães-Paniago, T. I. Kamins, and R. S. Williams, Phys. Rev. Lett. **91**, 176101 (2003).
[331] R. Dujardin, V. Poydenot, T. U. Schulli, G. Renaud, O. Ulrich, A. Barski, M. Derivaz, S. Colonna, and T. Metzger, J. Appl. Phys. **99**, 063510 (2006).
[332] J. Hodeau, V. Favre-Nicolin, S. Bos, H. Renevier, E. Lorenzo, and J. Bérar, Chem. Rev. **101**, 1843 (2001).
[333] T. Zhou, G. Renaud, J. Issartel, C. Revenant, T. Schulli, R. Felici, and A. Malchias, Phys. Rev. B **83** (2010).
[334] M. Richard, T. Schulli, G. Renaud, E. Wintyersberger, G. Bauer, and V. Holy, Phys. Rev. B **80**, 045313 (2009).
[335] G. Chen, G. Vastola, H. Lichtenberger, D. Pachinger, G. Bauer, W. Jantsch, F. Schäffler, and L. Miglio, Appl. Phys. Lett. **92**, 113106 (2008).
[336] A. Letoublon, V. Favre-Nicolin, H. Renevier, M. Proietti, C. Monat, M. Gendry, O. Marty, and C. Priester, Phys. Rev. Lett. **92**, 186101 (2004).
[337] J. Coraux, H. Renevier, V. Favre-Nicolin, G. Renaud, and B. Daudin, Appl. Phys. Lett. **88**, 153125 (2006).
[338] O. Landré, D. Camacho, C. Bougerol, Y. M. Niquet, V. Favre-Nicolin, G. Renaud, H. Renevier, and B. Daudin, Phys. Rev. B **81**, 153306 (2010).
[339] K. Tateno, H. Hibino, H. Gotoh, and H. Nakano, Appl. Phys. Lett. **89**, 033114 (2006).
[340] J. Eymery, F. Rieutord, V. Favre-Nicolin, O. Robach, Y.-M. Niquet, L. Fröberg, T. Mårtensson, and L. Samuelson, Nanolett. **7**, 2596 (2007).
[341] B. Tinkham, B. Jenichen, V. Kanager, R. Shayduk, W. Braun, and K. Ploog, J. Cryst. Growth **310**, 3416 (2008).